

AU-A128 478

CURRENT PROBLEMS IN TURBOMACHINERY FLUID DYNAMICS(I)  
MASSACHUSETTS INST OF TECH CAMBRIDGE GAS TURBINE AND  
PLASMA DYNAMICS LAB E W GREITZER ET AL. 31 DEC 82

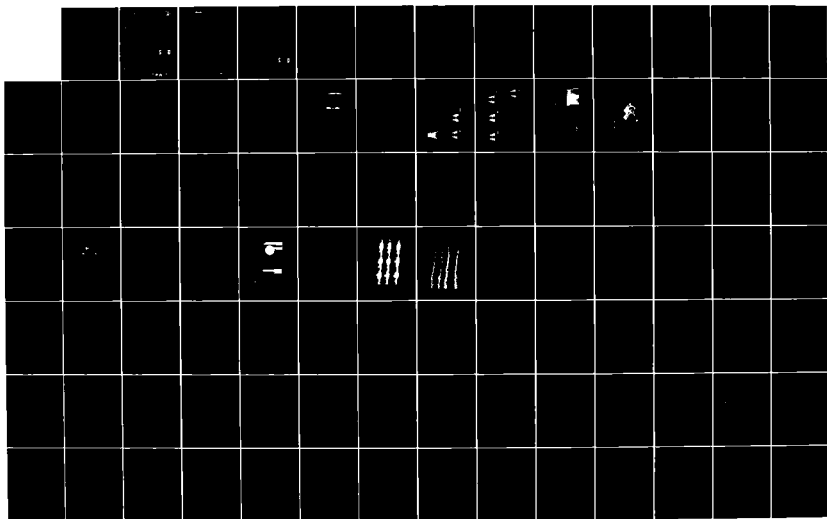
1/2

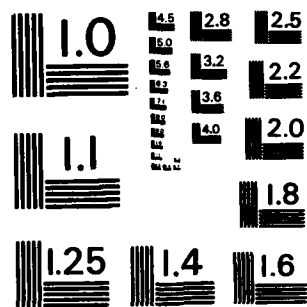
(UNCLASSIFIED

AFOSR-TR-83-0147 F49620-82-K-0002

F/G 21/5

NL





MICROCOPY RESOLUTION TEST CHART  
 NATIONAL BUREAU OF STANDARDS-1963-A

UNCLASSIFIED

3

SECURITY CLASSIFICATION OF THIS PAGE (When Data Entered)

REPORT DOCUMENTATION PAGE

READ INSTRUCTIONS BEFORE COMPLETING FORM

1. REPORT NUMBER <b>AFOSR-TR- 83-0147</b>		2. GOVT ACCESSION NO.	3. RECIPIENT'S CATALOG NUMBER
4. TITLE (and Subtitle) <b>CURRENT PROBLEMS IN TURBOMACHINERY FLUID DYNAMICS</b>		5. TYPE OF REPORT & PERIOD COVERED <i>Annual</i> <b>10/1/81 - 11/30/82</b>	
7. AUTHOR(s) <b>E.M. Greitzer, W.T. Thompkins, Jr., J.E. McCune, A.H. Epstein, C.S. Tan, W.R. Hawthorne</b>		8. CONTRACT OR GRANT NUMBER(s) <b>F49620-82-K-0002</b>	
9. PERFORMING ORGANIZATION NAME AND ADDRESS <b>GAS TURBINE &amp; PLASMA DYNAMICS LABORATORY DEPARTMENT OF AERONAUTICS &amp; ASTRONAUTICS MASSACHUSETTS INSTITUTE OF TECHNOLOGY, CAMBRIDGE, MA</b>		10. PROGRAM ELEMENT PROJECT, TASK AREA & WORK UNIT NUMBERS <b>61102F 3307/A4</b>	
11. CONTROLLING OFFICE NAME AND ADDRESS <b>AIR FORCE OFFICE OF SCIENTIFIC RESEARCH DIRECTORATE OF AEROSPACE SCIENCES BOLLING AFB, DC 20332</b>		12. REPORT DATE <b>December 31, 1982</b>	
14. MONITORING AGENCY NAME & ADDRESS (if different from Controlling Office)		13. NUMBER OF PAGES <b>135</b>	
		15. SECURITY CLASS. (of this report) <b>Unclassified</b>	
		15a. DECLASSIFICATION/DOWNGRADING SCHEDULE	
16. DISTRIBUTION STATEMENT (of this Report) <b>Approved for Public Release; Distribution Unlimited</b>			
17. DISTRIBUTION STATEMENT (of the abstract entered in Block 20, if different from Report)			
18. SUPPLEMENTARY NOTES			
19. KEY WORDS (Continue on reverse side if necessary and identify by block number)			
casing/hub treatment		three-dimensional flow	
axial flow turbomachinery		flow measurements in transonic fans	
axial flow compressors		transonic flow	
computational fluid dynamics		vortex flows	
compressor stall		inlet distortion	
20. ABSTRACT (Continue on reverse side if necessary and identify by block number)			
A multi-investigator program on problems of current interest in turbomachinery fluid dynamics is being conducted at the M.I.T. Gas Turbine & Plasma Dynamics Lab. Within the scope of this effort, four different tasks, encompassing both design and off-design problems, have been identified. These are: 1) Investigation of fan and compressor design point fluid dynamics (including formation of design procedures using current three-dimensional transonic codes and development of advanced measurement techniques for use in transonic fans) (continued on reverse side)			

ADA 126478

DTIC FILE COPY

DTIC ELECTE  
S APR 6 1983 D  
D

88-04-05-187  
UNCLASSIFIED

**UNCLASSIFIED**

SECURITY CLASSIFICATION OF THIS PAGE (When Data Entered)

20.

2) Studies of basic mechanisms of compressor stability enhancement using compressor casing/hub treatment; 3) Fluid mechanics of inlet vortex flow distortions in gas turbine engines; 4) Investigations of three-dimensional flows in highly loaded turbomachines (including blade-to-blade flow analysis and numerical computations of secondary flow in a bend using spectral methods. In addition to these tasks, this multi-investigator effort also includes the Air Force Research in Aero Propulsion Technology (AFRAPT) Program. ←

This document describes work carried out on this contract during the period 10/1/81 - 11/30/82.



<b>Accession For</b>	
NTIS GRA&I	<input checked="" type="checkbox"/>
DTIC TAB	<input type="checkbox"/>
Unannounced	<input type="checkbox"/>
<b>Justification</b>	
By _____	
Distribution/	
<b>Availability Codes</b>	
Dist	Avail and/or Special
A	

**UNCLASSIFIED**

SECURITY CLASSIFICATION OF THIS PAGE (When Data Entered)

**AFOSR-TR- 83 - 0147**

GAS TURBINE & PLASMA DYNAMICS LABORATORY  
DEPARTMENT OF AERONAUTICS & ASTRONAUTICS  
MASSACHUSETTS INSTITUTE OF TECHNOLOGY  
CAMBRIDGE, MASSACHUSETTS 02139

ANNUAL REPORT

on

CONTRACT NO. F49620-82-K-0002

entitled

CURRENT PROBLEMS IN TURBOMACHINERY FLUID DYNAMICS

for the period

October 1, 1981 to November 31, 1982

submitted to

AIR FORCE OFFICE OF SCIENTIFIC RESEARCH

Attention of: Dr. James D. Wilson, Program Manager  
Directorate of Aerospace Sciences, AFOSR (AFSC)  
Bolling Air Force Base, DC 20332

Principal  
Investigators: Edward M. Greitzer  
William T. Thompkins, Jr.  
James E. McCune

Co-Investigators: Alan H. Epstein  
Choon S. Tan

Collaborating  
Investigators: Eugene E. Covert  
Sir William R. Hawthorne  
Frank H. Durgin

December 30, 1982

Approved for public release;  
distribution unlimited.

UNCLASSIFIED

88 04 05 187

DTIC  
ELECTE  
S APR 6 1983 D  
D

TABLE OF CONTENTS

<u>SECTION</u>	<u>PAGE NO.</u>	
1. INTRODUCTION AND RESEARCH OBJECTIVES	1	
2. WORK TO DATE AND STATUS OF THE RESEARCH PROGRAM	2	
Task I: Investigation of Fan and Compressor Design Point Fluid Dynamics	2	
A: Inverse Design	2	
Appendix	6	
B: Advanced Measurements in Transonic Compressors	21	
Task II: Mechanisms of Compressor Stability Enhancement Using Casing/Hub Treatment	53	
Task III: Inlet Vortex Flow Distortion in Gas Turbine Engines	83	
Task IV: Investigation of Discrete-Blade and Three- Dimensional Flow in Highly Loaded Turbomachines	103	
1. Blade-to-Blade Effects	103	
2. Non-Axisymmetric Compressible Swirling Flow in Turbomachine Annuli	105	
3. Theory of Blade Designs for Large Deflections	106	
4. Numerical Studies of Secondary Flow in a Bend Using Spectral Methods	109	
5. Numerical Calculation of Flow in Casing Treatment Grooves	114	
General Progress on AFRAPT	125	
3. PUBLICATIONS	126	
4. PROGRAM PERSONNEL	<b>AIR FORCE OFFICE OF SCIENTIFIC RESEARCH (AFSC)</b> <b>NOTICE OF TRANSMITTAL TO DTIC</b> This technical report has been reviewed and is approved for public release IAW AFR 130-12. Distribution is unlimited.	127
5. INTERACTIONS	MATTHEW J. KENFER Chief, Technical Information Division	128
6. DISCOVERIES		130
7. CONCLUSIONS		131

## 1. INTRODUCTION AND RESEARCH OBJECTIVES

This report describes work carried out at the Gas Turbine and Plasma Dynamics Laboratory at M.I.T., as part of a multi-investigator effort on current problems in turbomachinery fluid dynamics. Support for this program is provided by the Air Force Office of Scientific Research under Contract Number F49620-82-K-0002, Dr. J.D. Wilson, Program Manager.

The present report gives a summary of the work for the period 10/1/81 - 9/30/82. For further details and background, the referenced reports, publications and the previous Final Report (covering the period 10/1/79 - 9/30/81)<sup>1</sup> should be consulted.

Within the general topic, four separate tasks are specified. These have been described in detail in Reference 1, but they are, in brief:

1. Investigation of fan and compressor design point fluid dynamics
2. Studies of compressor stability enhancement
3. Fluid mechanics of gas turbine engine operation in inlet flow distortion
4. Investigations of three-dimensional flows in highly loaded turbomachines

In addition to these tasks, the multi-investigator contract also encompasses the Air Force Research in Aero Propulsion Technology program. The work carried out in each of the tasks will be described in the next section.

---

1. E.M. Greitzer et al., AFOSR TR-82-0027, Final Report, 10/79-9/81, on "Current Problems in Turbomachinery Fluid Dynamics"

TASK I: INVESTIGATION OF FAN AND COMPRESSOR DESIGN POINT FLUID DYNAMICS

TASK IA: INVERSE DESIGN

Task Status

During the last two years a procedure which uses an input blade static pressure distribution to construct a geometry for supersonic cascades has been produced. This procedure assumed inviscid flow in the cascade. Continued progress, for either two or three dimensional design schemes, requires that a definition of a "better" blade row geometry be adopted, and we chose to define better as a lower stagnation pressure loss for the same row static pressure rise. The procedures previously developed gave us the ability to produce a blade row design for a specified blade static pressure, but were unworkable for producing better cascade geometries for two reasons. First, for supersonic cascades, boundary layer growth interacts strongly with the inviscid core flow and makes it quite difficult to design realistic profiles when viscous effects are not considered. Second, for low stagnation pressure loss blade designs, the numerical errors in conservation of stagnation pressure became comparable with the physical shock loss.

We felt that, since a number of procedures to add viscous flow effects to an inviscid calculation existed, but that little or no recent progress had been made toward improving conservation properties of time-marching algorithms, it was most important to concentrate on the problem of stagnation pressure errors in numerical algorithms. This problem turned out to be much harder to understand and cure than

had been anticipated, and nearly all our efforts this year have gone into solving this under-appreciated problem.

This effort has largely been successful, and our present algorithms have reduced the stagnation pressure error from an intolerable 10% to 15% to about 1%. At the present time, we have what we consider to be the best possible second order accurate numerical scheme for our purposes, and we are using it to design shock-free supercritical stators in order to demonstrate that we have solved the stagnation pressure error problem. Our next step will be to combine this improved numerical scheme with a new boundary layer code under development for NASA Lewis so that optimization calculations including viscous-inviscid interaction may be done for the design task.

#### Summary of Effort for the Current Reporting Period

The major effort for this reporting period was the search for sources of stagnation pressure errors in time-marching calculations. Two important sources of error were identified and corrected in the current algorithms. The first error source was, roughly speaking, that the algorithm solutions were sensitive to the shape of the finite difference grid in a way distinct from the fineness of the grid. In finite element terminology, the algorithms did not maintain geometric area conservation. The second error source was due to the details of specifying the solid wall boundary conditions.

Correction of errors due to grid shape is an important step toward solution of the design problem, but errors due to specification of solid wall boundaries are unimportant for the projected

viscous-inviscid interaction calculation since the flow in the solid wall region will be calculated by a boundary layer solver.

The search for these error sources demonstrated that nearly all popular time-marching schemes have identical interior point properties, and that finite difference solutions to problems posed in strong conservation law form can be made to be identical to so-called finite volume formulations. This work was collected in an AIAA paper, AIAA-83-0257 included as Appendix A, which will be presented in January 1983.

Efforts to understand these stagnation point errors did not produce a dramatic new algorithm, but did demonstrate how to optimize existing algorithms to produce significantly better results. The most severe test of our new numerical procedures is the shock-free supercritical stator problem where the flow solution must be nearly isentropic at every point in order to produce shock-free solutions. The test case chosen was the design due to Sanz, and comparisons between predicted and computed surface Mach numbers are shown in figures 12 and 14a of Appendix A. The level of stagnation pressure errors is shown in figure 13 and 14b. Older procedures predicted a shock on the suction surface and a stagnation pressure error greater than 15%. The present results are extremely good for an Euler flow calculation matched against a potential flow solver.

Work for Next Reporting Period

In order to demonstrate that it is feasible to optimize cascade blade shapes using the procedures developed, three projects are planned for the next reporting period.

- 1) Design a supercritical stator similar to the Sanz blade with a smaller gap to chord ratio. The hodograph procedure used by Sanz often breaks down as the blade spacing is reduced. This project will complete the thesis work of Tong.
- 2) Couple the present numerical code to the viscous-inviscid interaction procedure under development for NASA Lewis to incorporate viscous effects into design procedure.
- 3) Design an optimum two-dimensional supersonic compressor cascade on the basis of minimum stagnation pressure loss for shock system loss plus wake loss.

APPENDIX A

SOLUTION PROCEDURES FOR ACCURATE NUMERICAL  
SIMULATIONS OF FLOW IN TURBOMACHINERY CASCADES

W. T. THOMPSON Jr.\*  
S. S. TONG\*\*  
R. H. BUSH\*\*  
W. J. USAB Jr.\*\*  
R. J. G. NORTON\*\*\*

Massachusetts Institute of Technology  
Cambridge, Massachusetts

Abstract

For several years the authors have been involved in evaluating and developing numerical simulation schemes for compressible, two dimensional inviscid or viscous flows in turbomachinery cascades. Numerical schemes considered were all originally classified as time-marching schemes and include: 1) implicit approximate factorization schemes like those of Beam and Warming, 2) explicit schemes due to MacCormack, 3) explicit central difference schemes due to Jameson, Schmidt and Turkel and Rizzi, and 4) the multi-grid scheme of Ni. As we have developed these schemes we have come to believe that the accuracy of computational results is relatively insensitive to the numerical algorithms chosen but highly sensitive to implementation details such as boundary conditions, consistent flux balancing, grid resolution and numerical smoothing. In order to illustrate our viewpoint, we present an examination of the relationship between a flux balancing interpretation of the control volume conservation laws and various finite difference formulations and comparisons of the performance of these schemes on three test problems: Ni's bump in a channel, a supersonic nozzle, and flow in a supercritical compressor cascade. As a final test example, a comparison is made between measured and computed flow, using a compressible, Navier-Stokes solver, for a high speed turbine cascade.

Finite Difference Operator Definitions

$$\delta_j^0 u_{j,k} = \frac{1}{2}(u_{j+1,k} - u_{j-1,k})$$

$$u_j^+ u_{j,k} = \frac{1}{2}(u_{j+1,k} + u_{j,k})$$

$$u_j^- u_{j,k} = \frac{1}{2}(u_{j,k} + u_{j-1,k})$$

$$\delta_j^+ u_{j,k} = u_{j+1,k} - u_{j,k}$$

$$\delta_j^- u_{j,k} = u_{j,k} - u_{j-1,k}$$

$$\delta_{j/2}^0 u_{j,k} = u_{j+\frac{1}{2},k} - u_{j-\frac{1}{2},k}$$

Note that all coordinate positions at non-integer mesh spacing are to be defined by simple averages,

$$y_{j+\frac{1}{2},k} = \frac{1}{2}(y_j + y_{j+1},k)$$

\*Associate Professor, Department of Aeronautics and Astronautics; Member AIAA

\*\*Research Assistant, Department of Aeronautics and Astronautics

\*\*\*Visiting Engineer; permanent affiliation: Rolls-Royce, Inc., Atlanta, Georgia

INTRODUCTION

For several years the authors have been involved in evaluating and developing numerical methods for compressible, inviscid or viscous, internal flow problems. The methods discussed in this paper include (1) implicit approximation factorization schemes due to Beam and Warming [1], (2) explicit schemes due to MacCormack [2], (3) an explicit central difference scheme suggested by Jameson, Schmidt and Turkel [3] and Rizzi [4], and (4) the multi-grid scheme due to Ni [5]. Most of these methods were originally formulated as time-marching methods although all are now run as pseudo-time-marching methods.

Throughout these evaluations we have been interested primarily in the accuracy of the steady state solutions rather than the computer run time or number of iterations to convergence. As we have developed these methods we have come to believe that the accuracy of the computational results is relatively insensitive to the numerical scheme chosen, but it is highly sensitive to implementation details such as boundary conditions, consistent flux balancing, grid resolution and numerical smoothing.

In order to illustrate our viewpoint we first present an examination of the relationship between a flux balancing or finite volume interpretation of the control volume conservation laws and a finite difference formulation in strong conservation law form. While the development here is perhaps not unique or entirely new, it is essential for understanding the relationships between various numerical schemes. Next we present a development, from a flux balance viewpoint, of the several schemes which emphasizes their basic similarity rather than their computational differences. The conclusion here is that all these schemes should produce nearly the same steady state solutions when the same boundary conditions and smoothing operators are applied. Results from three inviscid computational test problems are then presented in order to demonstrate the validity of this conclusion. Lastly, results from computations using a full Navier-Stokes version of the Beam-Warming algorithm are compared to experimental results for a high speed, high turning turbine cascade. These results illustrate that a consistent application of the flux balancing analysis can produce accurate solutions even in extreme geometries with rather modest cost. The number of iterations to full convergence is about 500 for a grid containing 100x50 nodes.

ANALYSIS

Relationship Between Finite Difference and Finite Volume Interpretations

Consider the two-dimensional Euler equation expressed in conservation law form:

$$\frac{\partial U}{\partial t} + \frac{\partial F}{\partial x} + \frac{\partial G}{\partial y} = 0 \quad (1)$$

$$U = \begin{pmatrix} \rho \\ \rho u \\ \rho v \\ \rho E \end{pmatrix} \quad F = \begin{pmatrix} \rho u \\ \rho u^2 + p \\ \rho uv \\ \rho u(E+p/\rho) \end{pmatrix} \quad G = \begin{pmatrix} \rho v \\ \rho uv \\ \rho v^2 + p \\ \rho v(E+p/\rho) \end{pmatrix}$$

and a coordinate system transformation,

$$\xi = \xi(x,y) \quad \eta = \eta(x,y) \quad t = t \quad (2)$$

The strong conservation law form under this transformation is retained as, reference [6]:

$$\frac{\partial(U)}{\partial t(J)} + \frac{\partial(F)}{\partial \xi} \left( \frac{\partial \xi}{\partial x} + \frac{G}{J} \frac{\partial \xi}{\partial y} \right) + \frac{\partial(G)}{\partial \eta} \left( \frac{\partial \eta}{\partial x} + \frac{F}{J} \frac{\partial \eta}{\partial y} \right) = 0 \quad (3)$$

where J is the transformation Jacobian

$$\left( \frac{\partial \xi}{\partial x} \right) \left( \frac{\partial \eta}{\partial y} \right) - \left( \frac{\partial \xi}{\partial y} \right) \left( \frac{\partial \eta}{\partial x} \right) \quad (4)$$

In shorthand notation, equation (3) becomes:

$$\hat{U}_t + \hat{F}_\xi + \hat{G}_\eta = 0 \quad (5)$$

where

$$\hat{U} = \frac{U}{J}$$

$$\hat{F} = \frac{F}{J} \xi_x + \frac{G}{J} \xi_y$$

$$\hat{G} = \frac{G}{J} \eta_x + \frac{F}{J} \eta_y$$

$$J = \xi_x \eta_y - \xi_y \eta_x$$

Formal relationships exist between the transformation from (x,y) coordinates to (ξ,η) coordinates and the inverse transformation from (ξ,η) coordinates to (x,y) coordinates which are:

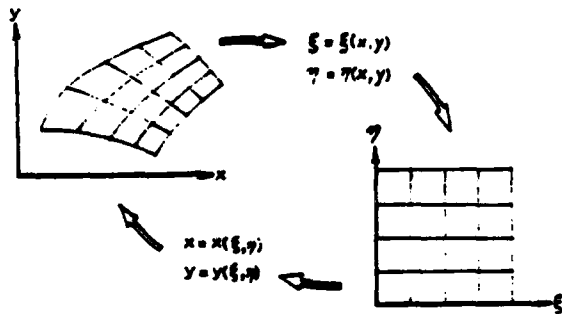


Figure 1. Relationship between transformation from physical to computational space and computational to physical space.

$$x_{,\xi} = \eta_{,y}/J, \quad y_{,\xi} = -\eta_{,x}/J$$

$$x_{,\eta} = -\xi_{,y}/J, \quad y_{,\eta} = \xi_{,x}/J \quad (6)$$

and the inverse Jacobian is

$$J^{-1} = x_{,\xi} y_{,\eta} - x_{,\eta} y_{,\xi} = 1/J$$

The Jacobians express the ratio of cell areas between the different representations.

The transformation metrics (ξ<sub>,x</sub> ξ<sub>,y</sub> η<sub>,x</sub> η<sub>,y</sub>) are most conveniently obtained, suggested by Steger [7], from a finite difference evaluation of these derivatives in computational space using equations (6). This procedure uses only the fact that the coordinate transformation is a one-to-one mapping. If we consider these derivatives to be evaluated by central finite differences, we have, assuming Δξ =

$$\left( \frac{\xi_{,x}}{J} \right)_{j,k} = \delta_k^0 y_{j,k} = \frac{(y_{j,k+1} - y_{j,k-1})}{2} \quad (7)$$

$$\left( \frac{\xi_{,y}}{J} \right)_{j,k} = -\delta_k^0 x_{j,k} = \frac{-(x_{j,k+1} - x_{j,k-1})}{2} \quad (8)$$

$$\left( \frac{\eta_{,x}}{J} \right)_{j,k} = -\delta_j^0 y_{j,k} = \frac{-(y_{j+1,k} - y_{j-1,k})}{2} \quad (9)$$

$$\left( \frac{\eta_{,y}}{J} \right)_{j,k} = \delta_j^0 x_{j,k} = \frac{(x_{j+1,k} - x_{j-1,k})}{2} \quad (10)$$

If we consider the computational cells to be polygons, the exact area of a cell can be determined, see [8], from

$$\text{Area} = \frac{1}{2} \left\{ \sum_{i=1}^N x_i y_{i+1} - \sum_{i=1}^N x_{i+1} y_i \right\} \quad (11)$$

where N is the number of edge nodes, and

$$i+1 = \begin{cases} i+1 & \text{if } i+1 \leq N \\ 1 & \text{if } i+1 > N \end{cases}$$

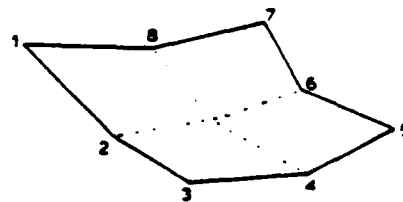


Figure 2. Node connection diagram for general computational cell polygon.

Now consider a possible finite difference representation of equation (5),

$$\left(\frac{\partial U/J}{\partial t}\right)_{j,k}^n = -\delta_j^0 \hat{F}_{j,k} - \delta_k^0 \hat{G}_{j,k} \quad (12)$$

on a standard 9 point cell,

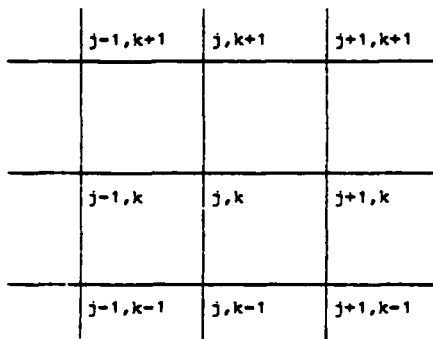


Figure 3. Finite difference node numbering scheme.

$$\begin{aligned} \left(\frac{\partial}{\partial t} (U/J)\right)_{j,k}^n &= -\frac{1}{2} \left\{ \left(F \frac{\xi_x}{J}\right)_{j+1,k} + \left(G \frac{\xi_y}{J}\right)_{j+1,k} \right. \\ &\quad - \left(F \frac{\xi_x}{J}\right)_{j-1,k} - \left(G \frac{\xi_y}{J}\right)_{j-1,k} \\ &\quad + \left(F \frac{\xi_x}{J}\right)_{j,k+1} + \left(G \frac{\xi_y}{J}\right)_{j,k+1} \\ &\quad \left. - \left(F \frac{\xi_x}{J}\right)_{j,k-1} - \left(G \frac{\xi_y}{J}\right)_{j,k-1} \right\} \quad (13) \end{aligned}$$

Now replacing the metric derivatives with their finite difference expressions, equations (7) through (11), and writing out only the continuity equation for clarity, we have

$$\begin{aligned} \left(\frac{\partial \rho/J}{\partial t}\right)_{j,k}^n &= -\frac{1}{4} \left\{ \left[ (\rho u)_{j+1,k}^n (y_{j+1,k+1} - y_{j+1,k-1}) \right. \right. \\ &\quad - (\rho v)_{j+1,k}^n (x_{j+1,k+1} - x_{j+1,k-1}) \\ &\quad - \left[ (\rho u)_{j-1,k}^n (y_{j-1,k+1} - y_{j-1,k-1}) \right. \\ &\quad - (\rho v)_{j-1,k}^n (x_{j-1,k+1} - x_{j-1,k-1}) \\ &\quad + \left[ -(\rho u)_{j,k+1}^n (y_{j+1,k+1} - y_{j-1,k+1}) \right. \\ &\quad \left. \left. + (\rho v)_{j,k+1}^n (x_{j-1,k+1} - x_{j+1,k+1}) \right] \right\} \end{aligned}$$

$$\begin{aligned} & - \left[ -(\rho u)_{j,k-1}^n (y_{j+1,k-1} - y_{j-1,k-1}) \right. \\ & \left. + (\rho v)_{j,k-1}^n (x_{j+1,k-1} - x_{j-1,k-1}) \right] \quad (14) \end{aligned}$$

or

$$\begin{aligned} \left(\frac{\partial (U/J)}{\partial t}\right)_{j,k}^n &= -\left(\delta_j^0 FC_{j,k}^n + \delta_k^0 GC_{j,k}^n\right) \\ &= - (RC)_{j,k}^n \quad (15) \end{aligned}$$

This form of the continuity equation is identical to that which would be obtained by an integration of the control volume fluid equations around the cell area, assuming no variation of  $(\rho u)$  or  $(\rho v)$  across a cell face.

Again using only the continuity equation for clarity,

$$\frac{\partial}{\partial t} \int_{\text{area}} \rho dx dy = - \int_{\text{control surface}} \rho (u \hat{i}_x + v \hat{i}_y) \cdot \bar{n} d\ell \quad (16)$$

where  $\hat{i}_x, \hat{i}_y$  are unit vectors in original Cartesian coordinates,

$\bar{n}$  is an outward normal vector to the cell face, and

$d\ell$  is length along the face.

Equation (16), when expanded, is identical to equation (14), and shows that the proper interpretation of a metric derivative is that the ratio of that derivative to the Jacobian is the projected area of the face. Thus the solution of a finite difference problem in strong conservation law form in a transformed space is equivalent to the solution of a flux summation algorithm expressed in physical space.

The flux sum of equation (13) could be improved by selecting a more accurate approximation for the integral of  $(\rho u)$  or  $(\rho v)$  over a face than simply its value at the center of the face. For example, a piecewise continuous interpretation of  $(\rho u)$  is equivalent to

$$\begin{aligned} \int (\rho u \hat{i}_x) \cdot \bar{n} d\ell &= (u_k^+ (\rho u)_{j,k}) \delta_k^+ y_{j,k} \\ &+ (u_k^- (\rho u)_{j,k}) \delta_k^- y_{j,k} \quad (17) \end{aligned}$$

An important property of equation (14) is that a uniform solution  $\{(\rho u)_{j,k}, (\rho v)_{j,k} \text{ constant over space}\}$  remains identically uniform. This property is generally referred to as area conservation in finite element analysis and its importance to maintaining constant freestream solutions was first pointed out by Steger [7]. A recent paper by Hindman [9] has also emphasized this property.

COMPARISON OF FLUX BALANCE FORM OF SEVERAL TIME-MARCHING ALGORITHMS FOR INVISCID FLOW

Centered Difference Algorithms

METHOD A. Implicit Time-Marching Algorithm of Beam and Warming [1]:

The first method to be considered is the time marching algorithm introduced by Beam and Warming which is unconditionally stable, in the linear problem, for two dimensional flows:

$$\begin{aligned} (I + \Delta t L_{\xi}^I) (I + \Delta t L_{\eta}^I) (\hat{U}_{j,k}^{n+1} - \hat{U}_{j,k}^n) = \\ = - \Delta t (\delta_j^0 FC_{j,k}^n + \delta_k^0 GC_{j,k}^n - L_{\text{SWAV}} \hat{U}_{j,k}^n) \\ = - \Delta t (RC_{j,k}^n - L_{\text{SWAV}} \hat{U}_{j,k}^n) \end{aligned} \quad (18)$$

where  $L_{\xi}^I$  and  $L_{\eta}^I$  are finite difference operators whose form determines the order of accuracy of the time-marching algorithm and  $L_{\text{SWAV}}$  is a finite difference smoothing operator.

Solution Procedure

Step 1:

$$(I + \Delta t L_{\xi}^I) (\hat{\Delta U}_{j,k}^n) = - \Delta t (RC_{j,k}^n - L_{\text{SWAV}} \hat{U}_{j,k}^n) \quad (19)$$

Step 2:

$$(I + \Delta t L_{\eta}^I) \hat{\Delta U}_{j,k}^n = \hat{\Delta U}_{j,k}^n \quad (20)$$

Step 3:

$$\hat{U}_{j,k}^{n+1} = \hat{U}_{j,k}^n + \hat{\Delta U}_{j,k}^n \quad (21)$$

METHOD B. Modified Beam and Warming Algorithm

In order to improve the accuracy of the flux balance operator in skewed mesh systems, a variety of modified Beam and Warming algorithms have been developed. The simplest modified operator, which corresponds to several other algorithms, is to balance the flux on the cell shown below.

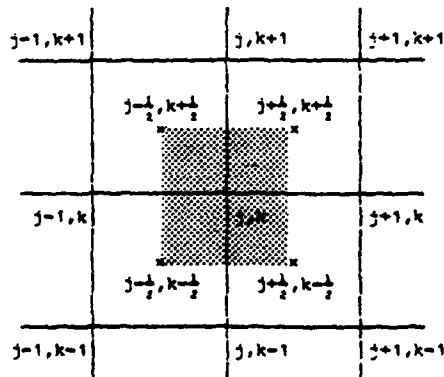


Figure 4. Half-spacing mesh cell in computational space.

The flux balance operator is:

$$RCH_{j,k}^n = \delta_{j/2}^0 (FCH)_{j,k}^n + \delta_{k/2}^0 (GCH)_{j,k}^n \quad (22)$$

where

$$\begin{aligned} (FCH)_{j,k}^n &= \left( u_j^{\pm} F_{j,k}^n \right) \left( u_j^{\pm} \delta_{k/2}^0 y_{j,k} \right) \\ &\quad - \left( u_j^{\pm} G_{j,k}^n \right) \left( u_j^{\pm} \delta_{k/2}^0 x_{j,k} \right) \\ (GCH)_{j,k}^n &= - \left( u_k^{\pm} F_{j,k}^n \right) \left( u_k^{\pm} \delta_{j/2}^0 y_{j,k} \right) \\ &\quad + \left( u_k^{\pm} G_{j,k}^n \right) \left( u_k^{\pm} \delta_{j/2}^0 x_{j,k} \right) \end{aligned}$$

and the algorithm becomes

$$\begin{aligned} (I + \Delta t_{j,k} L_{\xi}^I) (I + \Delta t_{j,k} L_{\eta}^I) (\hat{U}_{j,k}^{n+1} - \hat{U}_{j,k}^n) \\ = - \Delta t_{j,k} (RCH)_{j,k}^n - L_{\text{SWAV}} \hat{U}_{j,k}^n \end{aligned} \quad (23)$$

METHOD C. Explicit Time Integration Scheme of Jameson [3] and Rizzi [4]:

The Runge-Kutta time stepping approach can be expressed as:

$$\frac{d\hat{U}_{j,k}}{dt} = - RCH_{j,k}^n + L_{\text{RKAV}} \hat{U}_{j,k}^n = - P\hat{U}_{j,k}^n \quad (24)$$

Step 1:

$$\hat{U}^{(0)} = \hat{U}_{j,k} \quad (25)$$

Step 2:

$$\hat{U}^{(1)} = \hat{U}^{(0)} - \left( \frac{\Delta t}{2} \right)_{j,k} P\hat{U}^{(0)} \quad (26)$$

Step 3:

$$\hat{U}^{(2)} = \hat{U}^{(1)} - \left( \frac{\Delta t}{2} \right)_{j,k} P\hat{U}^{(1)} \quad (27)$$

Step 4:

$$\hat{U}^{(3)} = \hat{U}^{(1)} - \Delta t_{j,k} P\hat{U}^{(2)} \quad (28)$$

Step 5:

$$\begin{aligned} \hat{U}^{(4)} = \hat{U}^{(0)} \\ - \left( \frac{\Delta t}{6} \right)_{j,k} \left( P\hat{U}^{(0)} + 2P\hat{U}^{(1)} + 2P\hat{U}^{(2)} + P\hat{U}^{(3)} \right) \end{aligned} \quad (29)$$

Step 6

$$\hat{U}_{j,k}^{n+1} = \hat{U}^{(4)} \quad (30)$$

This method is usually run with the smoothing operator in each step formed as  $L_{RKAV} \hat{U}^n$  rather than  $L_{RKAV} \hat{U}^{(i)}$ .

If steps 2, 3, 4, 5 each converge independently, then the steady state solution is identical to that of the modified Beam and Warming, method B, if  $L_{BWA} = L_{RKAV}$ , and the solution is independent of  $\Delta t_{j,k}$ .

METHOD D. Flux Balance Form of MacCormack's Method (2):

A flux balance form of MacCormack's method may be expressed as:

Step 1, Predictor:

$$\begin{aligned} \hat{U}_{j,k}^* &= \hat{U}_{j,k}^n - \Delta t_{j,k} \left[ \left( F_{j+1,k}^{n,PLy1} - G_{j+1,k}^{n,PLx1} \right) \right. \\ &- \left( F_{j,k}^{n,PLy3} - G_{j,k}^{n,PLx3} \right) \\ &+ \left( - F_{j,k+1}^{n,PLy4} + G_{j,k+1}^{n,PLx4} \right) \\ &- \left( - F_{j,k}^{n,PLy2} + G_{j,k}^{n,PLx2} \right) \\ &\left. - L_{MAV} \hat{U}_{j,k}^n \right] \end{aligned} \quad (31)$$

where the projected lengths are

$$\begin{aligned} PL_{y1} &= u_j^+ \delta_{k/2}^0 y_{j,k} = y_{j+\frac{1}{2},k+\frac{1}{2}} - y_{j+\frac{1}{2},k-\frac{1}{2}} \\ &\vdots \\ PL_{x4} &= u_k^+ \delta_{j/2}^0 x_{j,k} = x_{j+\frac{1}{2},k+\frac{1}{2}} - x_{j-\frac{1}{2},k+\frac{1}{2}} \end{aligned}$$

Step 2, Corrector:

$$\begin{aligned} \hat{U}_{j,k}^{**} &= \hat{U}_{j,k}^* - \Delta t_{j,k} \left[ \left( F_{j,k}^{*,PLy1} - G_{j,k}^{*,PLx1} \right) \right. \\ &- \left( F_{j-1,k}^{*,PLy3} - G_{j-1,k}^{*,PLx3} \right) \\ &+ \left( - F_{j,k}^{*,PLy4} + G_{j,k}^{*,PLx4} \right) \\ &- \left( - F_{j,k-1}^{*,PLy2} + G_{j,k-1}^{*,PLx2} \right) \\ &\left. - L_{MAV} \hat{U}_{j,k}^* \right] \end{aligned} \quad (32)$$

Step 3:

$$\hat{U}_{j,k}^{n+1} = \frac{1}{2} \left( \hat{U}_{j,k}^* + \hat{U}_{j,k}^{**} \right) \quad (33)$$

Step 3 may be rewritten as

$$\begin{aligned} \hat{U}_{j,k}^{n+1} &= \hat{U}_{j,k}^n \\ &- \frac{\Delta t_{j,k}}{2} \left[ \left( (F_{j+1,k}^n + F_{j,k}^*) (u_j^- \delta_{k/2}^0 y_{j,k}) \right) \right. \\ &- \left( G_{j+1,k}^n + G_{j,k}^* (u_j^+ \delta_{k/2}^0 x_{j,k}) \right) \\ &- \left( (F_{j,k}^n + F_{j-1,k}^*) (u_j^- \delta_{k/2}^0 y_{j,k}) \right) \\ &- \left( G_{j,k}^n + G_{j-1,k}^* (u_j^- \delta_{k/2}^0 x_{j,k}) \right) \\ &+ \left( - (F_{j,k+1}^n + F_{j,k}^*) (u_k^+ \delta_{j/2}^0 y_{j,k}) \right) \\ &+ \left( G_{j,k+1}^n + G_{j,k}^* (u_k^+ \delta_{j/2}^0 x_{j,k}) \right) \\ &- \left( - (F_{j,k}^n + F_{j,k-1}^*) (u_k^- \delta_{j/2}^0 y_{j,k}) \right) \\ &+ \left( G_{j,k}^n + G_{j,k-1}^* (u_k^- \delta_{j/2}^0 x_{j,k}) \right) \\ &\left. - L_{MAV} (\hat{U}_{j,k}^n + \hat{U}_{j,k}^*) \right] \end{aligned} \quad (34)$$

This form of MacCormack's method is area preserving for each step (31 or 32) and offers the possibility of steady state solutions which are independent of  $\Delta t$ . When the predictor and corrector step both converge, which we generally find to be the case, then the steady state form of equation (34) is:

$$RCH_{j,k}^n - L_{MAV} \hat{U}_{j,k}^n = 0 \quad (35)$$

as with the modified Beam and Warming and fourth order Runge-Kutta schemes, methods B and C.

Comments on Centered Difference Algorithms

For each of the methods considered, A, B, C and D, the steady state solution desired is that the centered differenced flux balancing residual  $(RC)_{j,k}^n$  or  $(RCH)_{j,k}^n$  is zero. For all these schemes at interior points, this criterion is possible only when the artificial smoothing operators are neglected. The order of accuracy of all these methods is the same and each should be expected to produce nearly the same steady state solution except for differences in smoothing requirements or boundary conditions. As we shall see in the test examples, this conclusion can be demonstrated by numerical experiments.

Non-Centered Difference Algorithms

METHOD E. MacCormack's Method on a Non-Centered Cell Basis:

A version of MacCormack's method which does a flux sum on the cell structure shown in Figure 5 has been developed by Tong (10). This form is a

two or three dimensional extension of the strong conservation law version of MacCormack's method proposed by Hindman [9]. This scheme uses the same basic nine point cell as in Figure 3 or 4, but it computes a flux sum over each of the four interior cells.

Step 1:

$$U_{j,k}^* = U_{j,k}^n - \Delta t_{j,k} \left( (RMC)_{j+\frac{1}{2},k+\frac{1}{2}}^n - LMACV U_{j,k}^n \right) \quad (36)$$

Step 2:

$$U_{j,k}^{**} = U_{j,k}^* - \Delta t_{j,k} \left( (RMC)_{j-\frac{1}{2},k-\frac{1}{2}}^* - LMACV U_{j,k}^* \right) \quad (37)$$

Step 3:

$$U_{j,k}^{n+1} = \frac{1}{2} \left( U_{j,k}^n + U_{j,k}^{**} \right) \quad (38)$$

or

$$U_{j,k}^{n+1} = U_{j,k}^n - \frac{\Delta t_{j,k}}{2} \left( (RMC)_{j+\frac{1}{2},k+\frac{1}{2}}^n + (RMC)_{j-\frac{1}{2},k-\frac{1}{2}}^n - LMACV \left( U_{j,k}^n + U_{j,k}^{**} \right) \right) \quad (39)$$

where

$$(RMC)_{j\pm\frac{1}{2},k\pm\frac{1}{2}}^n = \frac{\delta_j^\pm (FM)_{j,k}^n + \delta_k^\pm (GM)_{j,k}^n}{\Delta_{j\pm\frac{1}{2},k\pm\frac{1}{2}}} \quad (40)$$

$$(FM)_{j,k}^n = F_{j,k}^n \delta_k^\pm y_{j,k} - G_{j,k}^n \delta_k^\pm x_{j,k} \quad (41)$$

$$(GM)_{j,k}^n = -F_{j,k}^n \delta_j^\pm y_{j,k} + G_{j,k}^n \delta_j^\pm x_{j,k} \quad (42)$$

$\Delta_{j\pm\frac{1}{2},k\pm\frac{1}{2}}$  is the area of 4-point cell.

This form of MacCormack's method also obeys geometric area conservation on the 4-point cells with the possibility of a steady state solution that is independent of  $\Delta t$ . Both the predictor and corrector steps can individually converge. The predictor and corrector steps express flux conservation on the 4-point cells and, if each  $(RMC)_{j,k}$  converges to zero, then we have global flux conservation.

METHOD F. Ni's Lax-Wendroff Method [5]:

Ni's method may be expressed in a one step form as:

$$U_{j,k}^{n+1} = U_{j,k}^n - \Delta t_{j,k} \left( \mu_j^0/2 \mu_k^0/2 (RMC)_{j,k}^n \right) + \frac{\Delta t_{j,k}^2}{2} \left\{ \mu_k^0/2 \delta_j^0/2 \left[ \left( \frac{\partial FNI}{\partial U} \right) \left( \frac{\partial RMC}{\partial U} \right) \right]_{j,k}^n + \mu_j^0/2 \delta_k^0/2 \left[ \left( \frac{\partial GNI}{\partial U} \right) \left( \frac{\partial RMI}{\partial U} \right) \right]_{j,k}^n \right\} + LMACV U_{j,k}^n \quad (43)$$

where

$$(RNI)_{j\pm\frac{1}{2},k\pm\frac{1}{2}}^n = \frac{1}{\Delta_{j\pm\frac{1}{2},k\pm\frac{1}{2}}} \left[ \delta_j^\pm (FNI)_{j,k\pm\frac{1}{2}}^n + \delta_k^\pm (GNI)_{j\pm\frac{1}{2},k}^n \right] \quad (44)$$

$$(FNI)_{j,k\pm\frac{1}{2}}^n = \left( \mu_k^\pm F_{j,k}^n \right) \left( \delta_k^\pm y_{j,k} \right) - \left( \mu_k^\pm G_{j,k}^n \right) \left( \delta_k^\pm x_{j,k} \right) \quad (45)$$

$$(GNI)_{j\pm\frac{1}{2},k}^n = - \left( \mu_j^\pm F_{j,k}^n \right) \left( \delta_j^\pm y_{j,k} \right) + \left( \mu_j^\pm G_{j,k}^n \right) \left( \delta_j^\pm x_{j,k} \right) \quad (46)$$

This representation of Ni scheme, which is not the computational form, is a Lax-Wendroff type method which does a flux sum on 4-point cells. A possible solution to the steady state form of equation (43) is that each  $(RNI)_{j\pm\frac{1}{2},k\pm\frac{1}{2}}^n$  becomes zero in the absence of artificial smoothing.

Comments on Non-Centered Schemes

Both the Tong and the Ni non-centered schemes compute flux balances on the 4-point cells and each solution can be consistent with these balances,  $(RMC)_{j\pm\frac{1}{2},k\pm\frac{1}{2}}^n$  or  $(RNI)_{j\pm\frac{1}{2},k\pm\frac{1}{2}}^n$  becoming zero in the absence of smoothing. Thus the Tong and Ni schemes should produce approximately the same steady-state solution, if the same boundary conditions are applied. The two steady state flux balance operators are not identical. We would expect Ni's scheme to produce a more accurate result in the absence of artificial smoothing, but his method may require more smoothing than Tong's method.

INVISCID TEST EXAMPLES

Three configurations were chosen as test examples. The first case was the bump in a channel problem introduced by Ni [5]; the second was a supersonic nozzle with a rapid isentropic expansion; and the third was a supercritical stator designed by Sanz [11]. For each problem, an exact steady state solution would be isentropic with constant stagnation pressure, stagnation temperature and mass flow rate. Methods are compared on the basis of predicted Mach number distributions and stagnation pressure loss over the domain. For all methods on all problems, the mass flow rate was conserved to within 0.3%.

Boundary Conditions

Inflow/outflow boundary conditions were of the non-reflecting characteristic or extrapolation type, but implementation details differed greatly from method to method. We believe that the results presented are as free as possible from contamination due to these conditions.

It was impossible to maintain exactly the same hard wall boundary conditions between the schemes. Methods A and B, which were developed strictly for viscous flow by the authors, used only a simple pressure and parallel velocity extrapolation for the inviscid case. These conditions were sufficient for the first two cases but not the supercritical stator case. The proper conditions for Ni's method are not clear. The first two examples for Ni's method predicted surface quantities from the interior point scheme and then corrected these quantities by a simple one-dimensional wave to maintain flow tangency.

Methods C, D, and E used boundary procedures which consistently satisfied

$$\text{normal momentum} \quad \frac{\partial p}{\partial n} = \frac{\rho q^2}{R} \quad (47)$$

$$\text{where } q^2 = u^2 + v^2$$

and R is the radius of curvature of the surface

$$\text{streamwise momentum} \quad \frac{\partial p}{\partial s} = -\rho \frac{\partial(q^2/2)}{\partial s} \quad (48)$$

where s is the arc length along surface

$$\text{flow tangency} \quad v/u = \delta_j y / \delta_j x \quad (49)$$

at each point on the boundary. To satisfy all three conditions at each point on the boundary requires an iterative evaluation of the boundary pressures at each time-marching step. This procedure is costly but is essential for simulations with minimum stagnation pressure error.

#### Artificial Smoothing Operators

For methods A, B, D, and F, the smoothing operators were generally as proposed by their authors with the smoothing coefficients "tuned-up" for each calculation. For methods C, D, and E, the calculation procedure was:

$$U^* = [I - RSPB]U^n \quad (50)$$

$$U^{**} = [I + S_x]U^* \quad (51)$$

$$U^{n+1} = [I + S_y]U^{**} \quad (52)$$

where RSPB is the flux balance operator and  $S_x, S_y$  are the smoothing operators

$$S_x U = f [U_{j+1} + U_{j-1} - 2U_j] \quad (53)$$

$$f = \frac{f_1}{1+f_2} \left[ 1 + \frac{f_2}{\Delta x / \Delta x_{min}} \right] \quad (54)$$

$$f_1 = 0.1 \quad f_2 = 200.$$

For methods C and D, these smoothing operators were applied after each step, but for method E they were applied only after the last step.

The steady state solutions are not independent of the smoothing operators, but every effort was made to reduce their effect.

#### CONVERGENCE CRITERION

For all of the methods except Tong's, the convergence criterion was easy to establish. The computed solutions were run until the steady state flux balance operator plus the smoothing operator converged to a specified value,  $1.0 \times 10^{-5}$  maximum at any point and  $1.0 \times 10^{-6}$  root mean square value.

In Tong's method, as with any MacCormack type method, the order of differencing in predictor and corrector steps is not unique. The double sawtooth solutions common to central difference schemes can be reduced by cyclically permuting the operator sequence. The disadvantage of this process plus the smoothing sequence adopted is that we lose the ability to drive a steady state residual below about  $1.0 \times 10^{-4}$  maximum local value and about  $1.0 \times 10^{-5}$  root mean square value. It is thus difficult to determine when to stop iterating on a solution, and we must supply some heuristic principle to determine when to stop. The advantage of this process is that the stagnation pressure errors in the "converged" solution are greatly reduced.

#### Ni Bump Test Case, Subsonic Flow

All of the methods produced acceptably accurate solutions for the channel bump problem especially in terms of symmetry and Mach number predictions. The grid used contained 65X17 points and is illustrated in Figure 5 along with a typical Mach number contour plot. The predicted top and bottom wall Mach numbers for each method are shown in Figure 6. The stagnation pressure loss for each of the methods is shown in Figure 7. All of the centered schemes produced essentially the same pressure loss of about 2% max  $\Delta P_t/P_t$ . The non-centered schemes produced essentially no loss. On balance, all the schemes performed adequately on the bump case.

#### Supersonic Nozzle Test Case

The supersonic nozzle test case geometry and grid is shown in Figure 8. This grid has 65X33 points. The inflow Mach number is 2.0, and an idealized wave diagram is also shown in Figure 8. The wave diagram shows that the wall outflow Mach number should be 2.83, and that the Mach number should be uniform in region 1. The idealized wave diagram does not account for curvature of the characteristics as the wave system from the lower wall interacts with the upper wall wave system. Under this assumption the exit centerline Mach number should be 2.625. The results for each of the schemes is shown in Figure 9 in terms of Mach number contours. The correct wave system is adequately predicted by all schemes. The stagnation pressure loss contours for this test case are all shown in Figure 10. The centered schemes all have unacceptable losses in the range of 1% to 4%. Ni's scheme has a small loss while the non-centered MacCormack has virtually no loss. It is likely that a better hard wall boundary condition treatment with Ni's method would eliminate the loss shown.

The agreement between the 4 centered schemes is quite remarkable; in fact, as would be expected from the analysis, all schemes produce nearly the same steady state solutions. The non-centered MacCormack and Ni's scheme produce quite similar results.

#### Supercritical Stator Test Case

A much more demanding geometry is the supercritical stator design presented by Sans [11]. The grid for this test case is shown in Figure 11. A simple sheared grid was used for simplicity which required a fine grid near the blade leading edge for accurate simulations.

The surface Mach number predictions for the supercritical stator using the Tong's non-centered MacCormack type method are shown in Figure 12. The agreement is satisfactory except at 8% chord on the suction surface. Slight variations in the specified downstream pressure specified produced overshoots or undershoots in this region. The sample calculation is for the downstream pressure specified by Sans. We are simply unsure of the reason for this discrepancy. The stagnation pressure loss for this calculation is shown in Figure 13. An unacceptably high loss of 14% exists locally at the stagnation point and a maximum loss of 4% exists on the suction surface.

The centered MacCormack scheme performed nearly the same on the Sans blade as is shown in Figure 14. The stagnation pressure loss at the leading edge is locally 14% and a maximum of 4% in the remainder of the domain.

#### VISCOUS TURBINE CALCULATION EXAMPLE

While the results from the supercritical stator geometry illustrate that accurate Euler equation solutions can be obtained, the situation is less clear for viscous flow problems. To illustrate our level of computational abilities for these flows, a calculation of the flow in a high speed, high turning turbine cascade is presented. The numerical method used is similar to the approximate factorization method of Beam-Warming [1] except that the flux balance operator uses trapezoidal rule integration, as in equation (17), on the computational cell of Figure 4. Local values of  $\Delta t$  are used to produce a constant local CFL number of about 4. Details of this algorithm will be available in reference [12]. Solutions for turbine geometries generally require about 500 iterations to converge to machine accuracy, 6 decimal digits.

The experimental results and geometric details for the cascade were made available in reference [13], and the geometry is shown in Figure 15. The turning is 126 degrees with an outflow Mach number of 0.75. The design Reynolds number is 500000. All calculations assumed laminar flow.

The computational results are presented in Figures 16 and 17. The first figure compares predicted blade surface pressure to the experimental values for a laminar calculation at design Reynolds number. The grid chosen has 100x29 points and is nearly orthogonal at each node point.

Predicted results are quite sensitive to the grid resolution. Reasonably accurate surface pressures were predicted everywhere including the stagnation point and the trailing edge. The maximum stagnation pressure error outside the boundary layer was about 1%. We are as yet unable to explain the discrepancy at 7% chord on the suction surface although we believe it to be linked to the trailing edge flow field.

The predicted trailing edge flow field is illustrated in Figure 17 in terms of velocity direction vectors. This calculation shows two small separation zones comparable in size to the trailing edge radius. While the predicted flow field at the trailing edge seems reasonable, we have no way to verify its accuracy.

#### CONCLUSIONS AND DISCUSSION

The presentation of the time-marching schemes in terms of a flux balancing interpretation and the inviscid computational examples shows that the six schemes analyzed are quite similar in their steady state solution properties. While the computational details of the schemes are very different, the steady state solutions of the central difference schemes are nearly identical. Computational details of the non-centered schemes are also quite different, but they again produce similar steady state solutions.

A consistent result throughout the evaluations was that the non-centered schemes produced lower stagnation pressure errors than did the centered schemes. Since entropy conservation or stagnation pressure conservation is not a conservation property of the finite difference equations, we expect these errors to be a function of the truncation errors present in the solution. The truncation error appears as an entropy generation, and the stagnation pressure error is the entropy error raised to the  $\gamma/(\gamma-1)$  power. Stagnation pressure loss is a very sensitive measure of the entropy generation in a scheme.

The grid sizes for the inviscid problems were chosen to produce small stagnation pressure errors for the non-centered schemes, and the centered schemes nearly always produced larger errors on the same grid. We attribute this result either to the space averaging properties of the solution operators or to artificial smoothing to eliminate double sawtooth errors.

Accurate Euler flow simulations are possible with the non-centered schemes as was shown by the supercritical stator example. Both methods reproduced the shock-free solution with a minimum of effort, and both produced only a small stagnation pressure loss on the test grid. With a locally refined, orthogonal grid, the total number of grid points required can be reduced to a more manageable number. Our ability to compute accurate viscous flow solutions is increasing rapidly. The turbine cascade solution is for a moderately difficult geometry, and the computational results are reasonable. Much more work must be done in this area before we can compute viscous solutions as accurately as for inviscid situations.

ACKNOWLEDGEMENT

Major sponsors for this evaluation were the Air Force Office of Scientific Research under the direction of Dr. James D. Wilson, contract number F49620-78-C-0084; the Office of Naval Research under the direction of Dr. Albert Wood, contract number W00014-81-K-0024; and Rolls-Royce Inc. The supercritical cascade data were furnished by Dr. R.V. Chima and J. Sans of NASA Lewis Research Center. The turbine cascade data were furnished by Rolls-Royce Ltd. and the British Ministry of Defence (Procurement Executive).

REFERENCES

- [1] Beam, R. M. and Warning, R. F., "An Implicit Factored Scheme for the Compressible Navier-Stokes Equations," *AIAA Journal*, Vol. 16, No. 4, April 1978, pp. 393-402.
- [2] MacCormack, R. W. and Paullay, A. J., "Computational Efficiency Achieved by Time Splitting of Finite Difference Operators," *AIAA Paper 72-154*, 1972.
- [3] Jameson, A., Schmidt, W. and Turkel, E., "Numerical Solutions to the Euler Equation by Finite Volume Methods Using Runge-Kutta Time Stepping," *AIAA Paper 81-1259*, June 1981.
- [4] Rizzi, A. and Eriksson, L. E., "Transfinite Mesh Generation and Damped Euler Equation Algorithms for Transonic Flow Around Wing-Body Configuration," *AIAA Paper 81-0999*, June 1981.
- [5] Ni, R. H., "A Multiple Grid Scheme for Solving the Euler Equation," *AIAA paper 81-1025*, June 1981.
- [6] Viviani, H., "Conservation Forms of Gas Dynamic Equations," *Recherche Aerospatiale*, No. 1, January 1974, pp. 65-68.
- [7] Steger, J. L., "Implicit Finite-Difference Simulation of Flow about Arbitrary Two-Dimensional Geometries," *AIAA Journal*, Vol. 16, No. 7, July 1978, pp. 679-686.
- [8] *CRC Handbook of Standard Mathematical Tables*, 21st Edition, edited by S. M. Selby, 1973, p. 369.
- [9] Hindman, R. G., "Generalized Coordinate Forms of Governing Fluid Equations and Associated Geometrically Induced Errors," *AIAA Journal*, Vol. 20, No. 10, October 1981, pp. 1359-1367.
- [10] Tong, S. S., Ph.D. thesis in preparation. Dept. Aero and Astro., Mass. Inst. of Tech., Cambridge, MA.
- [11] Sans, J., private communication
- [12] Bush, R.H., Ph.D. thesis in preparation. Dept. Aero and Astro, Mass. Inst. of Tech., Cambridge, MA.
- [13] private communication from Rolls-Royce Ltd.

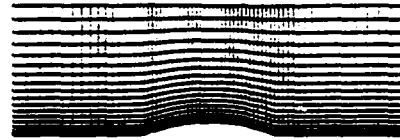


Figure 5a. 65 x 17 grid for Ni bump test case

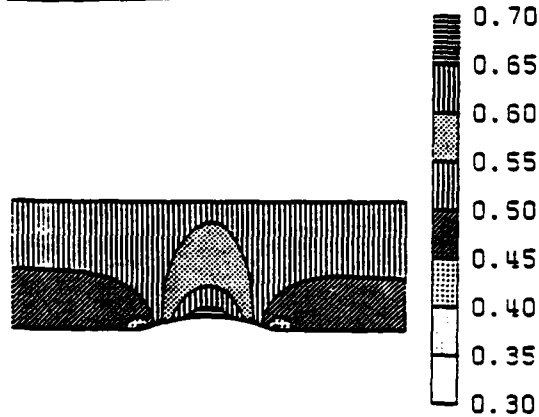


Figure 5b. Mach number contour plot for Ni bump

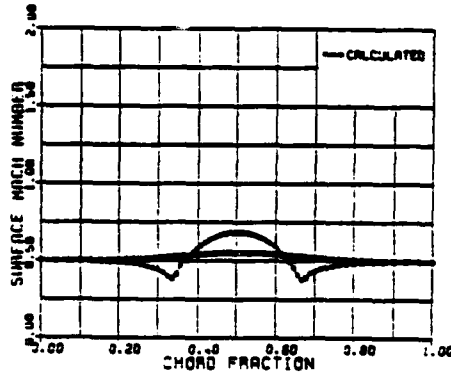


Figure 6a. Surface Mach number, Ni bump, Beam Warming method

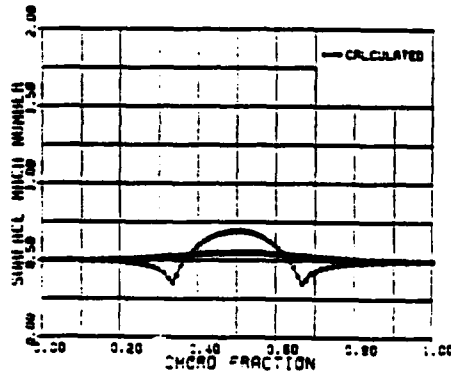


Figure 6b. Surface Mach number, Ni bump, modified Beam-Warming method

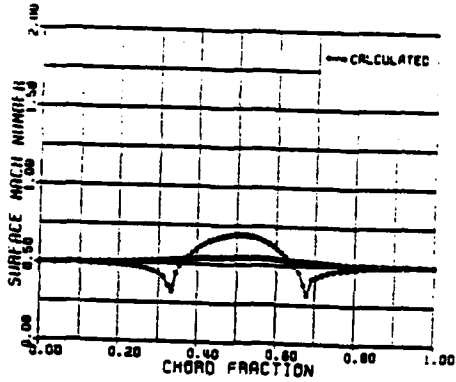


Figure 6c. Surface Mach number, Ni bump, centered MacCormack method

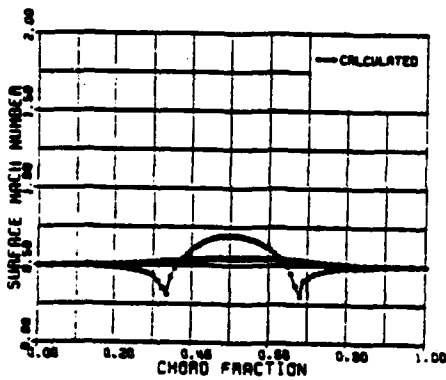


Figure 6d. Surface Mach number, Ni bump, Jameson-Rizzi method

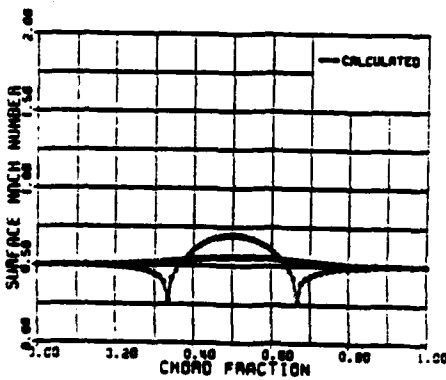


Figure 6e. Surface Mach number, Ni bump, non-centered MacCormack method

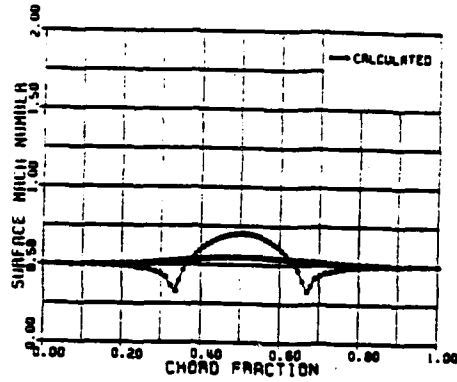


Figure 6f. Surface Mach number, Ni bump, Ni's method

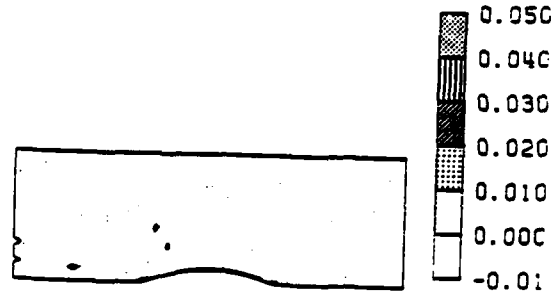


Figure 7a. Stagnation pressure error contour plot, Beam-Warming method

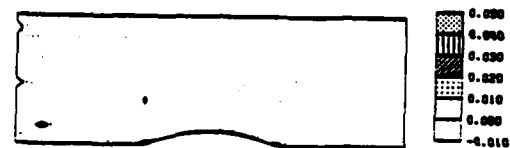


Figure 7b. Stagnation pressure error contour plot, modified Beam-Warming method

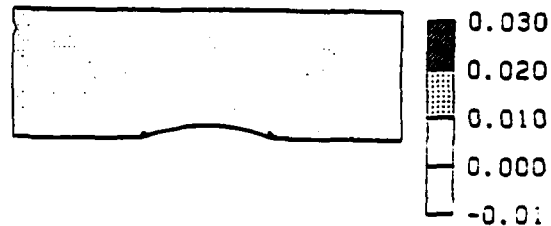


Figure 7c. Stagnation pressure error contour plot, centered MacCormack method

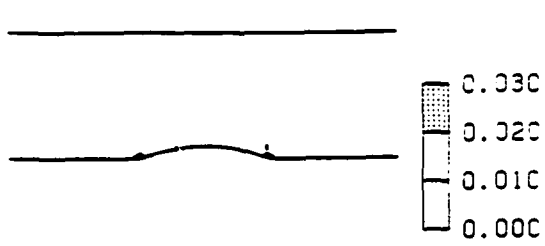


Figure 7d. Stagnation pressure error contour plot, Jameson-Rizzi method

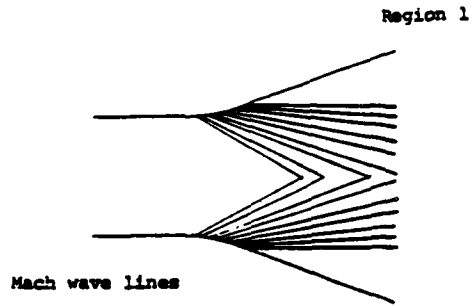


Figure 8b. Idealized wave diagram for supersonic nozzle

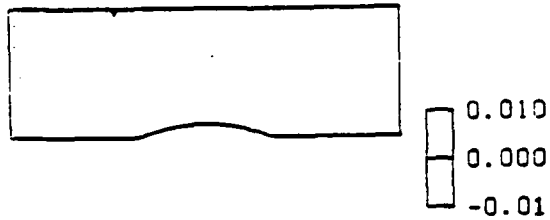


Figure 7e. Stagnation pressure error contour plot, non-centered MacCormack method



Figure 7f. Stagnation pressure error contour plot, Mi's method

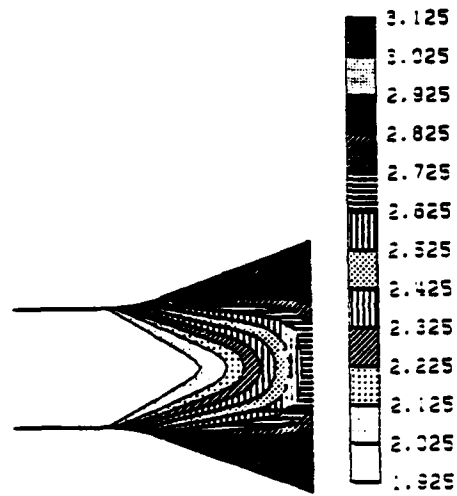


Figure 9a. Mach number contour plot, supersonic nozzle, Beam-Warming method

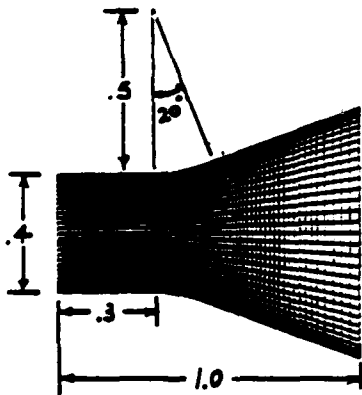


Figure 8a. 65x33 grid for supersonic nozzle test case

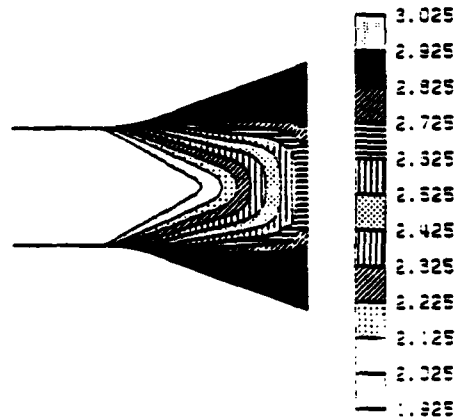


Figure 9b. Mach number contour plot, supersonic nozzle, modified Beam-Warming method

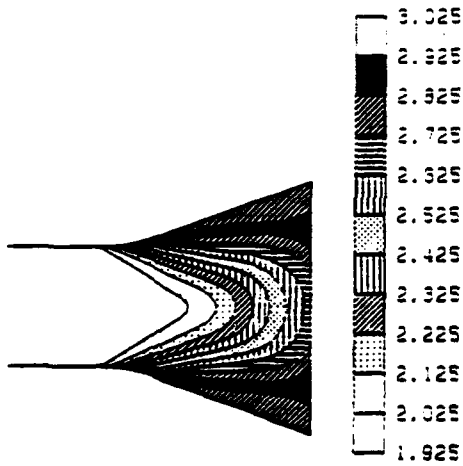


Figure 9c. Mach number contour plot, supersonic nozzle, centered MacCormack method

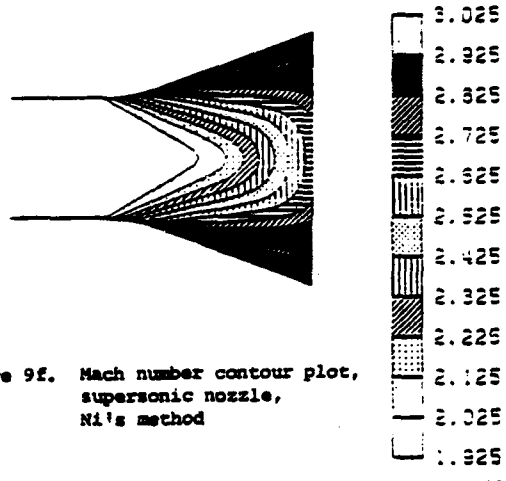


Figure 9f. Mach number contour plot, supersonic nozzle, Ni's method

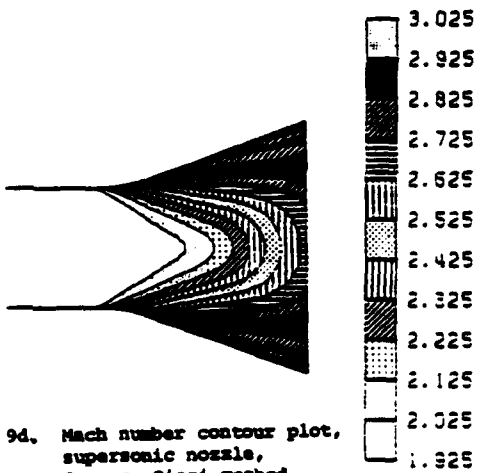


Figure 9d. Mach number contour plot, supersonic nozzle, Jameson-Rizzi method

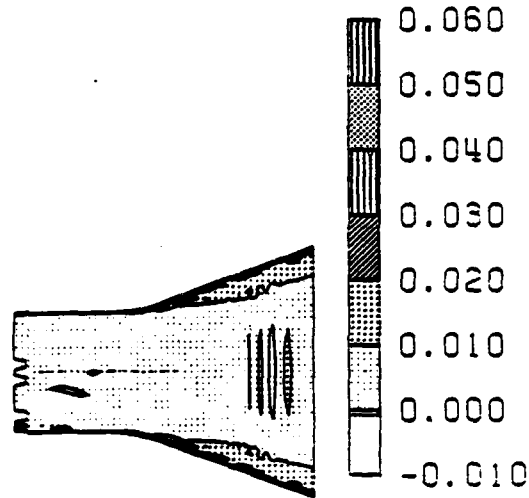


Figure 10b. Stagnation pressure error contour plot, modified Beam-Warming method

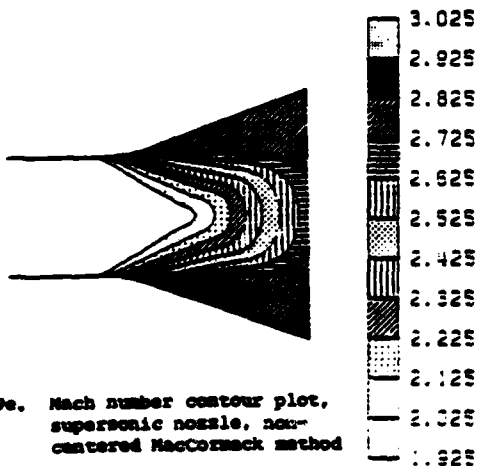


Figure 9e. Mach number contour plot, supersonic nozzle, non-centered MacCormack method

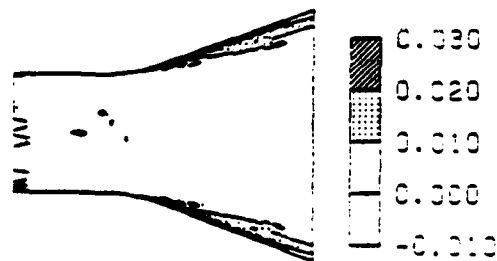


Figure 10a. Stagnation pressure error contour plot, Beam-Warming method

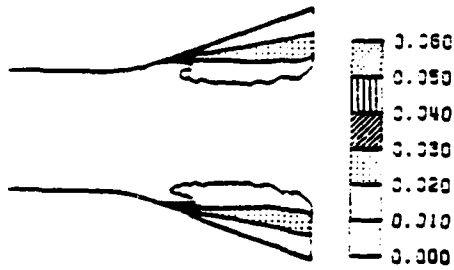


Figure 10c. Stagnation pressure error contour plot, centered MacCormack method

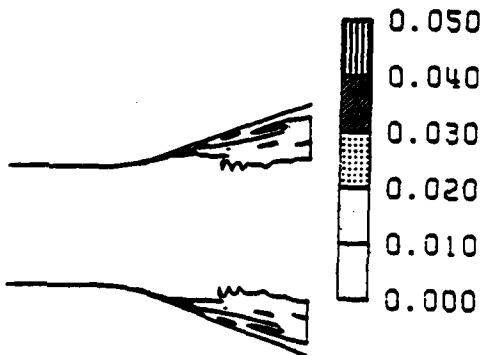


Figure 10d. Stagnation pressure error contour plot, Jameson-Rizzi method

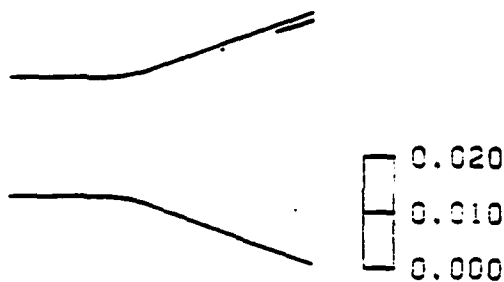


Figure 10e. Stagnation pressure error contour plot, non-centered MacCormack method

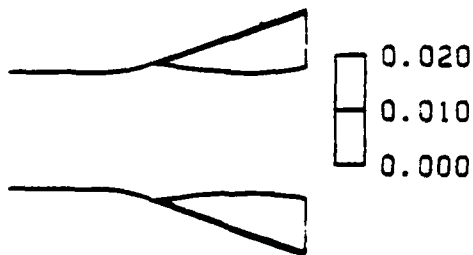


Figure 10f. Stagnation pressure error contour plot, NI's method



Figure 11. 73x34 grid for supercritical stator

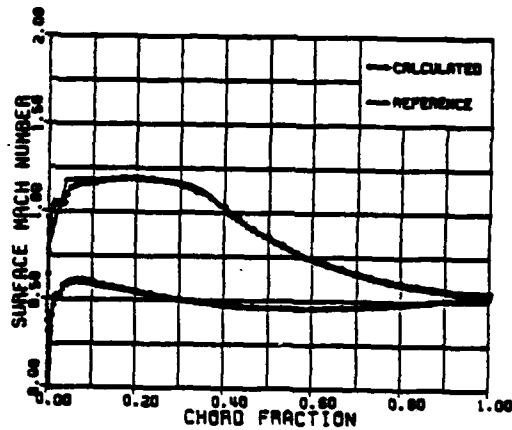


Figure 12 Surface Mach number comparison for non-centered MacCormack's method, supercritical stator

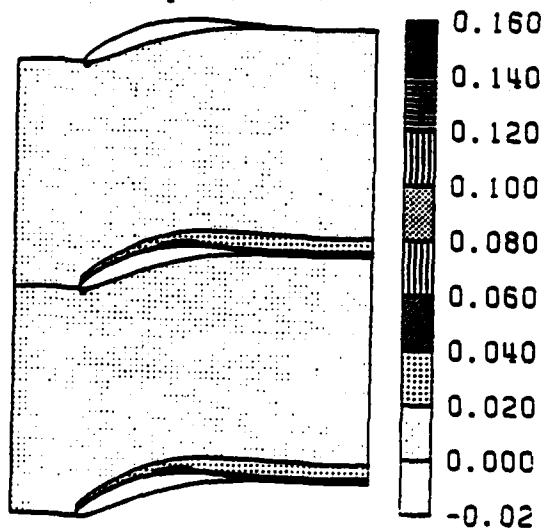


Figure 13 Stagnation pressure error contour plot, non-centered MacCormack's method, supercritical stator

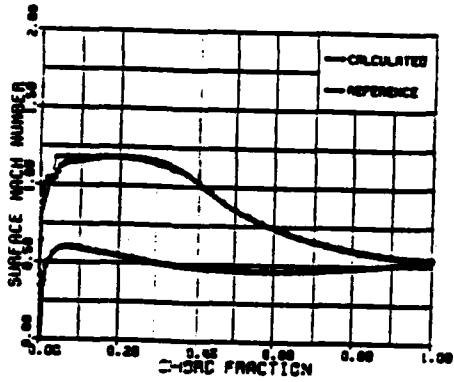


Figure 14a Surface Mach number comparison for centered MacCormack's method, supercritical stator

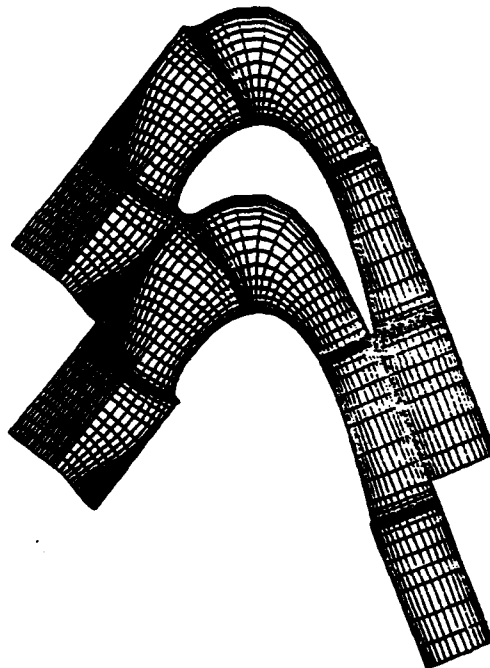


Figure 15 100 x 29 grid for turbine stator

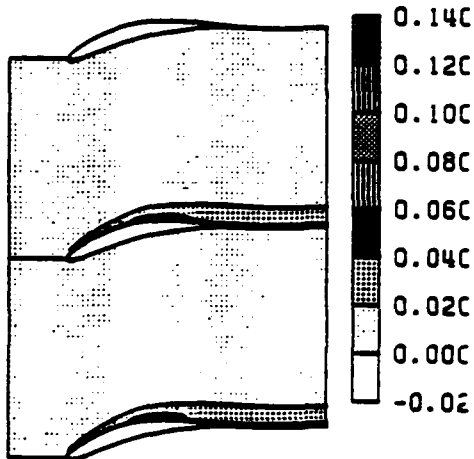


Figure 14b Stagnation pressure error contour for centered MacCormack's method, supercritical stator

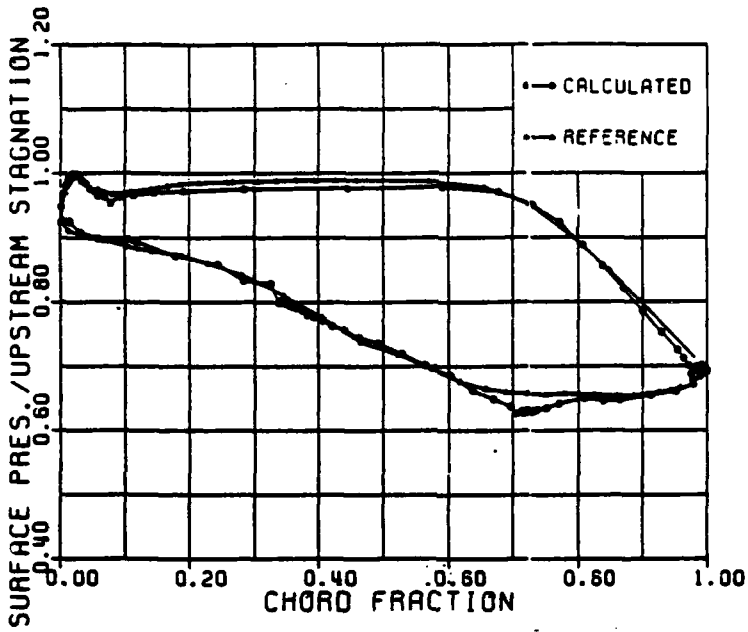


Figure 16 Blade surface static pressure comparison for turbine stator

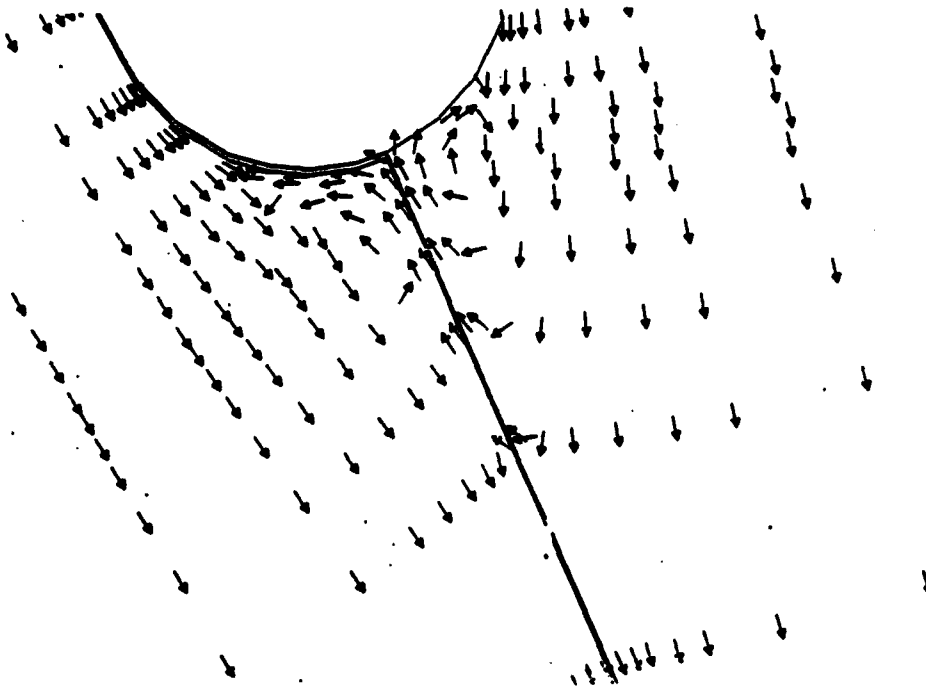


Figure 17 Velocity vector direction plot for turbine stator trailing edge region

TASK I B: ADVANCED MEASUREMENTS IN TRANSONIC COMPRESSORS

Introduction

This research effort is aimed at elucidating design point operation loss mechanisms of high work, high mass flow transonic compressor stages. In particular, the Air Force Aero Propulsion Laboratory High Through Flow (HTF) stage is being examined in the M.I.T. Blowdown Compressor Facility.

The M.I.T. Gas Turbine Laboratory has developed a unique capability for measuring the time dependent three-dimensional flow field of transonic compressors. Using fast response semi-conductor diaphragm pressure transducers mounted on traversing probes, the time dependent flow fields upstream and downstream of the blade rows can be mapped. This had been done previously for the MIT stage and a NASA 20-inch diameter high aspect ratio compressor stage and is continuing on the AFAPL 17-inch diameter HTF stage.

In all of the above aerodynamic measurements, the efficiency of each stage was obtained by direct measurement of stagnation pressure together with a calculated stagnation temperature. This temperature was found using the Euler equation and the measured tangential Mach number. This calculation rests on the assumptions: 1) that the flow is steady in coordinates rotating with the rotor, and 2) that there is no exchange of energy between stream-tubes (in rotor coordinates) due to work done by viscous forces or due to heat transfer. Both of these assumptions are known from qualitative observations to be not completely correct, but in the absence of a direct measurement of the

stagnation temperature at the rotor exit it has not been possible to relax the assumptions in treating the details of the rotor outflow.

For this reason, we have started work on a technique to measure the fluctuating total temperature in the Blowdown Compressor as described below.

Time Resolved Total Temperature Probe: Principle of Operation

Time resolved measurement of gas total temperature has always been a difficult task. Conventional thermocouples lose frequency response above 1 KHZ. Compensated thermocouples [1.1] have yet to be successfully demonstrated. Spectroscopic techniques using flows seeded with NO [1.2, 1.3], or 2,3 butanedione [1.4] show promise as sensitive non-intrusive tools. They require, however, high power, narrow band lasers for excitation at pulse rates sufficient to resolve the flow field. For transonic compressors where significant flow detail occurs at frequencies above 10 KHZ, commercial light sources are not presently available.

We have decided to take a somewhat simpler approach to the problem in the interests of returning information on the compressor flowfield more rapidly than might result from the more elegant but also more complicated spectroscopic techniques. We have developed a dual wire aspirating probe which should allow measurement of both total temperature and total pressure at frequencies above 10 KHZ. Conventional hot wires measure the thermal energy lost by convection to the fluid. They are thus sensitive to the wire/fluid temperature difference  $(T_w - rT_f)$  and the mass flux,  $\rho U$ , by the wire, where

$T_w$  is the wire temperature,  $T_T$ , the fluid total temperature;  $r$  the recovery factor;  $\rho$  the fluid density, and  $U$  the fluid velocity. Since the voltage from a constant temperature hot wire is proportional to the square root of the power dissipated in the fluid.

$$V^2 = f(\rho U)(T_w - rT_T) \quad (1)$$

In a transonic compressor, all the flow quantities fluctuate temporally, so that  $\rho$ ,  $U$ ,  $T_T$ , and  $P_T$  (the fluid total pressure) are functions of time, thus making conventional hot wire data exceedingly difficult to interpret for this flowfield. To overcome this problem, we have placed two coplanar hot wires in the 1.5mm diameter channel of an aspirating probe (figure 1.1). Since the convergent exit of the channel is choked, the mass flux ( $\rho U$ ) is now a function only of free stream total temperature ( $T_T$ ) and total pressure ( $P_T$ ), assuming gas composition is constant. Thus, equation (1) may be written as

$$V^2 = f(P_T/\sqrt{T_T})(T_w - rT_T) \quad (2)$$

In order to verify that the aspirating probe does not display the usual hot wire sensitivity to velocity fluctuations, the response, of the probe and of an isolated hot wire, to the vortex shed from a right circular cylinder were compared. When the cylinder was unheated, the hot wire responded to the velocity fluctuations but the aspirating probe did not (figure 1.2). When the wire is heated,

however, the probe responded to the temperature fluctuations, thus confirming the performance of the probe to first order.

Treating the hot wire as a right circular cylinder and adopting the functional form of the heat transfer suggested by Collis and Williams [1.5]. Thus, equation 2 becomes

$$V^2 = [C_1 (P_T/\sqrt{T_T})^n + C_2] (T_w - rT_T) \quad (3)$$

where  $C_1$ ,  $C_2$ ,  $n$  are constants to be determined by calibration (although our measured values are in good agreement with those of [1.5]).

#### Steady State Probe Calibration

As for any instrumentation, the quality of the data can be no better than the accuracy of the calibration. Initial checks of the aspirating probe operation were performed in a 2.5cm diameter heated free air jet in which the total pressure (Mach number) and the total temperature could be varied independently. The range of Mach number variation is 0 to 1.0 and of total temperature 20°C to 150°C. Thus, probe calibration in air could be established. Also, frequency response was roughly estimated by using the vortex shed from a heated right circular cylinder as excitation. This excitation frequency could be varied up to about 8 KHZ by changing the velocity.

The initial use of the probe, however, is in the M.I.T. Blowdown Compressor Tunnel which uses an argon-freon-12 mixture with a ratio of specific heats of 1.4 as the working fluid. Thus, a test rig was

constructed to facilitate calibration with this gas composition (figure 1.3). The test rig is a blowdown facility using the tanks of the blowdown compressor as source and vacuum dump. The supply tank is heated by an atmospheric pressure steam jacket up to 100°C. The probe is tested in a one inch diameter channel terminated by a choked orifice. The Mach number in the channel is varied by changing the orifice diameter. The test channel is heated in order to inhibit the growth of a thermal boundary layer. The momentum boundary layer thickness at the probe position is approximately 10% of the channel diameter. The data which follows was taken at a channel Mach number of 0.19.

The calibration procedure is to take data by varying the tank stagnation pressure at constant stagnation temperature while operating at a particular wire overheat ratio. The conditions surveyed include the operating range of the Blowdown Compressor facility. A typical calibration curve is presented in figure 1.4. The constants,  $C_1$ ,  $C_2$ , and  $n$  are determined by a nonlinear least squares data fit.

The calibration repeatability appears to be better than 0.1% in voltage which would correspond to approximately 0.4% in adiabatic efficiency. The very good agreement between the constants derived from calibration runs at different temperatures implies that interpolation is sufficient for any intermediate temperature.

In practice, the probe data is reduced with an iterative routine using the experimental calibration curves. This routine was checked by simultaneous solution of equation (3) for each wire. This gave identical results.

As a further check on probe operation, a semiconductor diaphragm (Kulite XCQ-093) total pressure probe has been mounted "piggyback" on the probe. The total pressure probe has the same inlet diameter as the aspirating probe and is immediately adjacent to it. Thus, total pressure is measured in two ways. To date, however, the fluctuating component of these total pressures does not agree well (which will be discussed later).

#### Limits to Performance

The design of the dual wire aspirating probe is an engineering compromise between spatial resolution (small size) and hot wire constraints (wire L/D); and angular acceptance and frequency response. The hot wire length to diameter ratio must be kept large (above 200) in order for thermal end effects to be small. Since the smallest practical hot wires are 0.1 to 0.2 mils in diameter, the channel diameter must be larger than 1mm. Because of anemometer stability problems, a 0.25 mil diameter wire is used and the channel diameter is 1.5mm. This is also consistent with construction constraints. In order to ensure that both wires exhibit similar sensitivity, the ends of the wires are copper plated so as to equalize the active length of each wire to within 1%.

During operation in the blowdown tunnel, a shift in D.C. calibration of 0.2 to 0.5% was noted after each run. This is believed due to the deposition of the detonation products (mostly fine carbon) of the plastic explosive used to start the tunnel. Careful washing of the wires in distilled water after each run returned the original calibration. This is troublesome since most wire breakage occurs during handling. A future solution may be a shutter or cap on the wall cavity in which the probe resides during the explosion.

The basic assumption concerning the operation of the probe is that both wires are immersed in the same uniform flowfield. It is only to the degree that this condition holds true that the probe can yield meaningful results. This assumption can be violated in two ways. One is that flowfield contains disturbances whose length scales are small compared to the probe diameter. This is certainly true but may not be significant. The second problem would arise when the flow angle into the probe is large enough to induce separation. One way of improving the probe's response to off angle and small scale disturbances would be to increase the L/D of the channel before the wires, thus mixing out the non-uniformities. This approach cannot be taken, however, because the growth of the resultant thermal boundary layer would damp out the high frequency components of interest. The present design was chosen to keep the thermal boundary layer height at the wire plane below 10% of the channel diameter. The off-angle response of the probe has been checked to  $\pm 20^\circ$  with no deviation noted.

Another assumption in the data analysis is that the channel flow in the probe behaves in a steady state quasi-1D manner. This was checked by examining the solution to the time dependent continuity and momentum equations for the conditions relevant to the probe's operation. No significant deviation from the steady state assumption was apparent.

An additional limit to performance is the basic signal to noise ratio of each hot wire. At the present low total pressure required for steady state (i.e. constant corrected speed and weight flow) operation in the blowdown tunnel, the blade wake temperature excess is only four times the noise level. For this reason, the temperature derived from using the piggyback Kulite total pressure probe (which has relatively little noise) and any one of the two wires gives a more accurate reading than the temperature derived from both wires together. This problem was recognized after the data presented herein was taken and will be improved in a later data set. Also, the inlet total pressure will be doubled with the flywheel installed, thus also increasing the signal to noise of the probe.

The final constraint on confirmation of overall probe accuracy is the lack of an accurate high frequency calibration of the aspirating probe. The shed vortex method is qualitative at best since Reynolds number constraints limit the size of cylinder and thus the wake. Although the time dependent continuity analysis indicates that channel flow acts as though in steady state, experimental verification is strongly desirable. Unfortunately, it is extremely difficult to generate a well-characterized strongly fluctuating flow field at

frequencies upward of 1 KHZ. We are presently considering several methods of accomplishing this including a two-foot diameter chopper disk and a high speed "lawn sprinkler" concept. In both cases, these are complex, high speed rotating devices requiring careful mechanical and aerothermal design. Plans are now to construct such a device during the next year.

#### Preliminary Measurements

The aspirating probe has been used to survey the outflow of the AFAPL High Through Flow (HTF) rotor. The rotor is operated with the probe inserted in a stator gap directly behind the rotor. The probes are traversed from tip to hub in 15 to 20 ms. These measurements were all made before the installation of the flywheel on the HTF rotor. Thus, the corrected speed changes approximately 1.5% during the test time.

The spanwise distribution of total pressure ratio across the rotor is presented in figure 1.5. The total pressure probe is the semiconductor unit mounted piggyback on the aspirating probe. The four-way probe is a high frequency cylinder probe illustrated in figure 1.6. The AFAPL stator L.E. refers to conventional steady state pitot probes located along the stator leading edge. These are conventional measurements taken at AFAPL. For the two high frequency measurements, the data are time averages. Note that the agreement among the measurements is not very close. This difference is of the

order of 3-5% at a given spanwise location. Discrepancies between steady state and time resolved data have been noted before [1.6] (although not necessarily explained).

Evidence from ongoing testing at NASA Lewis Research Center suggests that the spanwise pressure distribution of a transonic compressor may continuously vary to some degree, even though the average operating point is steady. To explore this, surveys using the total pressure probe during three nominally identical runs is shown in figure 1.7. Although the curves have generally the same shape and average to the same total pressure, the particular value at any spanwise location may vary by as much as 3% from test to test.

Another aspect of this variation can be seen in figure 1.8 which shows the wall static pressure approximately 0.2 chord upstream of the tip. Here, the waveforms have the same overall shape but are clearly not identical at the few percent level. (The traces are displaced vertically for clarity.) This is somewhat surprising since the blow-down tunnel should be an extremely repeatable facility for compressor testing (even the small acoustic disturbances in the supply tank are identical from test to test). Even if time resolved transonic compressor behavior is unsteady, it should be repeatable in the blow-down facility. It is suggested that the variation observed in these three tests is due to differences in the initial angular position of the rotor at the instant the test starts. Thus, the flow variations would be a function of three variables -- blade-to-blade variations (and thus rotor angular position), inflow perturbations, and any inherent rotor unsteadiness. Exactly in what manner these three

phenomena interact is not well understood at this time but is a matter of continuing research. In an attempt to understand the causes of the test-to-test variation in the blowdown compressor, future tests will be started with the rotor at identical (to 1/40 blade spacing) angular positions. It is believed that this should substantially reduce this variation (although not the unsteadiness).

With the level of test-to-test variation in mind, we can now compare the measurements from different probes at the same location during different tests. Time resolved measurements of rotor outflow total pressure is presented in figure 1.9 for probes of differing configurations and size. The sphere probe is approximately 5mm in diameter; the four-way cylinder probe, 3mm; the total pressure probe with a Kulite XCQ-093 transducer, 3mm; and the total pressure probe with a Kulite XCQ-063, 2mm. The D.C. levels are the same but the traces have been displaced vertically for clarity. As would be expected, the frequency response improves as the probe size is reduced. More importantly, however, the symmetry of the waveform changes, especially near the tip, as the probe size is reduced. Thus, conclusions as to blade-to-blade flow details must be made with extreme caution. The time average of these signals vary no more than the test-to-test differences shown in figure 1.7. Further exploration of the probe size effect will include construction of a 1.2mm diameter high frequency total pressure probe. Also, any high frequency calibration facility constructed for use with the aspirating probe will also be utilized to check the other aerodynamic probes.

Comparison of the spanwise distribution of the time average of the total temperature a) measured with the aspirating probe and b) inferred using the Euler Turbine Eq. from angle measurements made with the four-way cylinder probe is shown in figure 1.10. The resultant adiabatic efficiency is shown in figure 1.11. It is important to note that these averages differ no more than the test-to-test flow variation. Thus, on a time averaged basis, one may conclude that the Euler Equation is an accurate approximation of the rotor flow.

This is not necessarily the case for the blade-to-blade flow detail shown in figures 1.12-1.14. Here, ten blade ensemble averages of the flow near the nub, midspan, and tip are presented along with their respective power spectral densities. In this case, the difference in the blade-to-blade variation is significant even though the average flow quantities are equal. In the case of the tip measurement ( $R/R_t = 0.95$ ) much of the variation is due to differences in the total pressure waveform, perhaps due to probe size effects mentioned earlier. This is not the case for the inner stations, however, where the variation is principally in the total temperatures. Thus, the Euler Equation may not be an accurate representation of the time resolved flow field. Further analysis work is planned in this area.

Plans for Future Work

Efforts for the next reporting period include both further testing and analysis. The HTF rotor will be retested with the recently acquired flywheel installed. This will reduce the corrected speed and weight flow variations to less than 0.5% and also increase the Reynolds number by a factor of two.

A high frequency calibration facility will be designed and constructed to test the frequency response of the aspirating and other probes. Also, work will proceed on improving the signal-to-noise ratio of the aspirating probe. Analysis on the data will continue with emphasis placed on understanding the implications of the time resolved temperature data.

REFERENCES

- 1.1 Elmore, D., "Dynamic Gas Temperature Measurement System," in Turbine Engine Hot Section Technology, NASA TM83022, Oct. 1982.
- 1.2 Gross, K.P., McKenzie, R.L., "The Two-Photon Absorptivity of Rotational Transitions in the  $A^2\Sigma^+(v'=0)-X^2\Pi(v''=0)$  Gama Bands of Nitric Oxide," J. Chem. Physics **76** (11), 1 June 1982, pp. 5260-5266.

- 1.3 McKenzie, R.L., and Gross, K.P., "Two Photon Excitation of Nitric Oxide Fluorescence as a Temperature Indicator in Unsteady Gas-dynamic Processes," Applied Optics, Vol.20, No.12, June 1981, pp. 2153-2165.
- 1.4 Epstein, A.H., "Fluorescent Visualization for Turbomachine Research," M.I.T. Gas Turbine Lab Report 142, March 1978.
- 1.5 Collis, D.C., and Williams, M.J., "Two-Dimensional Convection From Heated Wires at Low Reynolds Numbers," Journal of Fluid Mechanics, vol. 6, pp. 357 (1959).
- 1.6 Epstein, A.H., et al., "Time Resolved Measurements In a Low Aspect Ration Transonic Compressor Stage," ASME Paper 82-GT-201, April 1982.

# ASPIRATING PROBE

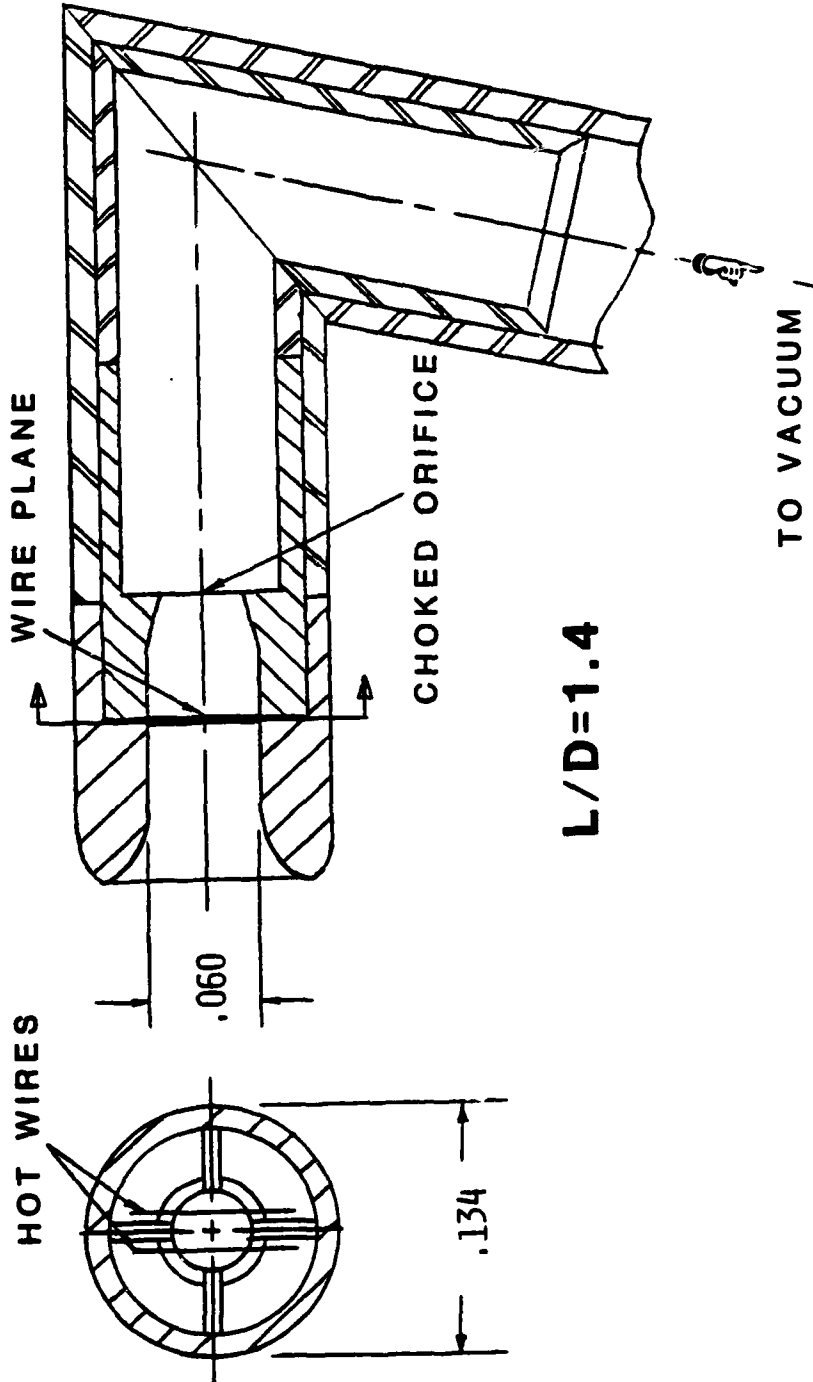


Fig. 1.1 -- Aspirating Probe (dimensions are in inches)

# UNHEATED VORTEX STREET

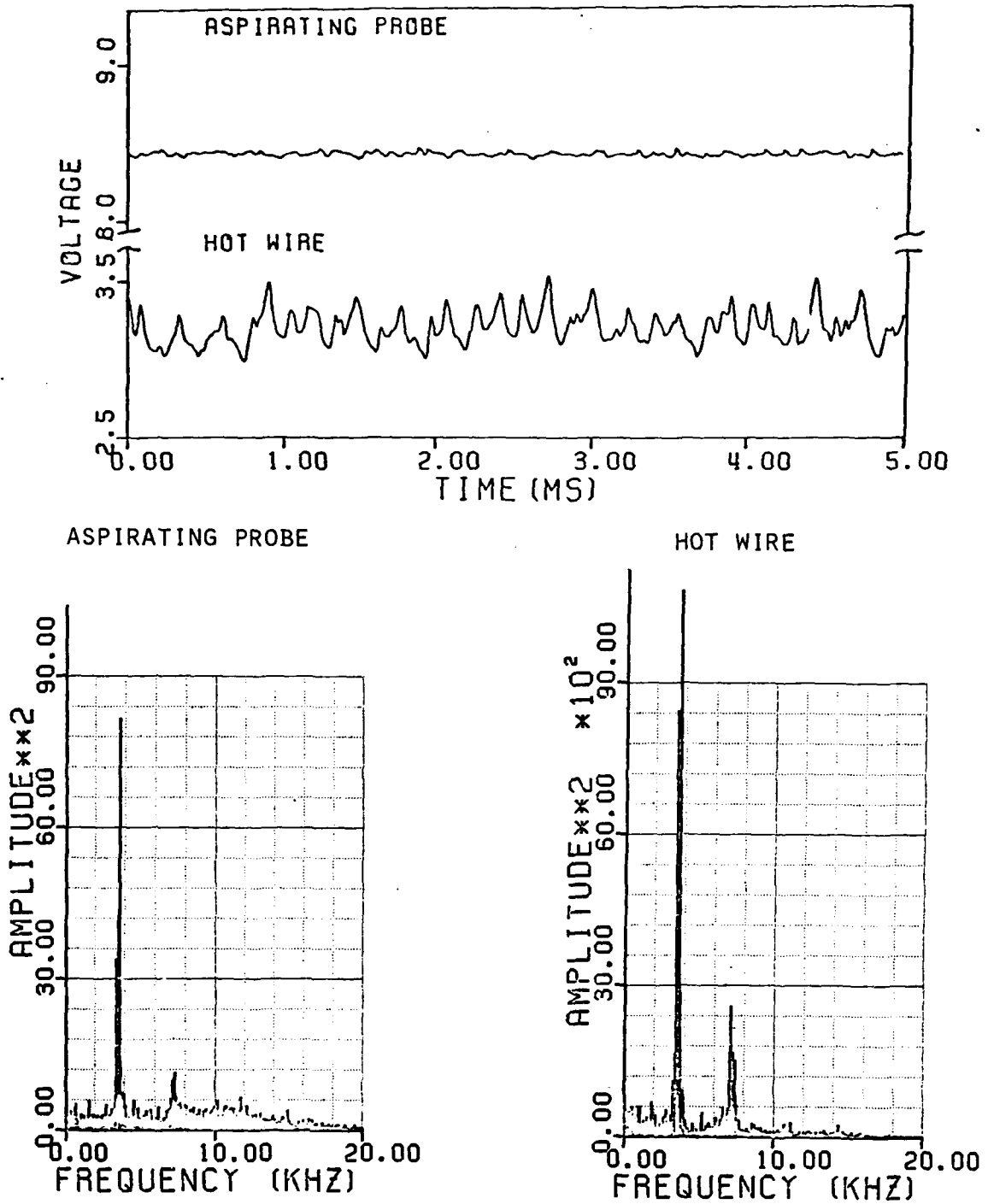


Fig. 1.2a -- Probe vs. hot wire response in a vortex sheet shed by an unheated cylinder.

# HEATED VORTEX STREET

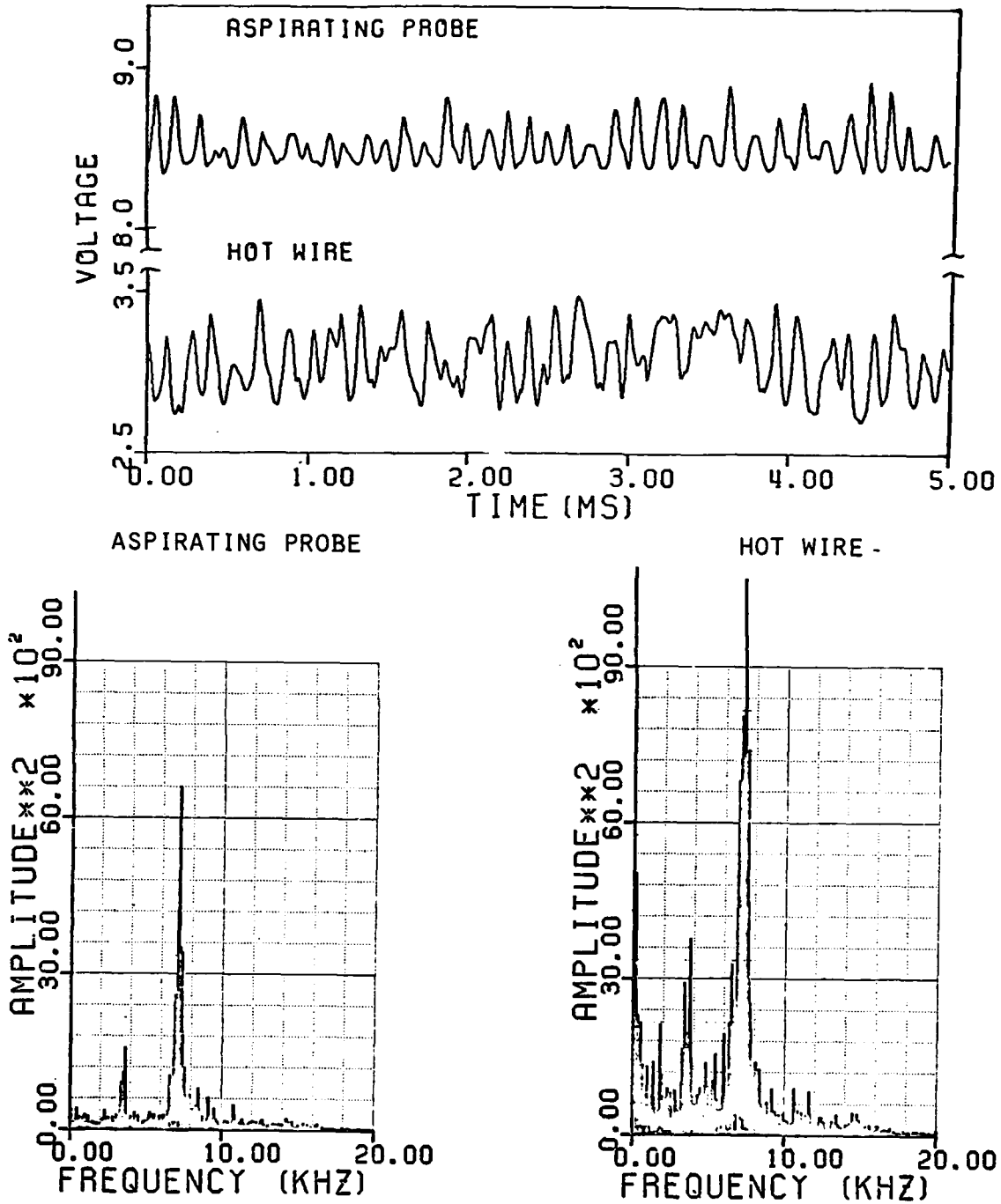
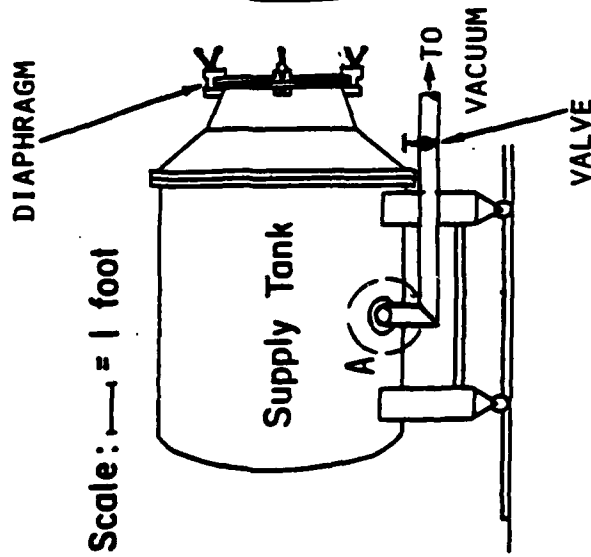
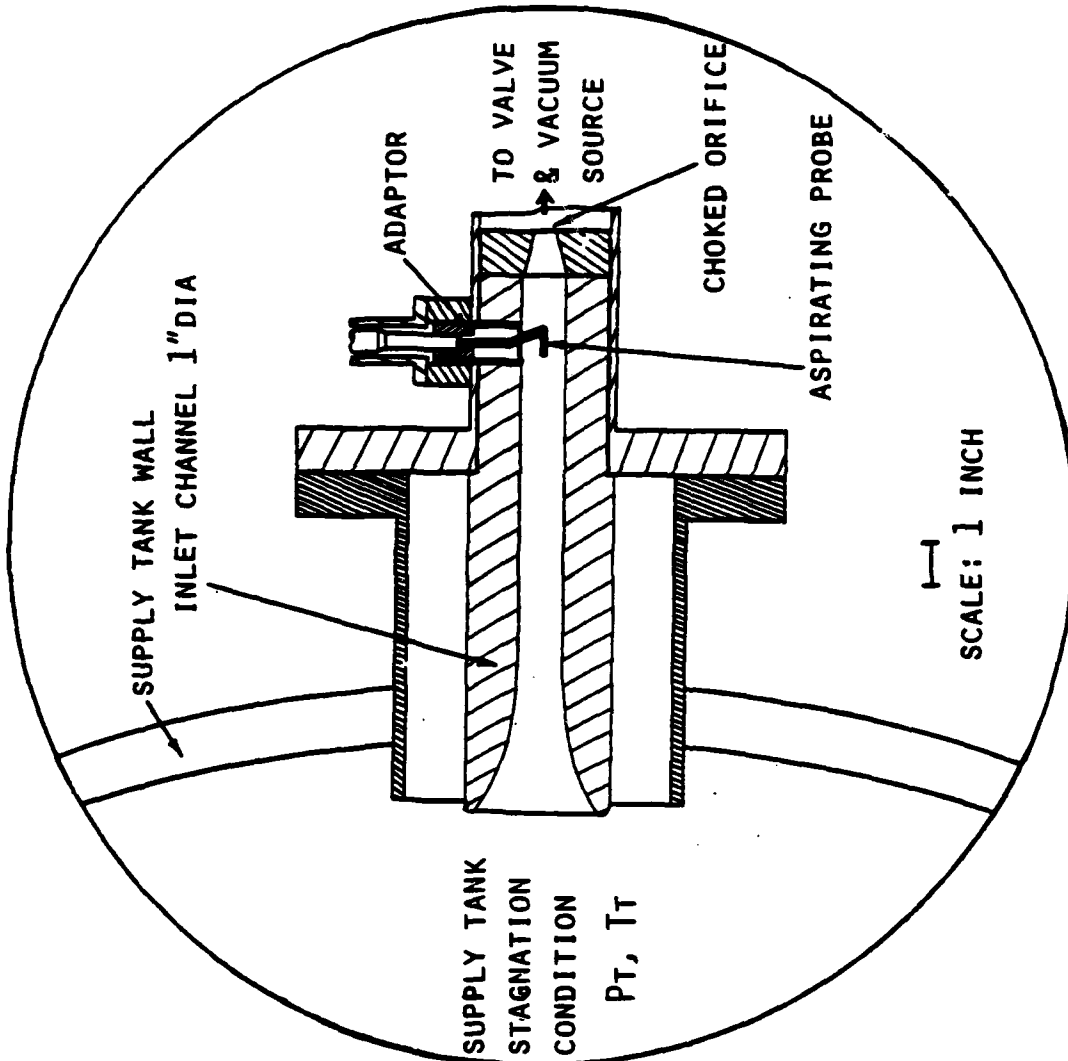


Fig. 1.2b -- Probe vs. hot wire response in a vortex sheet shed by a heated cylinder.



DETAIL "A"

Fig. 1.3 -- Scale Drawing of Aspirating Probe Calibration Facility.

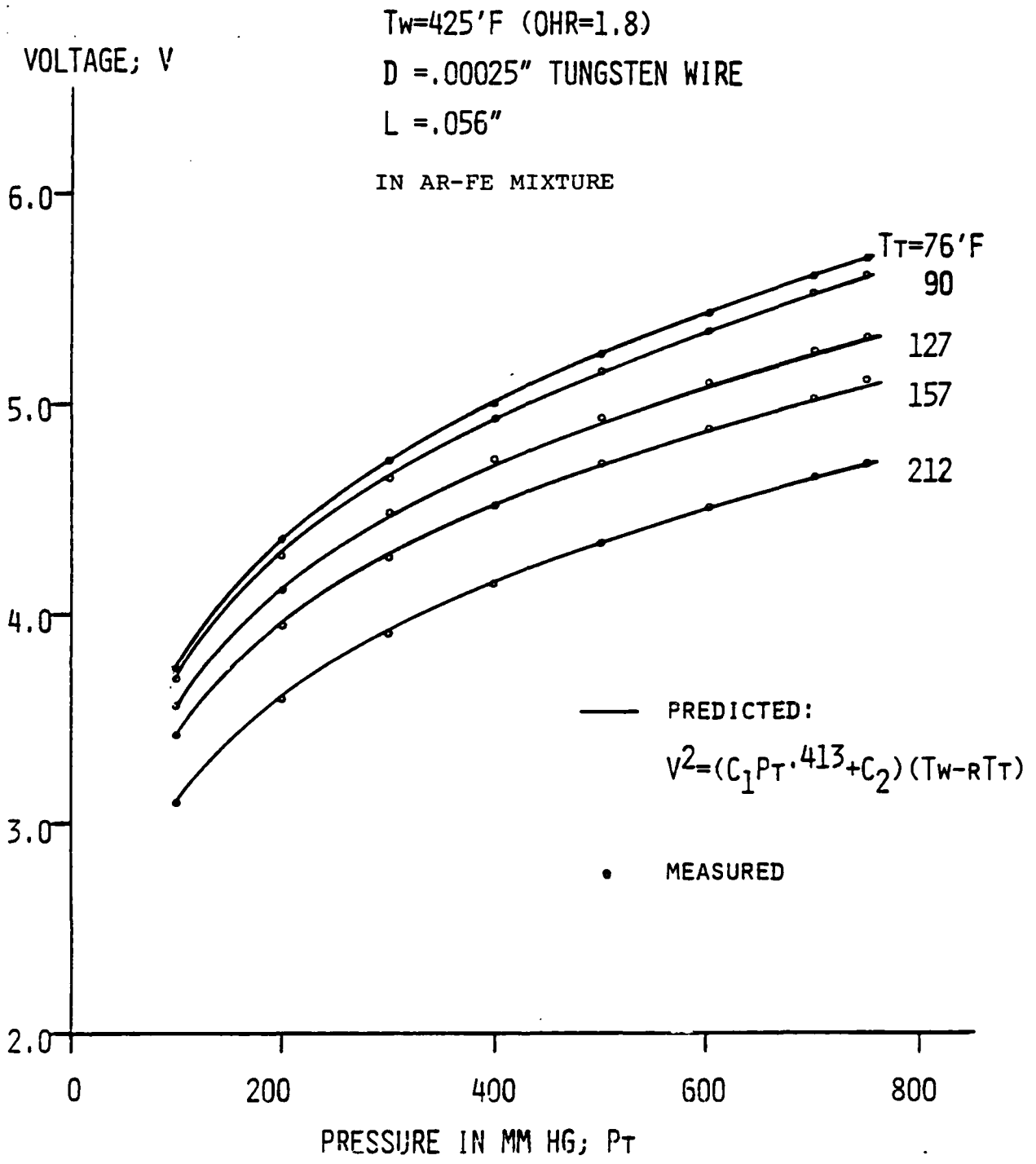


Fig. 1.4 -- D.C. wire calibration in argon and freon-12.

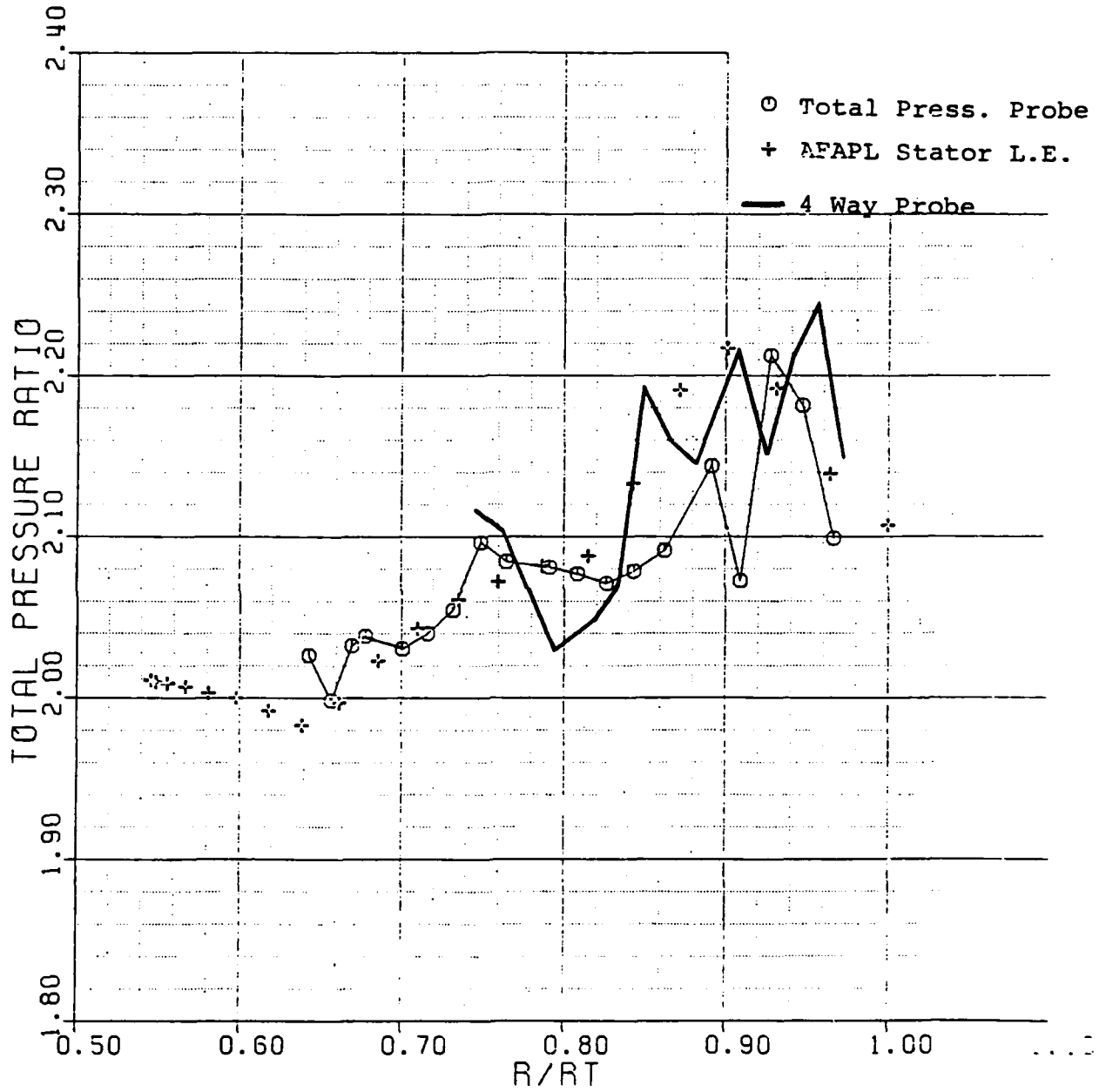


Fig. 1.5 -- Comparison of time averages of 4-way cylinder probe and total pressure vs. pitot measurements at AFAPL.



Fig. 1.6 -- 4-way high frequency cylinder probe  
(the light spots are transducers).

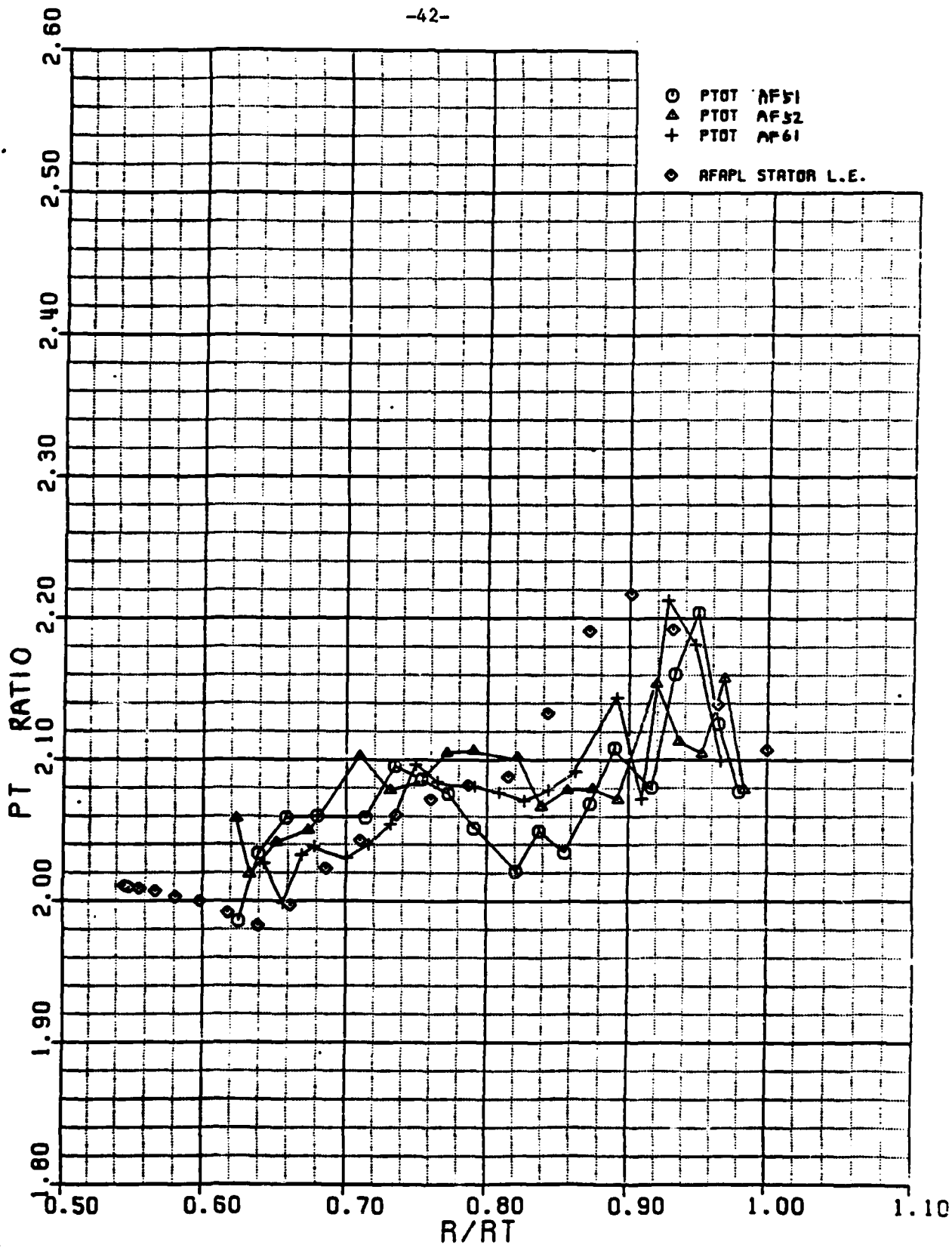


Fig. 1.7 -- Variation in radial distribution of stagnation pressure as measured by total pressure probe during three nominally identical tests.

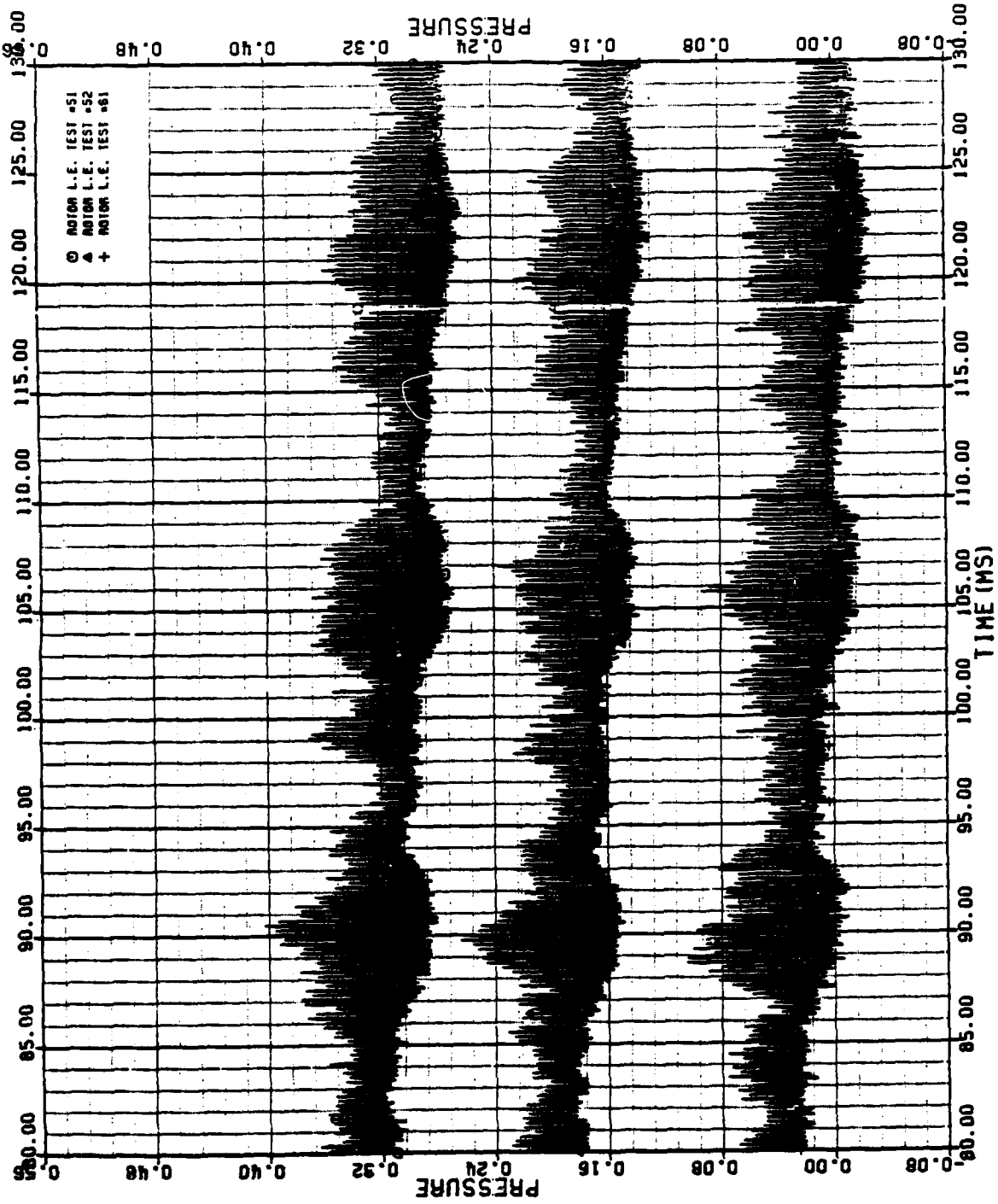


Fig. 1.8 -- Comparison of wall static pressure measured 0.2 chords upstream of rotor leading edge during 3 nominally identical runs. The curves have been displaced vertically for clarity.

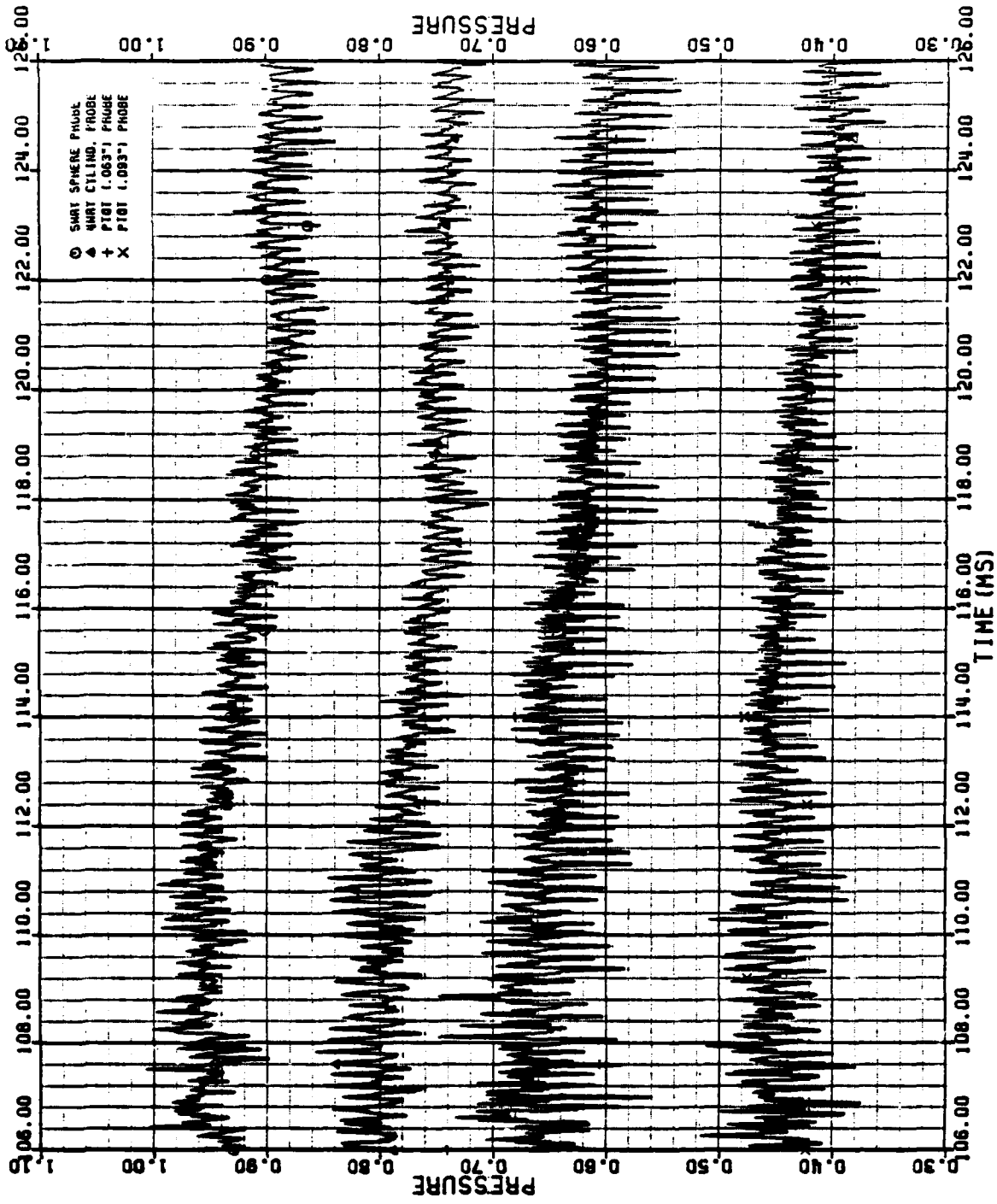


Fig. 1.9 -- Variation in measured total pressure for 4 different probes during a tip to hub traverse during 4 different tests. The traces are displaced vertically for clarity.

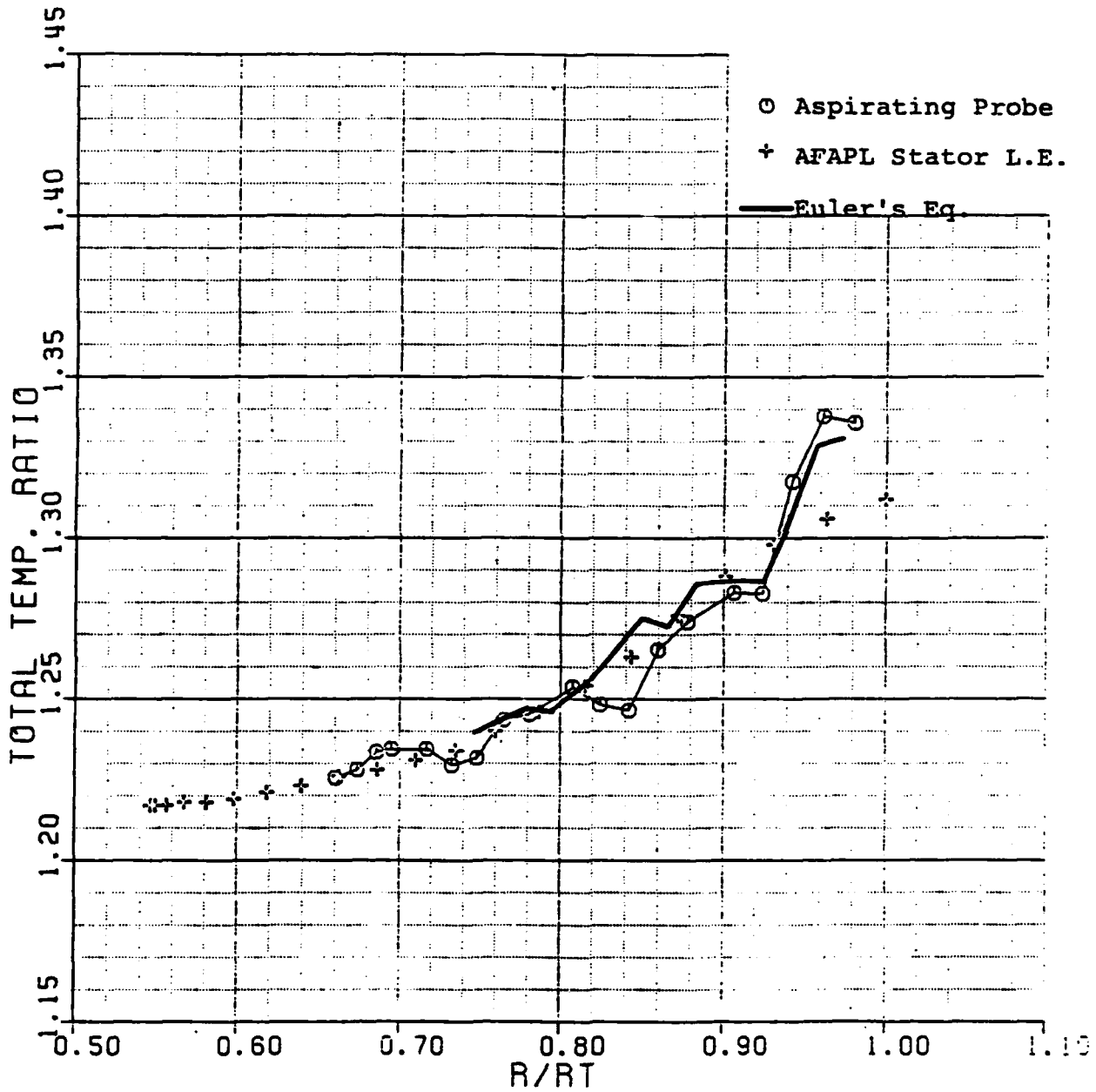


Fig. 1.10 -- A Comparison of time averaged total temperature measured with the aspirating probe, conventional thermographs at AFAPL, and deduced from angle measurements using Euler's Equation.

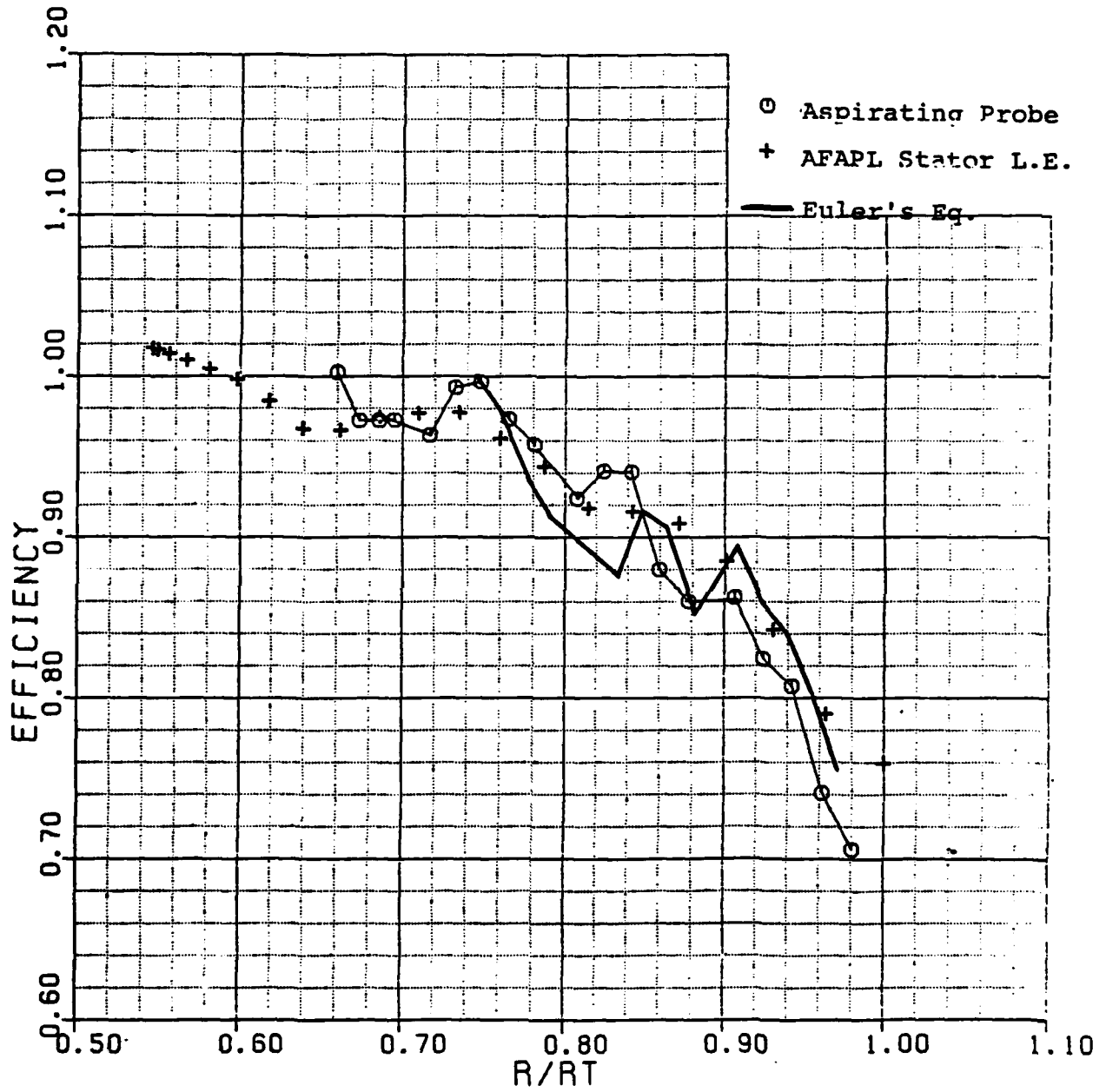


Fig. 1-11 — Adiabatic efficiency calculated from the data in Figures 1.5 and 1.10.

R/Rt = .95

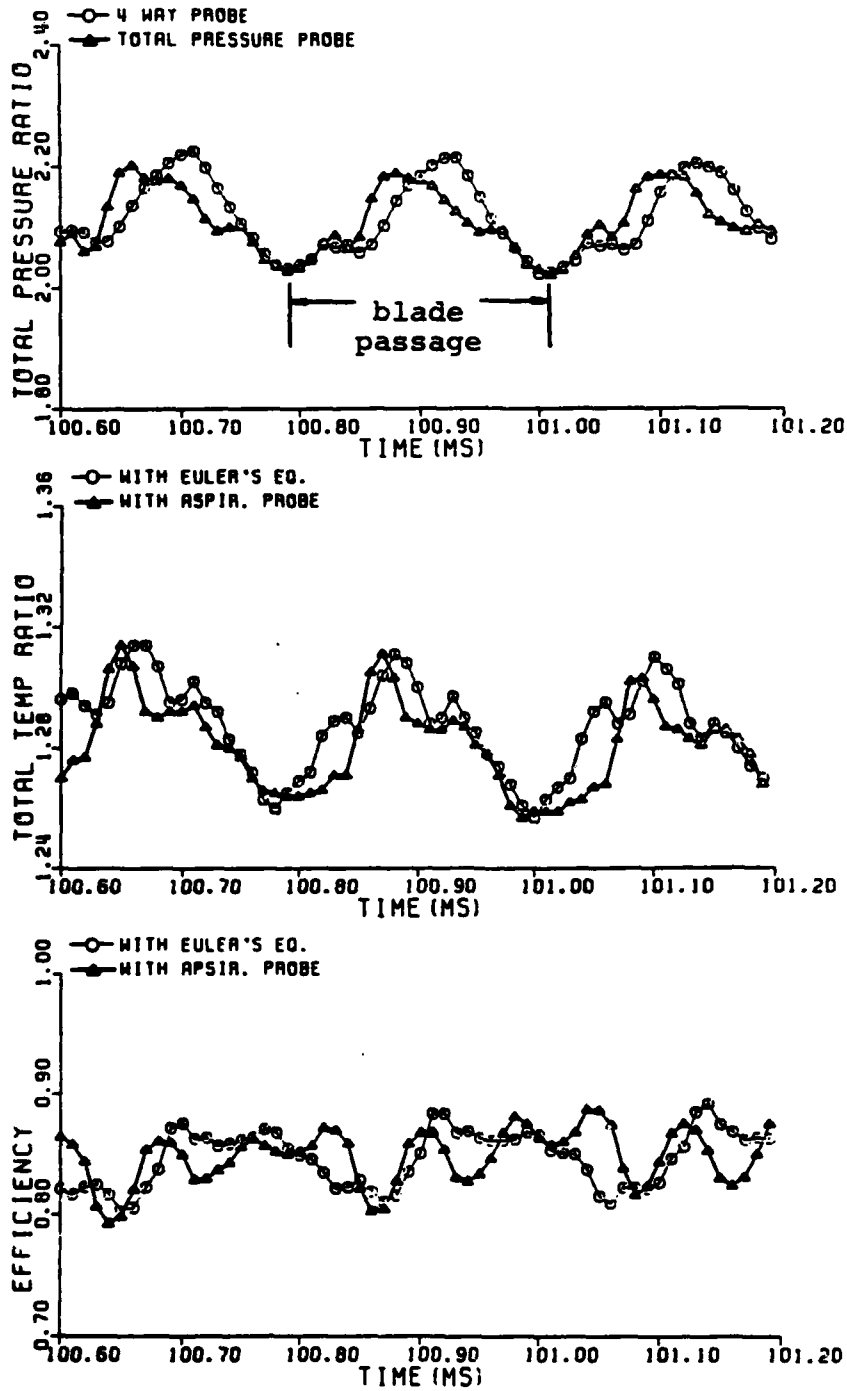


Fig. 1.12a -- Comparison of total pressure ratio, total temperature ratio and efficiency between 4 Way Probe and Aspirating Probe at R/Rt=.95; 10 cycle ensemble averaged.

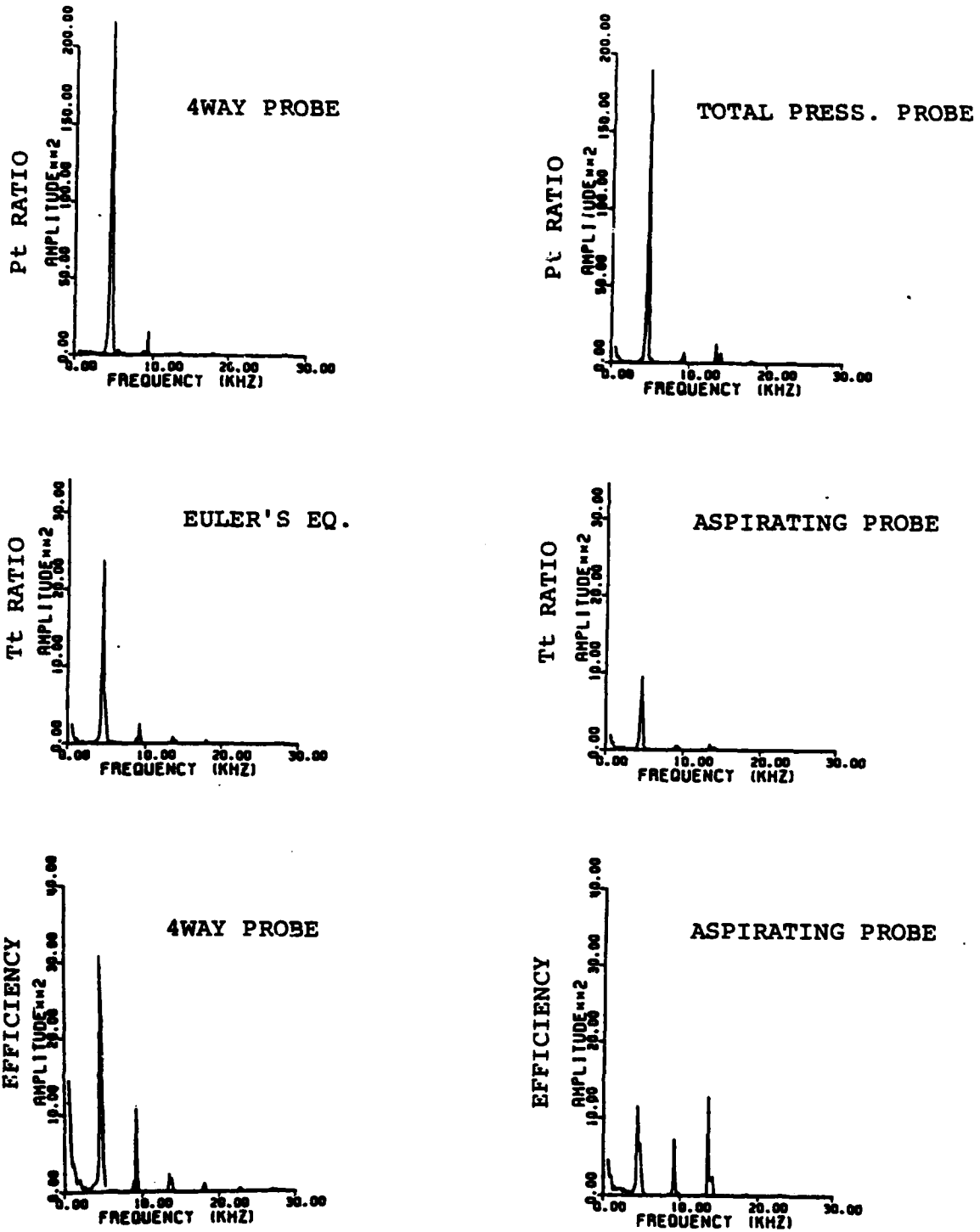


Fig. 1.12b -- Frequency spectrum of total pressure ratio, total temperature ratio and adiabatic efficiency from 4 way probe & aspirating probe at  $R/R_t = .95$ ; 10 cycle ensemble averaged.

R/Rt = .88

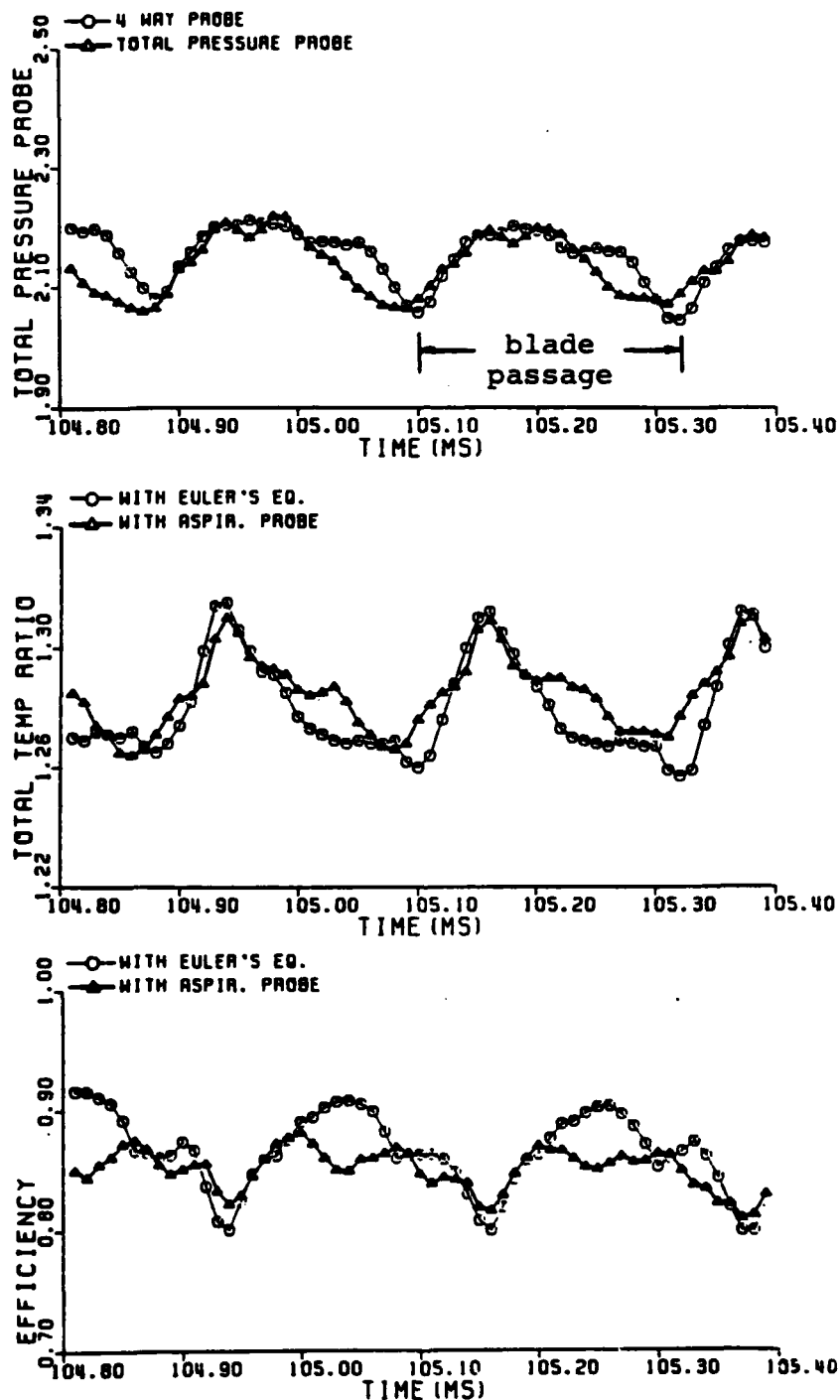


Fig. 1.13a — Comparison of total pressure ratio, total temperature ratio and efficiency between 4 Way Probe and Aspirating Probe at R/Rt=.88; 10 cycle ensemble averaged.

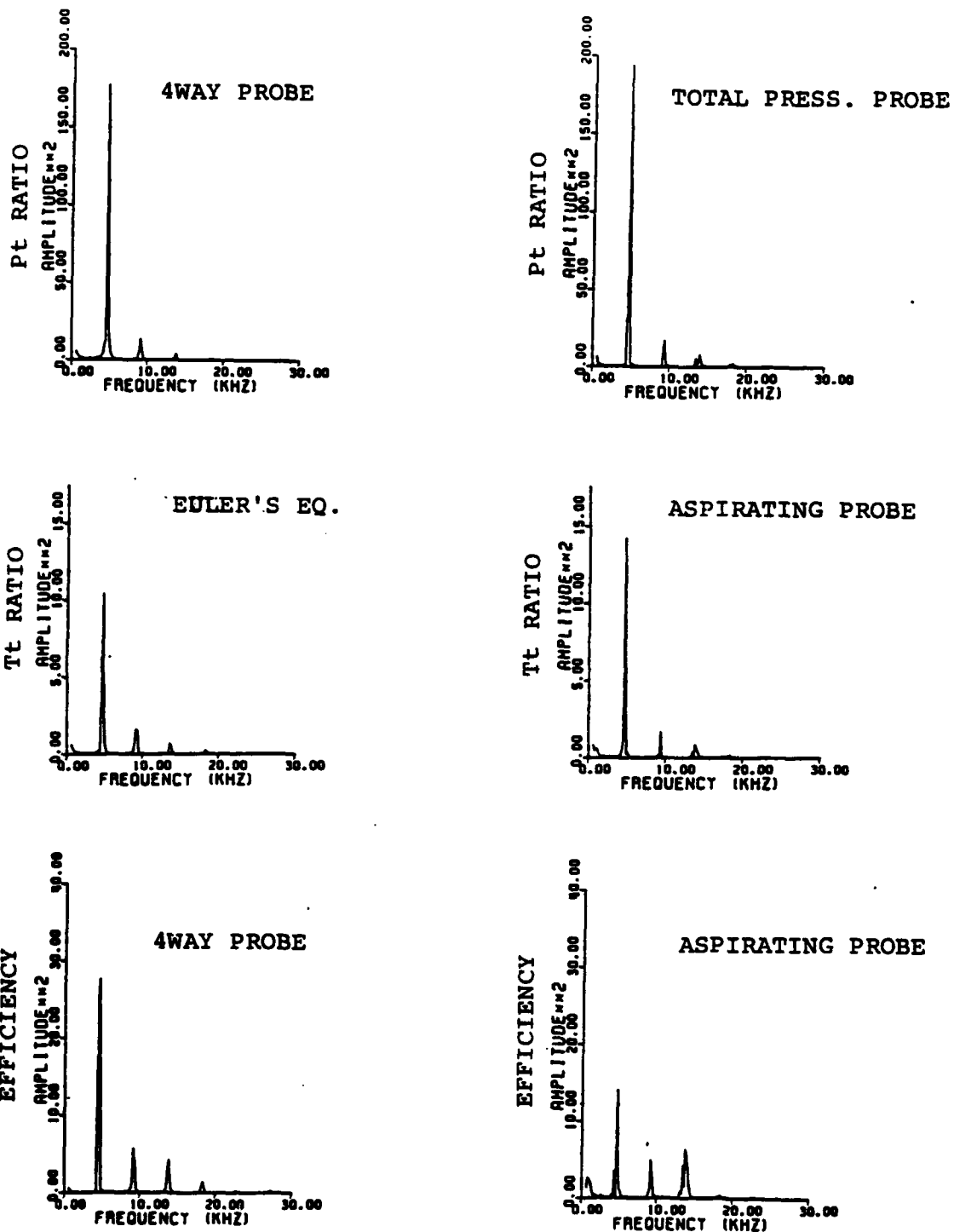


Fig. 1.13b -- Frequency spectrum of total pressure ratio, total temperature ratio and adiabatic efficiency from 4 way probe & aspirating probe at  $R/R_t = .88$ ; 10 cycle ensemble averaged.

R/Rt = .73

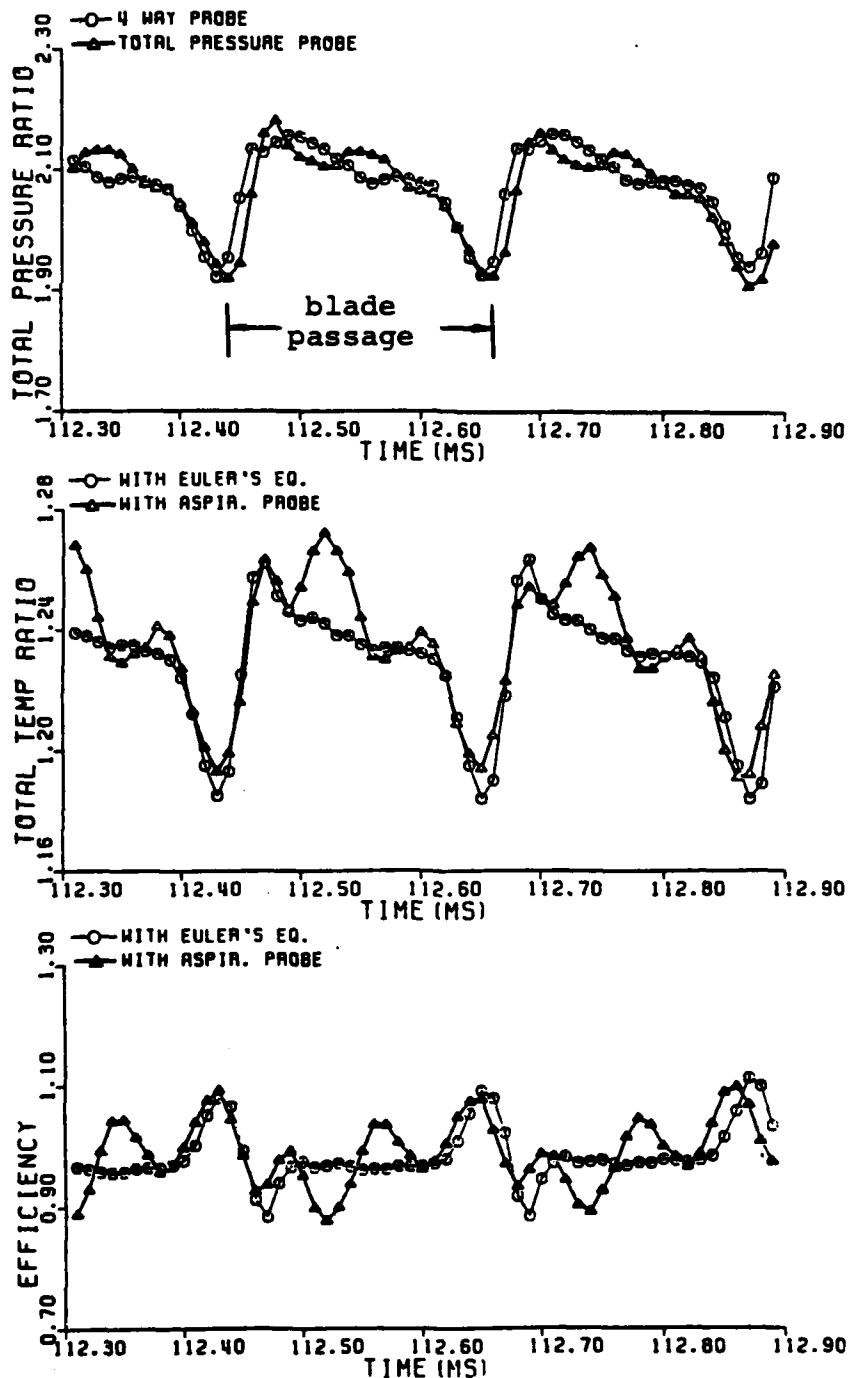


Fig. 1.14a -- Comparison of total pressure ratio, total temperature ratio and efficiency between 4 way Probe and Aspirating Probe at R/Rt=.73; 10 cycle ensemble averaged.

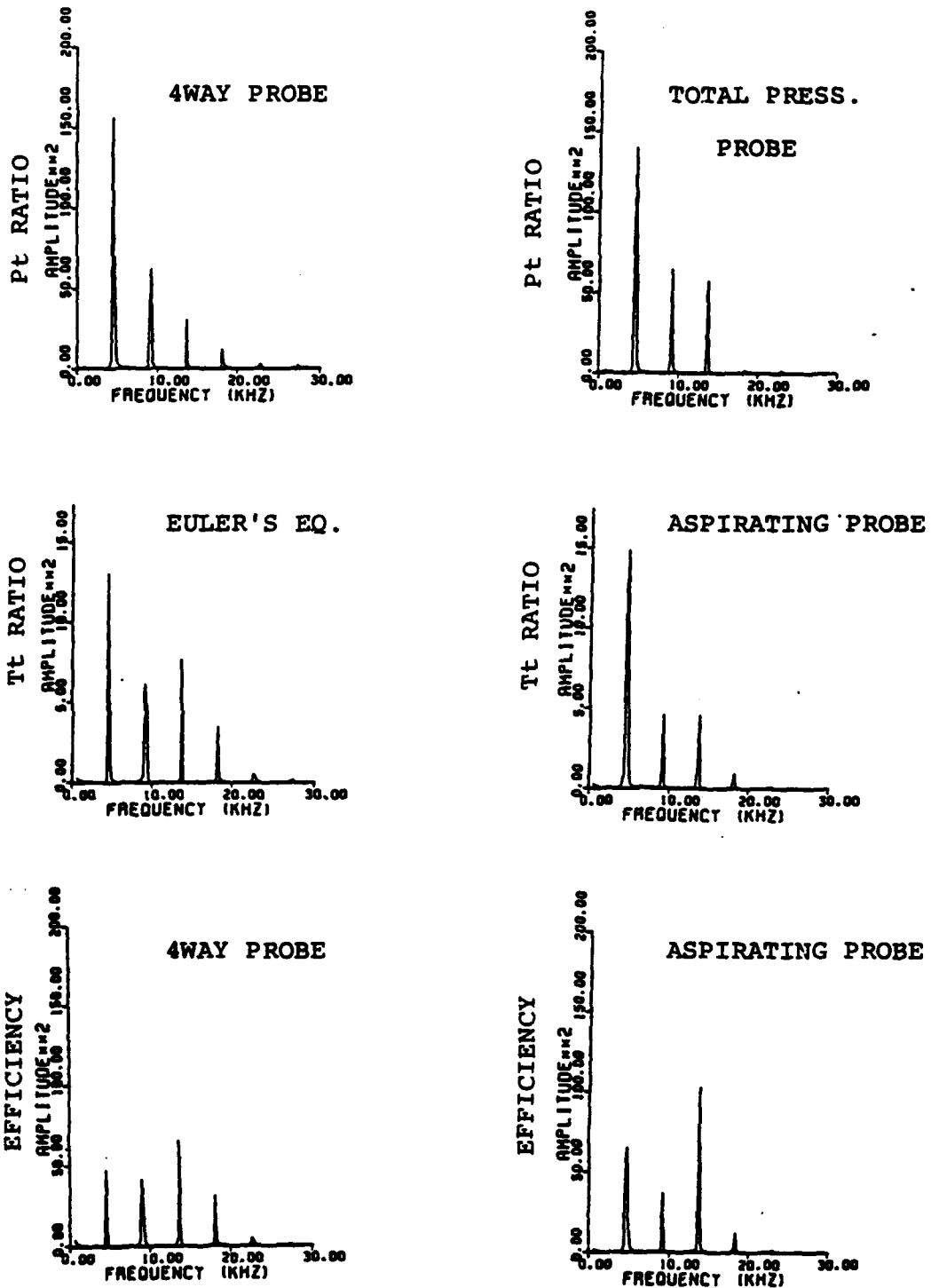


Fig. 1.14b -- Frequency spectrum of total pressure ratio, total temperature ratio and adiabatic efficiency from 4 way probe & aspirating probe at  $R/R_t = .73$ ; 10 cycle ensemble averaged.

TASK II: MECHANISMS OF COMPRESSOR STABILTY ENHANCEMENT  
USING CASING/HUB TREATMENT

During the past year we have tested the hub treatment using a high stagger stator configuration, in order to promote a wall stall. The result was a substantial improvement in stator stall margin and performance. This is the first time that such improvements have been documented.

We have also continued efforts on the modelling of the interaction between the flow in the grooves and that in the endwall (although the main emphasis has been on the experiments). The detailed results are given in the M.S. Thesis of Mr. P. Cheng. However, a paper has also been written which summarizes this work, and this is presented below.

EFFECTS OF COMPRESSOR HUB TREATMENT  
ON STATOR STALL AND PRESSURE RISE

P. Cheng, M.E. Prell, E.M. Greitzer, C.S. Tan  
Department of Aeronautics and Astronautics  
Massachusetts Institute of Technology  
Cambridge, MA 02139

ABSTRACT

An investigation has been conducted of the changes, in stator stall margin and performance, which occur due to a slotted hub treatment rotating beneath an axial compressor stator row. Two different stator rows, one with low stagger and one with high stagger, were tested both with solid wall and with hub treatment. The experiments showed, for the first time, that (with the high stagger blading) the hub treatment was very effective in delaying the outset of stator stall and in increasing the peak stator static pressure rise. For this blading, measurements of the stator exit flow field appear to indicate that the inception of stall was associated with a wall stall. With the treatment the large blockage in the hub region was greatly decreased and, near the hub, the total pressure at the stator exit was found to be higher than that at stator inlet. These results, in accompaniment with the data taken using the low stagger stator, support the hypothesis that endwall treatment is effective when the type of stall that occurs is wall stall.

### Introduction

It has been known for some years that the application of grooves or slots over the rotor tips in the casing of an axial flow compressor can have a large effect on compressor stall margin and performance. Experimental observations (1, 2) have also shown that casing treatment can substantially reduce the endwall boundary layer blockage in the rotor tip region. It has been hypothesized that this blockage reduction results from strong flow injection out of the treatment, and that the low-momentum flow in the endwall region is energized due to this injection of high velocity fluid.

It has also been found that one can often make a simple but useful distinction between two types of compressor stall. One of these, termed "blade stall" is a roughly two-dimensional type of stall where a significant portion of the blade span has a large wake due to substantial thickening or separation of the suction surface boundary layer. The other, termed "wall stall," is associated with the endwall boundary layer separation (1, 2), and it appears that casing treatment will only be effective when the type of stall is wall stall (1, 2).

A third feature which has emerged not only from (1, 2) but from flow visualization reported in (3), is that relative motion between endwall and blade is an important element for the success of the grooves in reducing the blockage. In view of this, it is natural to ask whether a rotating "hub treatment" below a row of cantilevered stator blades would also be effective in improving the stall margin. If this is so, the geometry would also be more amenable to investigation of the details of flow in the blade passage, as well as provide a different perspective from which to view the fluid dynamic phenomena.

In the present work, the effect of hub treatment on the stall margin and performance of a "hub critical" stator was examined. Two sets of blading configurations were tested, each with a solid wall and with hub treatment. It was found that for the first set of blading (low stagger) the application of hub treatment did not have a major effect on the stator performance. However, for the second set of blading (high stagger) the hub treatment improved the compressor performance, delaying the inception of stall and markedly increasing the peak stator static pressure rise.

#### Experiment Design

It is fundamental in the design of this experiment to ensure that the stator hub endwall is stall limiting. The design used is aimed at having the rotor (and IGV) act only as a "flow generator" for the stator. Thus, in choosing the blade setting angles, it is desired that the rotor has a low loading relative to the stator. The requirement of high stator hub loading can be satisfied by using a rotor blade with low twist. This creates a low total pressure rise across the rotor hub relative to the tip, which loads the stator hub.

When the initial experiments were carried out in the present facility, a severe restriction was that the stator discharge was to ambient pressure. Hence, as described in (4), we were forced to use blading of rather low stagger, which tends not to be conducive to wall stall. In accordance with this (as described in detail in (4)) the type of stall encountered in these initial experiments appeared to be blade stall, rather than pure wall stall.

During the second set of experiments, which were carried out with an exhaust fan, however, we had the freedom to increase the blade

stagger; this tended to promote a wall stall. In addition, in order to achieve a wall stall, based on the correlation presented in (5), the stator hub clearance was doubled to four percent of the blade chord (or 4.5 percent of the staggered gap based on exit angle.) A summary of the two stator configurations used is presented in Table 1. In order to distinguish these two, we will refer to them below as the low stagger and high stagger stators respectively.

TABLE 1

STATOR BLADING GEOMETRY

	Low Stagger	High Stagger
Midspan stagger angle (measured from axial)	22.5°	42.5°
Camber	30.0°	30.0°
Solidity at midspan	1.0	1.0
Blade clearance	0.8mm	1.5mm
Number of blades	45	45
Chord	38.0mm	38.0mm

EXPERIMENTAL FACILITY

The experiment was conducted on a single stage research compressor driven by a variable speed D.C. motor. This is a 0.59m diameter single stage compressor with a hub/tip ratio of 0.75. It was modified for casing treatment as well as hub treatment, and the former was used throughout all the tests, as this tended to increase the hub loading. A cross sectional schematic of the compressor showing the blading and treatment locations is given in Figure 1.

Most of the measurements were taken at a blade speed of 75m/s (at the mean radius) for the low stagger stator and at 70m/s for the high stagger stator. Runs were also made at speed from 55m/s to 95m/s to check Reynolds number dependence (which was found to be of only slight influence on the observed changes due to the hub treatment). The

Reynolds number based on blade chord at the stator midspan (at the stall point) was nominally  $1.5 \times 10^5$  for the first set of tests and  $1.0 \times 10^5$  for the second.

The pressure instrumentation consisted of 20 total pressure "Kiel" probes and 24 hub and casing static pressure taps. Acquisition of the pressure data was done by a 48 channel scanivalve pressure scanner operated by a digital microcomputer. A self-nulling radial traverse mechanism was used to determine radial profiles of total pressure and flow angle and a hot wire anemometer was used to enable accurate determination of the stall point.

The data to be presented is non-dimensionalized in a standard fashion: velocities are non-dimensionalized by  $U$ , the mean blade speed, and pressure difference are non-dimensionalized by either  $1/2\rho U^2$  or by the relevant stator inlet dynamic pressure. Other quantities used for non-dimensionalization or for reference levels will be defined as they are introduced. In all the figures "SW" is used to denote the solid wall and "HT" is used for hub treatment. Further details of the facility are given in (4) and (6).

#### TREATMENT DESIGN

The hub treatment consists of axial slots skewed at a  $60^\circ$  angle to the radial direction. These slots have been found to provide large increases in stall margin when used as a rotor casing treatment. The slots rotate under the middle 90% of the stator for the high stagger rotor and under the middle 70% for the low stagger. The slot spacing is such that the slotted area is twice that of the solid (land) area.

The slot aspect ratio (axial length/tangential width) is 2.0, and the radial depth is 30% of the axial length. The actual dimensions and treatment geometry are shown in Figure 2. The hub treatment was constructed by machining a wide circumferential groove in the cylinder and glueing pre-machined plexiglass plates into the groove.

### EXPERIMENTAL RESULTS

In this section we first show the effects of the hub treatment on stall margin and compressor speedline characteristics, then compare the untreated and treated traverse data and discuss these results.

#### Low stagger stator

For the low stagger blading, the application of hub treatment to the compressor described above resulted in only a small reduction of the stalling flow coefficient<sup>1</sup> (approximately 2%) and an increase in the stator pressure rise characteristic of approximately 5% at the peak. The stator pressure rise characteristic from this test, as determined from the casing wall static taps just ahead of and just behind the stator, is shown in Figure 3. The vertical axis is nondimensionalized wall static pressure rise across the stator and the horizontal axis is the axial velocity parameter ( $C_x/U$ ) based on mean inlet axial velocity. The stall points, i.e., the points of inception of rotation stall in the stator are also indicated. (For reference the rotor stall point was far below these at  $C_c/U = 0.35$ .) Rotating stall

---

<sup>1</sup>The point at which rotating stall was encountered.

onset was clearly detectable on an oscilloscope which displayed the response of hot wire survey at stator exit 20% span away from hub through an anemometer.

Although there is an increased static pressure rise across the stator, due to the hub treatment, at all flow coefficients tested, the increase is much less than the large increases that have been experienced with casing treatment. One additional aspect described in (4) is that there was a decrease of stator deviation angle and blockage with treatment compared to the untreated case, and presumably this improvement is the reason for the increase in treated stator static pressure rise. However, from the analysis of stator wakes, it was seen that a thick wake was present from hub to midspan both with treatment and without. This data, as well as other supporting evidence given in (4), implied that the inception of stall was associated with a so-called "blade stall" type of separation.

#### High stagger stator

For the high stagger blading the application of hub treatment of the compressor resulted in a much more substantial change. The flow coefficient at stall onset was decreased by 12% and, more impressively, the peak stator static pressure rise was increased by over 50%. Figure 4 shows a comparison of the overall total to static pressure rise characteristic  $[(P_{ex} - P_{t_{in}})/(\rho U^2/2)]$  vs.  $(C_x/U)$  for the complete stage, with and without the hub treatment. The stator stall points, also indicated here, are at  $C_x/U = .315$  and  $.275$  (for the solid wall and hub treatment respectively), with an uncer-

tainty of approximately one percent. Note that although the  $C_x/U$  values are somewhat lower than normal, it should be emphasized that this is due to the high rotor stagger, and the stagger and flow angles associated with the stator are representative of those encountered in modern compressors. Due to the large pressure rise in the rotor, the improvement in stator performance is not really brought out in this figure. However, the figure does show that the overall stage characteristic is negative and that the rotor is operating far from stall, as should be the case in this experiment.

A comparison of the stator static pressure rise characteristic is shown in Figure 5, which shows  $\Delta P_{\text{stator}}/(\rho U^2/2)$  plotted versus  $C_x/U$  for the solid wall (SW) and the hub treatment (HT). It is evident that the inception of stall has been delayed and the static pressure rise has been markedly increased due to the hub treatment.

These stator speed lines were checked several times with and without treatment. It was found that there was some slight deterioration in performance over long test times (due presumably to the accumulation of dirt, which could be seen to build up on the compressor blades). However, the maximum difference found due to this effect was a flow coefficient shift, with both solid wall and hub treatment, of 2% or less, i.e., the changes were an order of magnitude less than the differences between the solid wall and hub treatment configurations.

Radial Traverse Total Pressure Data

In order to examine the feature of the flow in more detail, radial traverses were taken with the solid wall and with hub treatment at a "solid wall near stall point",  $C_x/U = 0.33$ . A comparison of the (arithmetic) pitch average total pressure distribution at the rotor and stator exit for hub treatment and solid wall at this near stall point is presented in Figure 6. The symbols RTE and STE refer to the locations downstream of the rotor and stator respectively, as shown in Figure 1, and again, SW denotes solid wall and HT denotes hub treatment. In the figure the vertical axis is radial location (percent span) and the horizontal axis is the non-dimensionalized total pressure. The reference pressure is ambient (compressor inlet total pressure) and the dynamic pressure used for non-dimensionalization is based on the midspan stator inlet velocity. The reason for this latter convention is that due to the very non-uniform total pressure profile, there is no one "freestream" value of the stator inlet dynamic pressure; however, the midspan quantity is a convenient representative value.

In examining the stator exit traverses it should be mentioned that there was an axial gap of 3mm behind the stator (see Figure 1) between the rotating hub piece and the stationary annulus, with a dead-ended cavity below. Although this may affect the absolute values of total pressure and flow in the hub, it is to be emphasized that it is the comparisons between solid wall and hub treatment that are of most interest here, and the gap geometry is the same for both these

cases. The comparisons should thus be valid, especially since the differences are quite substantial.

It can be seen that the rotor exit total pressure profiles are nearly identical so that for both smooth wall (SW) and hub treatment (HT) the (stator) inlet conditions are the same. However, the two stator exit profiles are quite different. With the solid wall there is a large total pressure defect (and also a large blockage) near the stator hub. In contrast, for the treated case the stator exit total pressure is higher than the rotor exit total pressure near the hub. It is evident that work has been done on the flow in the endwall region due to the fluid injected from the grooves and that the heavy losses (and blockages) in the hub region, have been reduced. (Note that for this set of experiments the flow is essentially incompressible so there is no net flow out of the treatment. However, due to the fact that the flow entering and leaving the grooves has a very different velocity, there can be a net momentum flux out of the grooves.)

Another feature seen in Figure 6 is that even at midspan the treated stator exit total pressure with hub treatment is apparently higher than that which occurs with the solid wall. However, one would not expect the mixing effects (i.e. shear forces) to extend to this radial station from the endwall region. In fact the reason for this total pressure change is that there is a large blockage at the hub region with the solid wall, and the flow near the hub is forced to move outwards. In consequence, there is a considerable radial streamline shift that occurs between the RTE to STE axial locations

for this configuration. This radial shift (convection) of the non-uniform total pressure profile causes the apparent total pressure change in the midspan region, as will be discussed below.

#### Flow Angle

Figure 7 presents comparison of the absolute flow angle  $\alpha$ , measured from the axial direction. The figure shows the midpitch radial distribution of angles with smooth wall and with hub treatment at  $C_x/U = 0.33$ . It is seen that again the two rotor exit profiles are very similar, the difference between the two being within  $0.5^\circ$  at all radii. In contrast, the two stator exit profiles are quite different. With the treatment there is an increase in angle very near the hub but a decrease in angle, i.e., an increase in turning, in the midspan region due to the treatment; similar results were obtained in the low stagger case.

#### Circumferential Traverses

Another way to examine the effect of treatment on the flow field is to compare the circumferential distribution of total pressure at the STE station for the solid wall and the hub treatment. This comparison is made in Figure 8, which shows plots of total pressure difference across the stator blade row divided by local inlet dynamic head, versus circumferential position, for several different span locations. The total pressure used for reference in this figure is the rotor exit total pressure, which has been converted to the appropriate stator exit radial position using a streamline curvature

data reduction program (7). The dynamic pressure used for nondimensionalization is based upon the local stator inlet velocity.

Although the reference pressures at inlet are slightly different due to the (radial) streamline shifts, it can be seen that there are major differences between these two cases at the region 6% span away from hub. For the solid wall the wake is very deep with large loss. With hub treatment the wake profile is flatter and, more importantly, the total pressure is higher than the rotor inlet total pressure at all circumferential positions.

Further evidence of the differences between solid wall and hub treatment is seen in the comparison of the wake distribution at the 26% span location. With the solid wall the wakes are fairly thin; this is viewed as another indication that the onset of stall is due to a pure wall stall at the hub. With the hub treatment, however, there is a "spike" in total pressure between near the pressure surface side. We take this to imply that this is an indication of a jet of high total pressure fluid. This is consistent with a picture of strong flow injection out of the slots impinging on the pressure surface, and deflection rearwards. At the midspan region and outboard the wake distributions are similar for the solid wall and the treatment, although the magnitudes are slightly different.

The effect of hub treatment on the total pressure "loss" profile (based on the axisymmetric data analysis program) is shown in Figure 9, which is also at  $C_x/U = 0.33$ . The loss coefficient,  $\bar{w}$ , is here defined as the (pitch averaged) total pressure difference across blade divided by the local inlet dynamic head. For the solid wall the

loss profile is in accord with what one would expect, with low losses near the midspan region, and higher values at the two endwall regions. With treatment, however, the total pressure "loss" coefficient (as defined) becomes negative from midspan to hub endwall, showing clearly that the hub is doing work on the flow.

We have previously discussed the differences in radial streamline shifts for the two configurations. The radial streamline shifts derived from the data reduction program are presented in Figure 10. In the figure the streamline shift between the RTE and STE axial locations, divided by span, is plotted as a function of radius. For the untreated case there is a large streamline shift due to the blockage occurring near the hub, while for the treated case the shift is smaller because of the reduced blockage.

Using this information about the radial flows, we can now close the loop and present a rotor exit total pressure profile which has been convected according to the radial streamline shift shown in preceding figure. (Note that this shifted total pressure, denoted by RSH was the reference pressure for the total pressure plots presented in Figure 6.) Figure 11 shows this shifted rotor total pressure profile and the measured midpitch stator total pressure profile, for the treated hub configuration, at  $C_x/U = 0.33$ . The reference pressure used here is the ambient pressure, and the dynamic head for nondimensionalization is based on the midspan stator inlet velocity. It is seen that in the neighborhood of the midspan the two profiles are closely the same; this shows the consistency between the data analysis and the experimental results since at midpitch the flow can

be considered inviscid and the total pressure should be constant along a streamline. Note, however, that near the hub the stator total pressure is higher than the shifted rotor total pressure; as described previously this is viewed as being due to the net momentum flux out of the treatment, which is seen as a key characteristic of hub treatment.

In addition to the data presented previously, other data of a diagnostic nature were also taken to investigate the sensitivity of the results to the Reynolds number. Over the range tested ( $.75 \times 10^5$  to  $1.35 \times 10^5$ ) there was little change (less than three percent maximum) in any of the measured performance parameters. Since the difference between treated and untreated builds at any of the Reynolds numbers tested was an order of magnitude larger than this, Reynolds number effects on the overall phenomenon are small.

#### Discussion

From the experimental results it appears that there is a strong similarity between hub treatment and casing treatment; flow injection out of the slots and consequent energizing of the endwall region and reduction being a key element of the operation of both. Accompanied with the casing treatment results, it is also believed that the hypothesis of "blade stall" and "wall stall" can be a useful criterion for successful treatment application. From a more detailed fluid dynamic point of view, however the basic mechanism for the operation of endwall treatment is still not really understood in a quantitative manner. In this regard, the terms wall stall and blade stall are not really descriptive in any sort of fundamental fluid mechanic sense.

It is thus important to quantify more precisely the features of the flow regimes that are associated with each type of stall, as well as the detailed effects of casing treatment on the stall onset process. The present set of experiments can therefore be viewed more as an overall examination of the problem and it is clear that questions such as those posed in (1) will require information on a more detailed level.

There is one further point that can be mentioned. As previously discussed, it is hypothesized that the delay in stall outset due to endwall treatment is associated with momentum transfer between slots and blade passage. This momentum transfer is viewed as reducing the endwall boundary layer blockage. We have explored this using a simple endwall boundary layer flow model to examine the effect of casing/hub treatment on boundary layer growth (6). It is found that the momentum transfer at endwall due to flow in and out of the grooves has a much more powerful effect on the boundary layer growth than the wall shear stress has. The results indicate that the endwall treatment does have a very strong potential to decrease the boundary layer growth, although the calculated effects are larger than those observed in the limited data available.

Summary and Conclusions

1. An investigation has been carried out on the effects of a rotating grooved hub treatment on stator stall and performance. Two different sets of stators, a low stagger and a high stagger row, were tested with and without the axial skewed groove hub treatment.

2. It was found that for the low stagger row the application of hub treatment did not have a major effect on the stator performance. It also appeared that the type of stall encountered with this configuration was blade stall.

3. For the high stagger row the application of axial skewed slots to the rotating hub under a compressor stator resulted in a substantial change in both the stall onset point and peak static pressure rise of the stator. To the authors' knowledge this is the first time such results have been obtained.

4. It is hypothesized that the success of the treatment was due to the suppression of wall stall at the hub, this being supported by hot wire surveys and circumferential traverses at stator exit. Accompanied with the results of the low stagger case, this seems to illustrate again that endwall treatment will be effective when the type of stall that occurs is wall stall.

5. It is seen that the large blockage at hub endwall region is removed when the treatment is applied. The high losses associated with to the blockage are not only decreased, but the total pressure

actually increases across the stator near the hub region, because of the work done by the (treated) hub on the main flow.

REFERENCES

1. Smith, G.D.J. and Cumpsty, N.A., "Flow Phenomena in Compressor Casing Treatment", Cambridge University Engineering Department Report, CUED/A-Turbo TR-112, 1982.
2. Greitzer, E.M., Nikkanen, J.P., Haddad, D.E., Mazzawy, R.S., and Joslyn, H.D., "A Fundamental Criterion for the Allocation of Rotor Casing Treatment," ASME Journal of Fluids Engineering, 101, June 1979.
3. Mikolajczak, A.A., and Pfeffer, A.M., "Methods to Increase Engine Stability and Tolerance to Distortion," AGARD-LS-72, Nov. 1974.
4. Prell, M.E., "An Experimental Investigation of Stator Hub Treatment in an Axial Flow Compressor," MIT, GTLPDL Report No. 161, July 1981.
5. Koch, C.C., "Stalling Pressure Rise Capability of Axial Flow Compressor Stages," ASME Paper No. 81-GT-3, May 1981.
6. Cheng, P., "Effects of Compressor Hub Treatment on Stator Stall and Pressure Rise," MIT, GTLPDL Report No. 167, September 1982.

7. Hearsey, R.M., "A Revised Computer Program for Axial Compressor Design," 1 & 2, ARL-TR-75-001, Aerospace Research Laboratory, Wright-Patterson Air Force Base, Ohio, 1976.
  
8. Horlock, J.H. and Perkins, H.J., "Annulus Wall Boundary Layers in Turbomachines," AGARD-AG-185.
  
9. Marble, F.E., Personal Communication, January 1982.

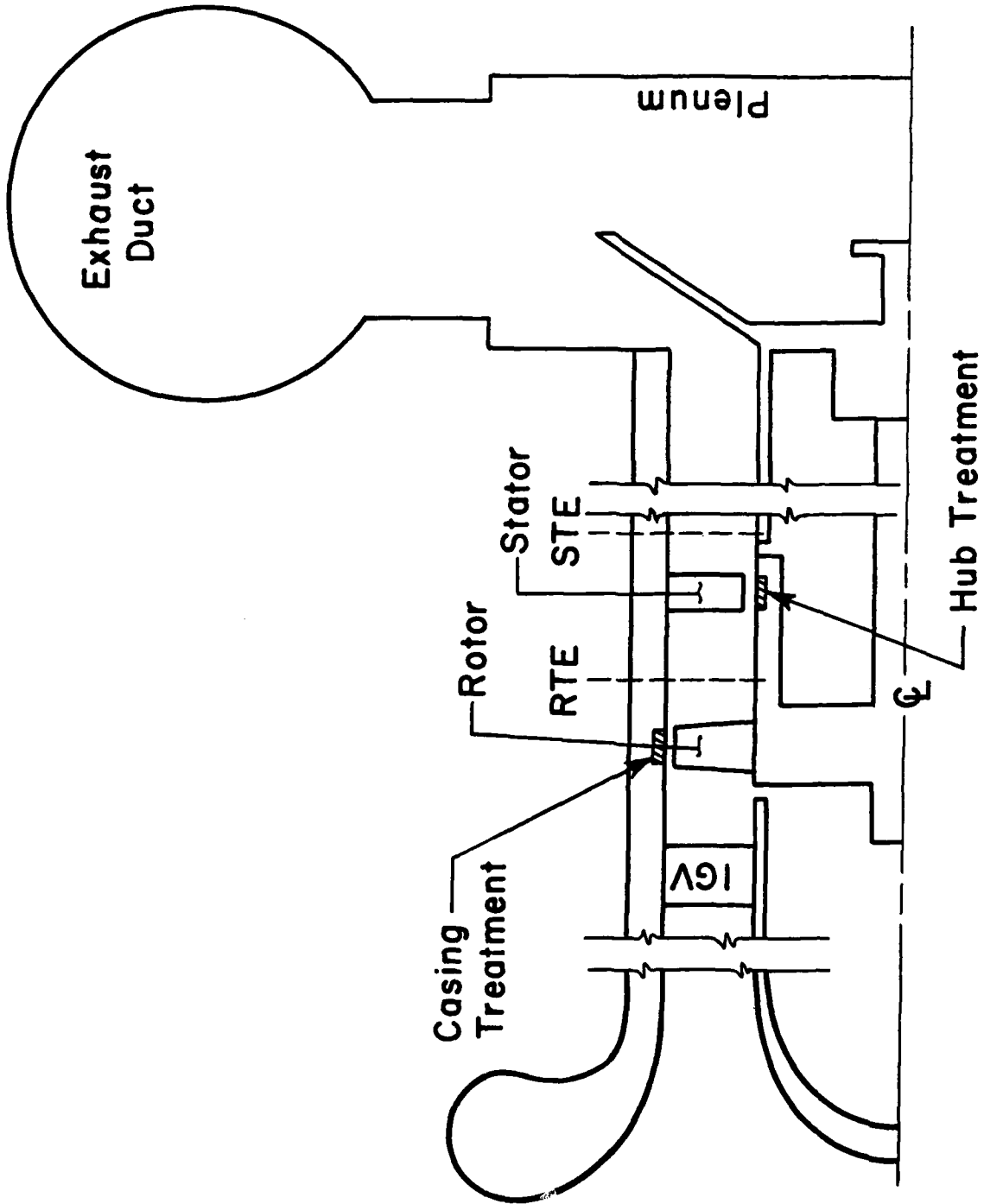
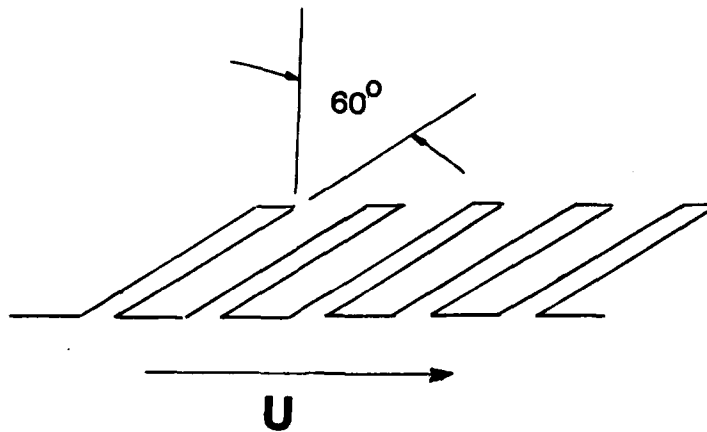
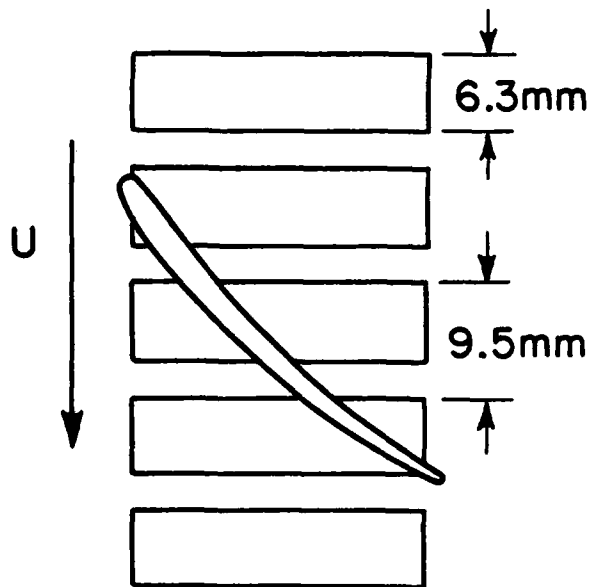


Figure 1. Compressor Cross Section (Schematic)

### R- $\theta$ PLANE



### X- $\theta$ PLANE



### X-R PLANE

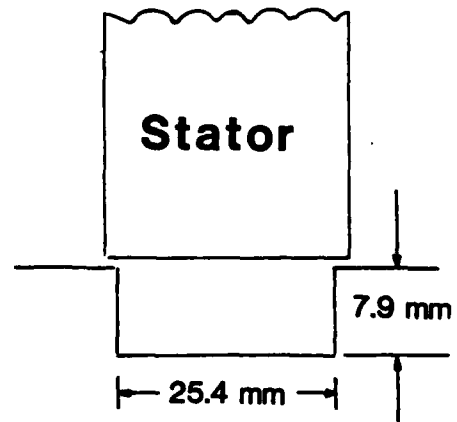


Figure 2. Hub Treatment Geometry (high stagger stator).

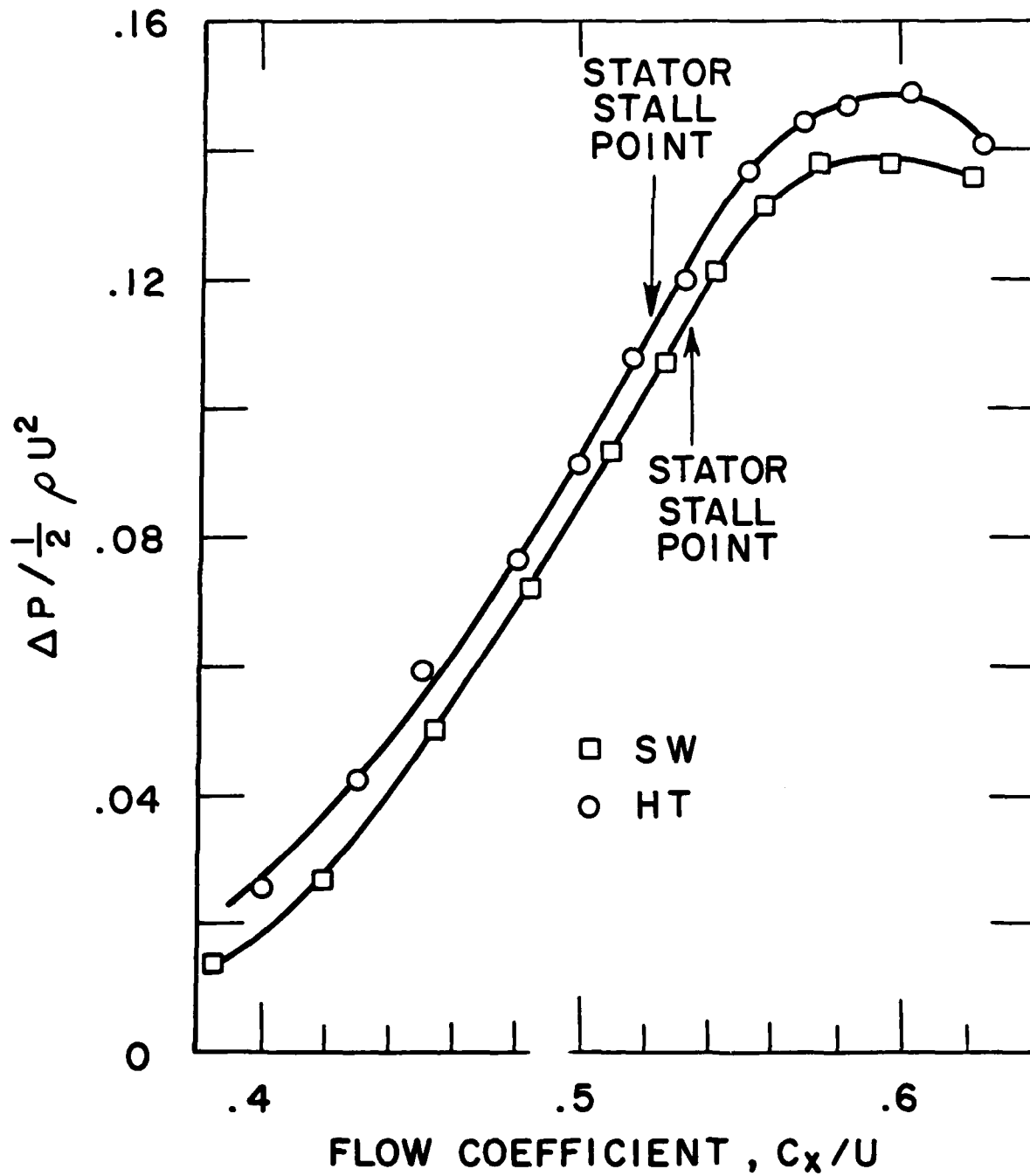


Figure 3. Stator Static Pressure Rise Characteristic (low stagger stators).

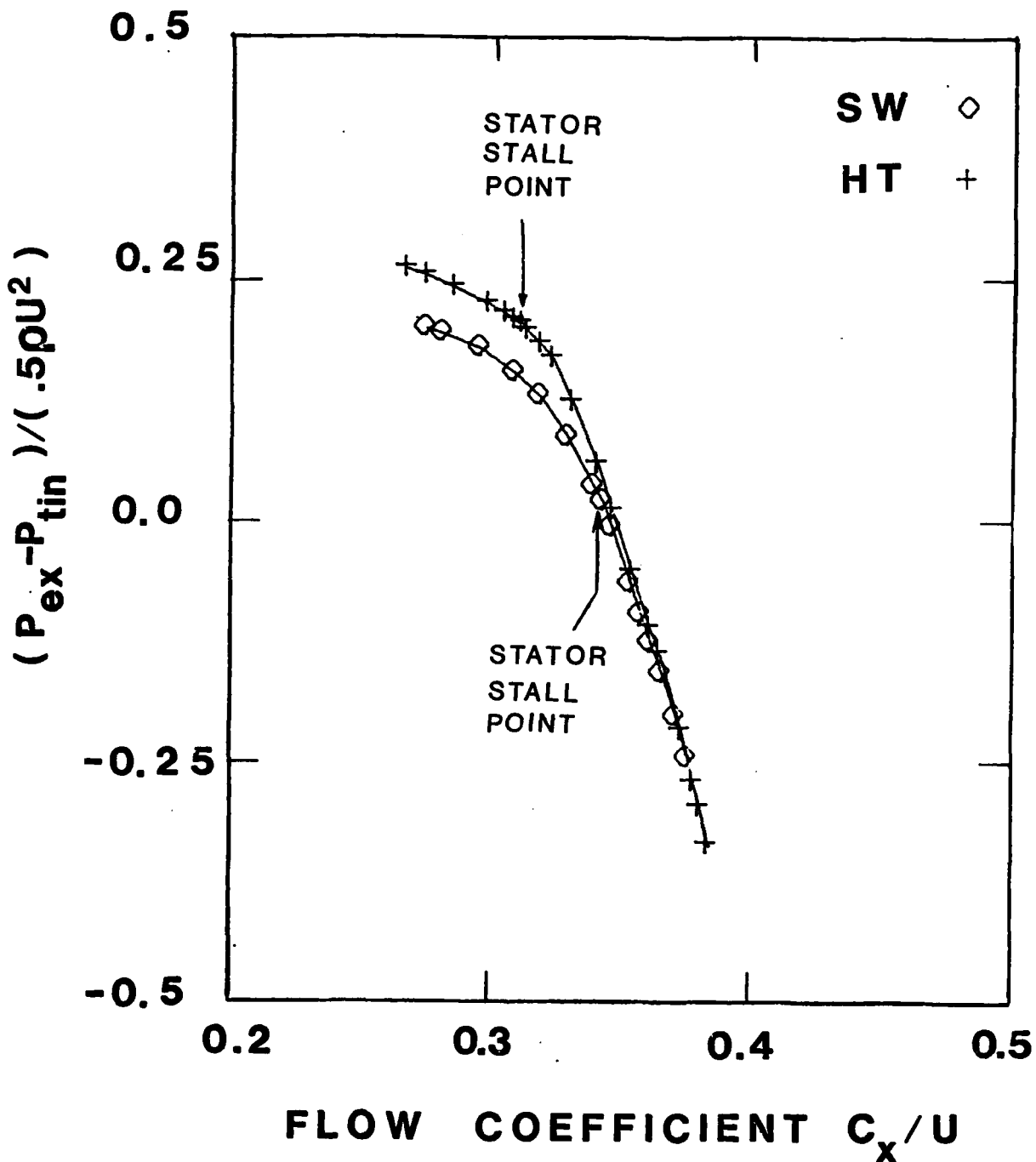


Fig. 4 -- Overall Stage Characteristic (High Stagger Stators) with Solid Wall (SW) and with Hub Treatment (HT)

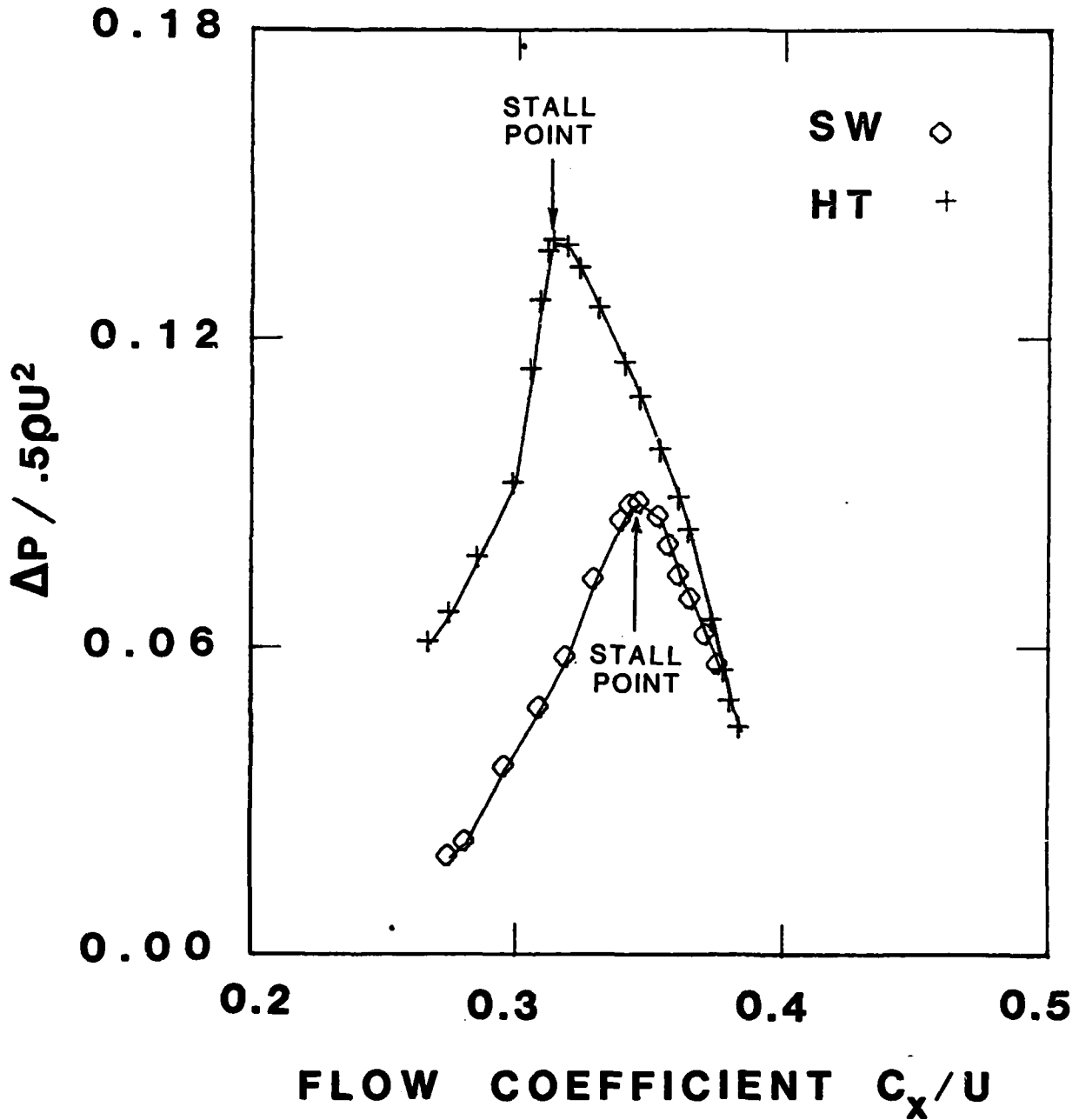


Fig. 5 -- Stator Static Pressure Rise Characteristic (High Stagger Stators) with Solid Wall (SW) and with Hub Treatment (HT)

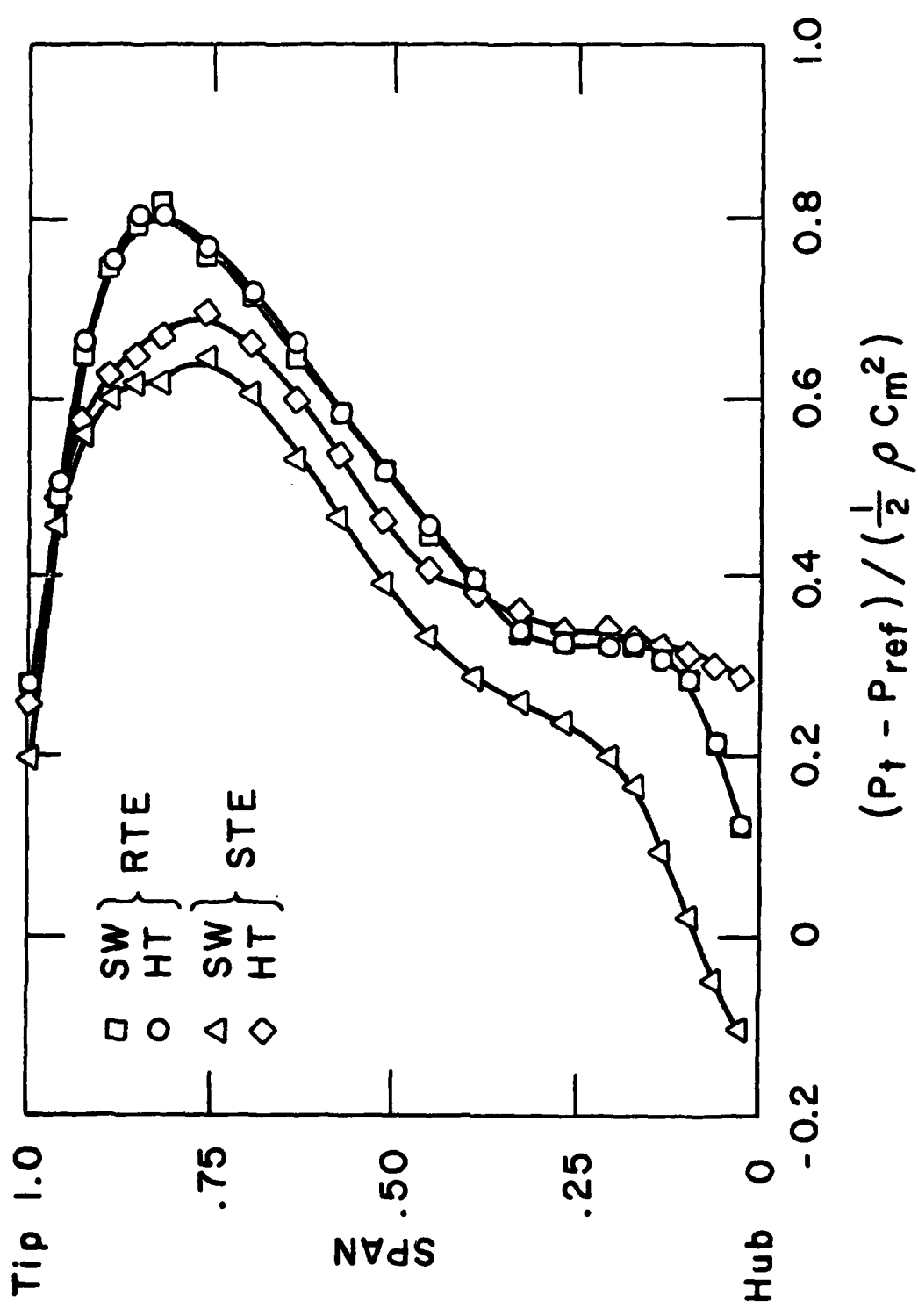


Figure 6. Stator Inlet and Exit Total Pressure Distributions with Solid Wall (SW) and Hub Treatment (HT)

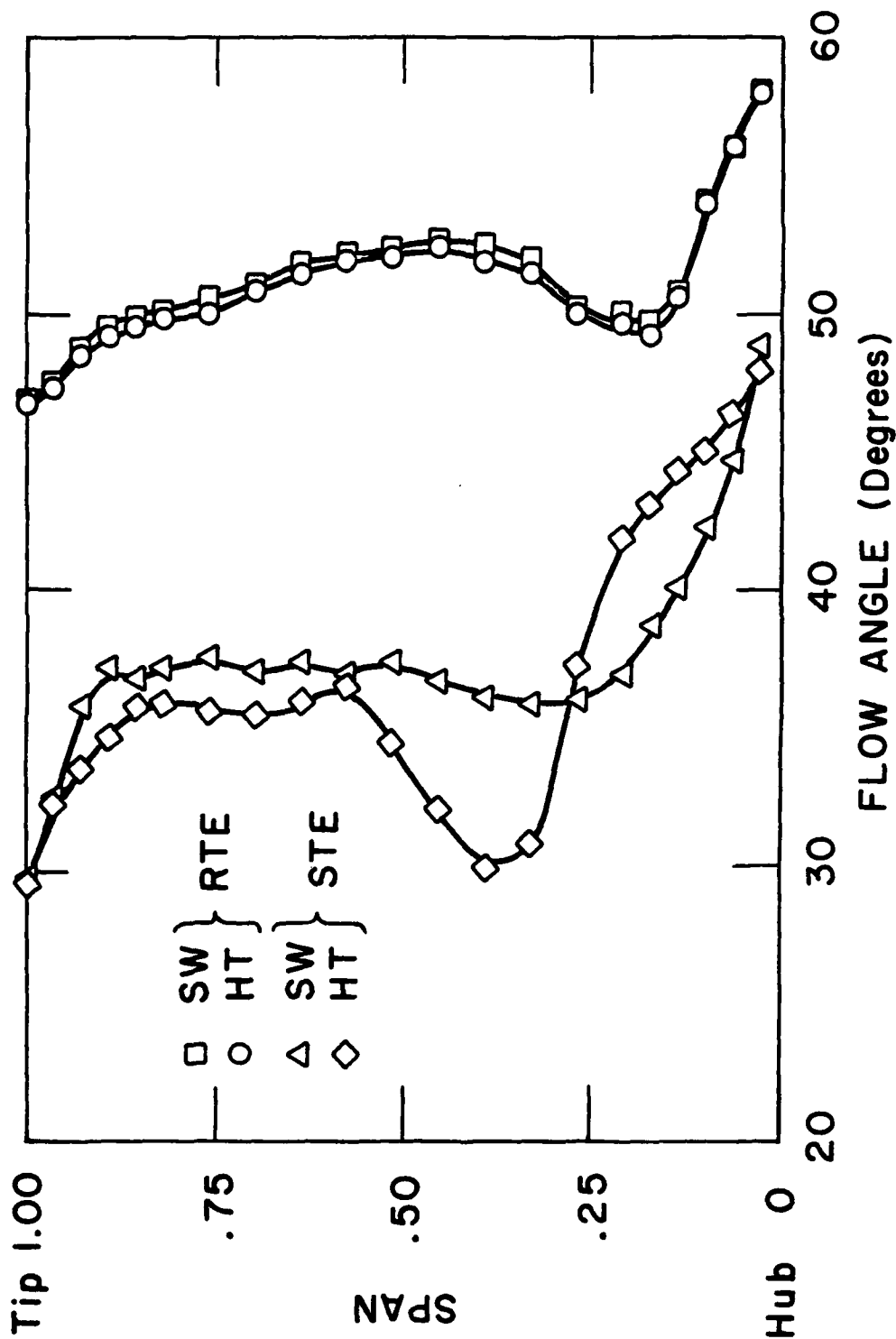


Figure 7. Stator Inlet and Exit. Flow Angle Distributions with Solid Wall (SW) and Hub Treatment (HT)



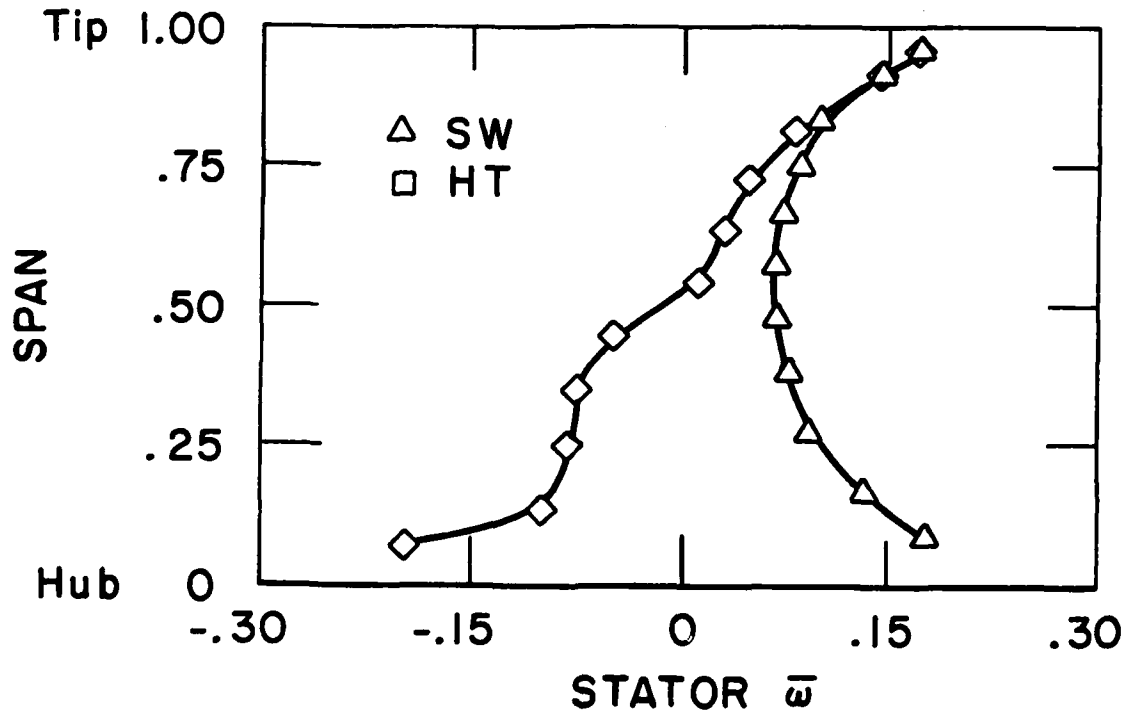


Figure 9. Stator Total Pressure Loss ( $\bar{\omega}$ )

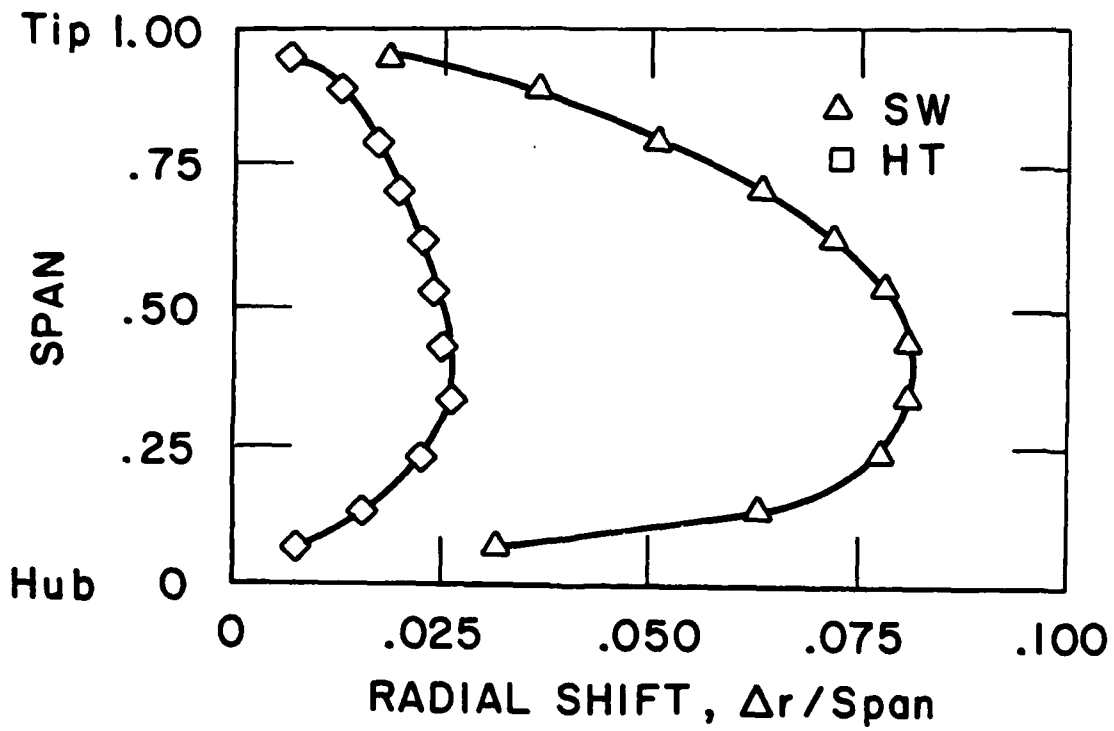


Figure 10. Radial Streamline Shift Across Stators  
(from data reduction using streamline curvature calculation)

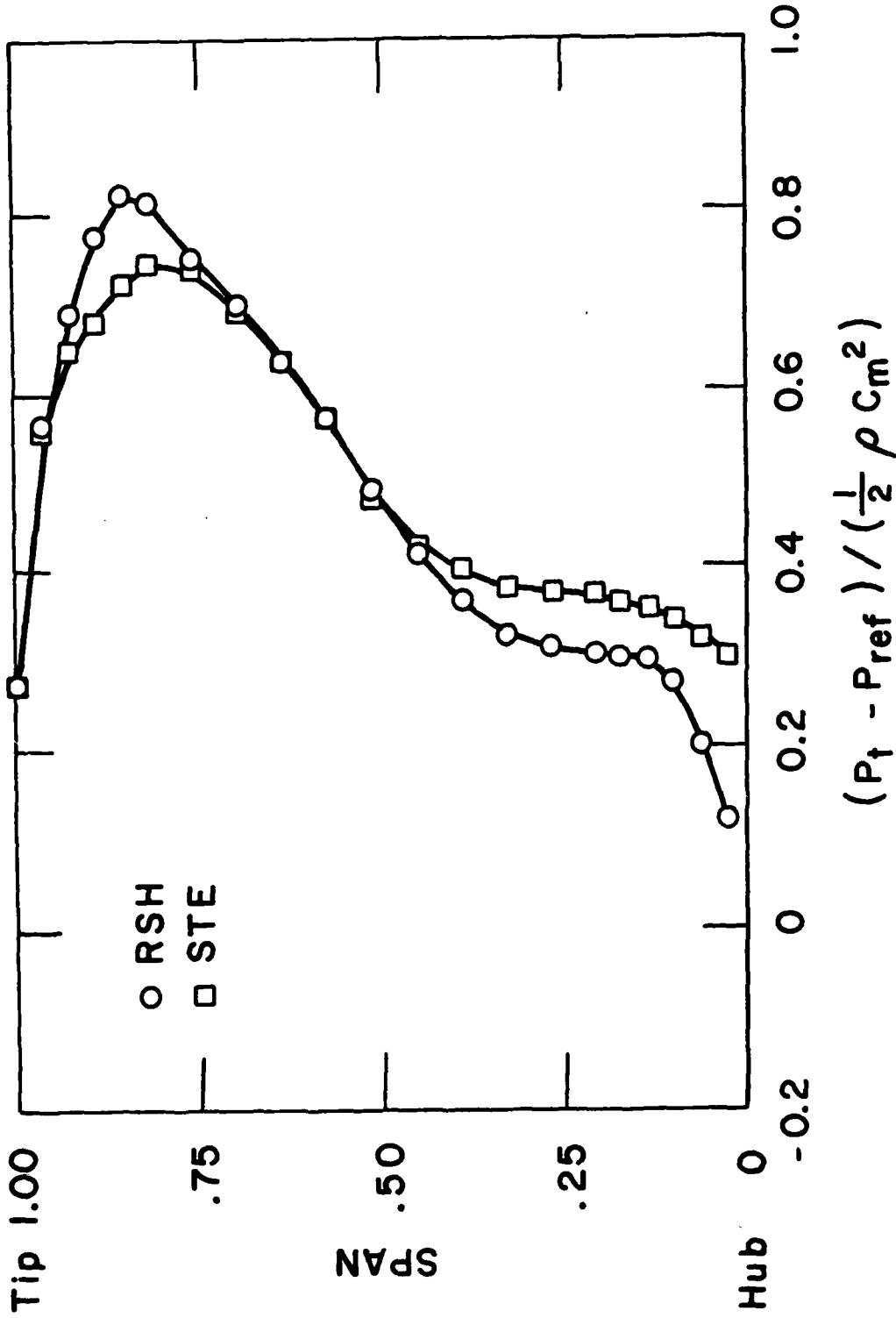


Figure 11. Covected Stator Inlet and (Midpitch) Stator Exit. Total Pressure Distributions (convection of inlet profile based on streamline curvature calculations).

TASK III: INLET VORTEX FLOW DISTORTION IN GAS TURBINE ENGINES

During the past year, work on this project has been focussed on the completion of the inlet flow facility to be used in the Wright Brothers Wind Tunnel, the basic regimes of operation of this facility, and the obtaining of initial data on the overall flow field around the inlet. The details of this work are reported in GT & PDL Report No. 166 (3.1), which is essentially the M.S. Thesis of Mr. Wen Liu.

One of the tasks that was carried out in connection with the facility construction was the fabrication of two inlet models, one of plexiglass for flow visualization and one of aluminum with forty surface pressure taps. The inlets were designed to be separation free using a NASA panel method code and semi-empirical diffusion factor separation criterion (3.3). Another task was the construction of a shear profile generator, which creates a roughly linear velocity profile over the central fifty percent of the tunnel. Also included in this aspect of the project were the calibration of the flow measuring system, the survey of the overall tunnel flow quality, and the development of a tripping device (wire) on the inlet to ensure that operation was not in the subcritical regime. A schematic of the inlet model is shown in Fig. 3.1, which also indicates the pressure tap locations.

Using the facility, basic parametric information has been obtained on the regimes in which a vortex will form. This information is shown in Figure 3.2, which relates to an inlet at ninety degrees of yaw, in a flow with a freestream that is irrotational upstream of the

inlet. The horizontal axis is non-dimensional inlet height above the ground,  $H/D$ , where  $D$  is the inlet inner diameter, and the vertical axis is the velocity ratio  $V_{inlet}/V_{\infty}$ . It can be seen that, as has been found elsewhere (e.g. 3.3), moving to larger values of  $H/D$  or smaller values of  $V_{inlet}/V_{\infty}$  decreases the tendency for an inlet vortex to form. This type of parametric data has also been obtained for an inlet at zero degrees of yaw in a flow with upstream vertical vorticity, as shown in (3.1).

Of more interest, however, is the data on the static pressure distribution on the inlet surface for an inlet at ninety degrees of yaw. These data are plotted in terms of the static pressure coefficient,  $C_p$  ( $= [(P_i - P_{ref})]/(P_i - P)_{ref}$ ), versus azimuthal position round the inlet, for different axial locations, and are shown in Figure 3.3(a to h).

The  $C_p$  distribution is shown for the conditions at which there is a strong vortex:  $H/D = 1.0$ ,  $V_i/V_{\infty} = 16.5$ . The  $C_p$  distribution versus circumferential location (0 degrees being the leading edge, and the angles varying in a clockwise manner so that 90 degree is top and 270 degree is bottom) for the eight axial locations along the inlet is shown in Figures 3.3 (a) to 3.3 (h). Note each graph is plotted on a different vertical scale. Figure 3.4 however, is a composite plot of the  $C_p$  distributions, to the same scale.

At distances far away from the inlet lip, the  $C_p$  distribution is somewhat similar to the  $C_p$  for a two dimensional cylinder, indicating a wake region behind the cylinder. As we approach the lip, the minimum value of  $C_p$  decreases indicating an increase in flow

velocity. The shape of the  $C_p$  distribution changes gradually, with a region of high static pressure appearing at the lower rear of the cylinder. This region of high pressure moves to about the 260 degree position at axial location 4 (1.0 D from the lip). (Note that there is not really a true stagnation point due to the component of surface flow axially along the inlet.)

The shift in the location of the low velocity region from the leading edge to the bottom of the cylinder suggests a change in circulation, increasing towards the lip, as depicted in Figure 3.5. We can draw an analogy to the study reported in Goldstein (3.4) in which a cylinder was spun to create circulation. In that case the front stagnation point also moved towards the lower part of the cylinder as circulation increases.

For axial locations closer to the lip, the  $C_p$  plots show a peak at the 210 degree location indicating a region of low velocity there. A tentative explanation for this is as follows. From the flow visualization study of the trailing vortex, it was shown that the center of the vortex trails from the inlet at roughly the 180 degree position. Referring to Figure 3.6 we can see that there is an interaction between the trailing vortex and the overall flow into the inlet, which could give rise to a region of low velocity at about the 210 degree location.

In addition to the flow associated with the trailing vortex, the ground vortex which is below and in front of the lip at the 180 degree location has some influence on the flow into the inlet, and this would also be expected to give rise to a low velocity region near the 210

degree location, and a high velocity, low pressure, region near the 310 degree location. Because the ground vortex is concentrated in a smaller region than the trailing vortex, the flow induced by the ground vortex is locally stronger as indicated by the  $C_p$  distributions at axial locations 7 and 8 (0.27 D and 0.17 D respectively from the inlet lip); the velocity at the 310 degree location is lower than that induced by the trailing vortex at about the 150 degree location. The pressure distribution thus appears to be at least qualitatively explained using this simple model of varying circulation.

Ref 3.1 also gives details of the flow round the inlet for a low value of  $V_{inlet}/V_\infty$  where we obtain a totally different  $C_p$  distribution near the inlet lip. The composite plot (of all eight axial locations) for this situation is shown in Figure 3.7 where we see, as the inlet lip is approached, a peak in static pressure, i.e. a low velocity region near 180 degrees. This may be explained with reference to Figure 3.8, which we regard as showing, based on our previous work (3.5), two counter-rotating tracking vortices. It can be seen that these will create a low velocity region between them, i.e. near 180 degrees.

In summary, in both situations (the high  $V_{inlet}/V_\infty$  and the low  $V_{inlet}/V_\infty$ ) the pressure distributions appear to be in accord with the conceptual model of the flow round the inlet that we have presented in our previous work.

REFERENCES

- 3.1 Liu, Wen, "Design and Analysis of an Experimental Facility for Inlet Vortex Investigation," M.I.T. GT & PDL Report No. 166, August 1982.
- 3.2 Boles, M.A. and Stockman, N.D., "Use of Experimental Separation Limits in the Theoretical Design of V/STOL Inlets," AIAA Paper 77-878, July 1977.
- 3.3 Glenny, D.E., "Ingestions of Debris into Intakes by Vortex Action," Ministry of Technology, Aeronautical Research Council CP No. 1114, London, 1970.
- 3.4 Goldstein, S., Modern Developments in Fluid Dynamics, vol. 1, Dover, 1965
- 3.5 De Siervi, F. et al., "Mechanisms of Inlet Vortex Formation," Journal of Fluid Mechanics, 124, pp. 173-208, Nov. 1982.

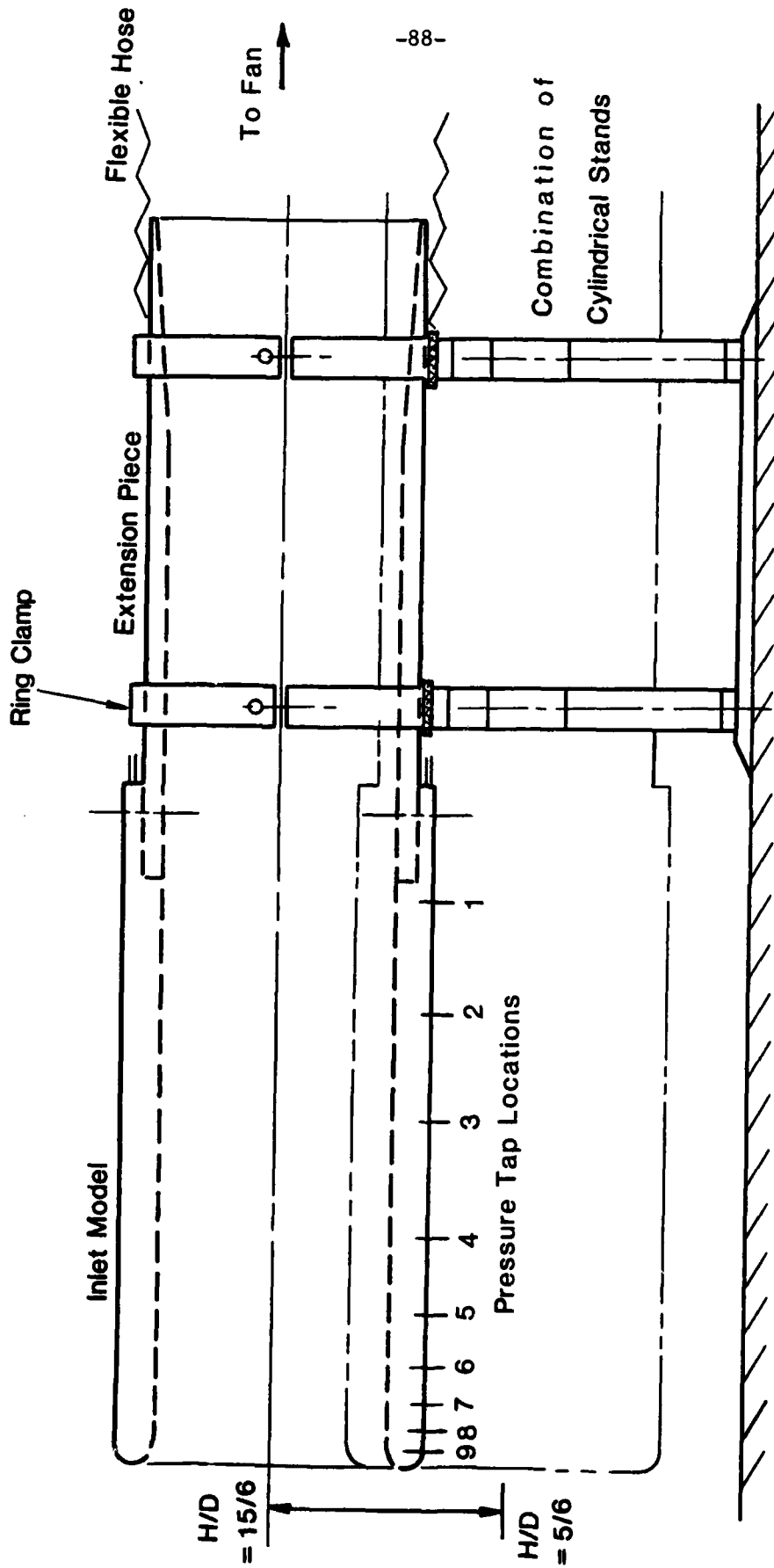


Figure 3.1. Inlet model ( $D = 0.15m$ )

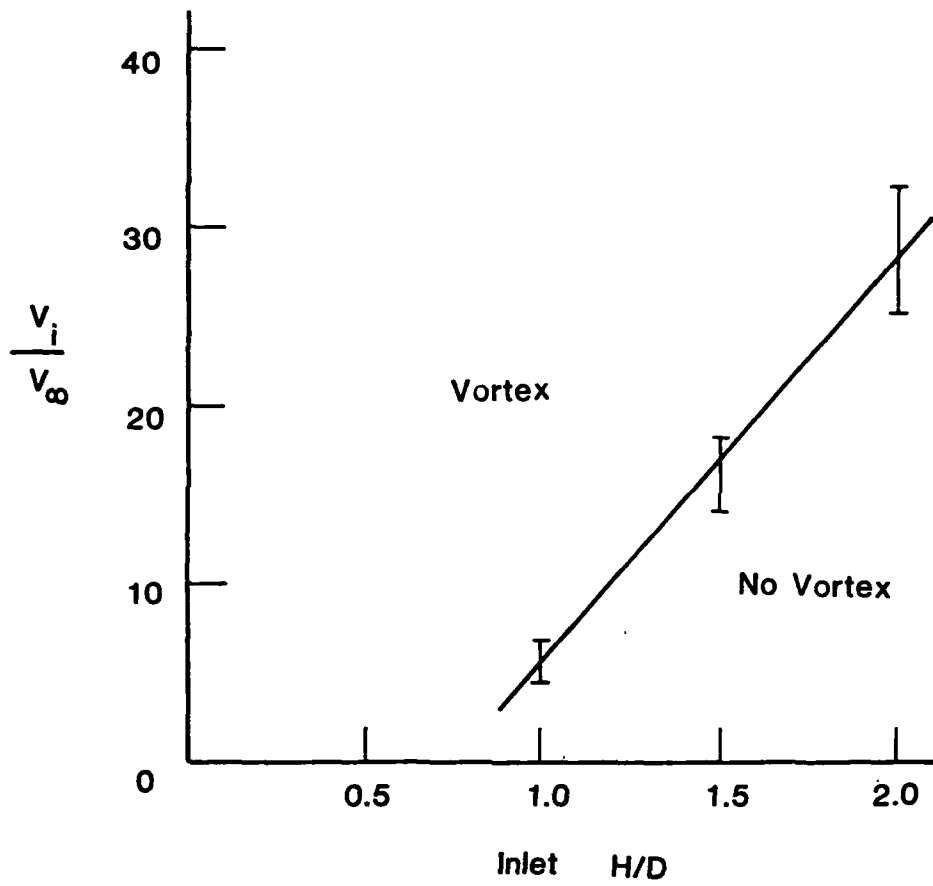


Fig. 3.2 -- Regimes of vortex formation (inlet at 90 degrees of yaw in irrotational freestream)

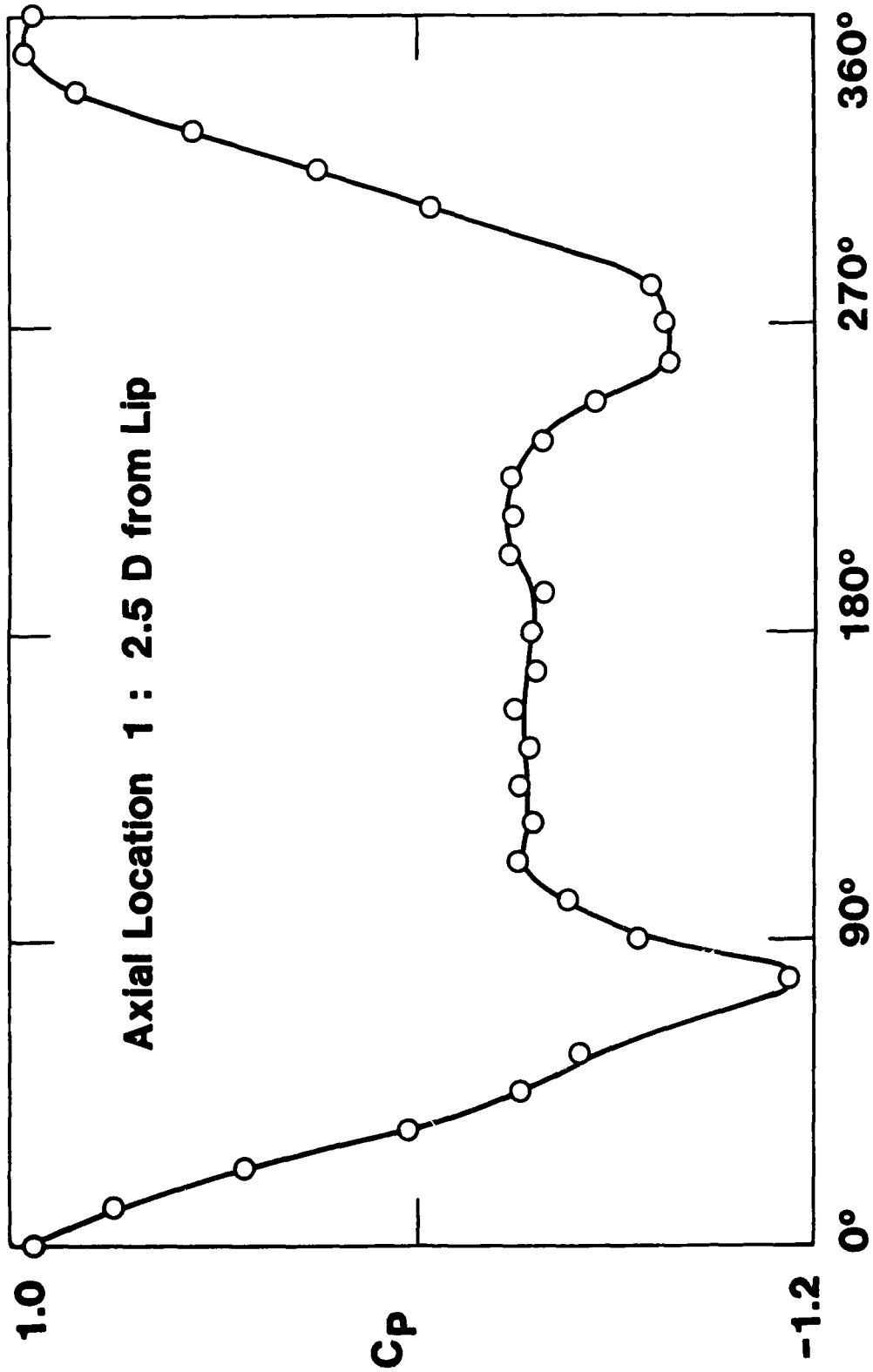


Fig. 3.3a --- Circumferential  $C_p$  Distribution on Inlet at High  $V_1/V_\infty$  (Inlet Vortex Present) at  $90^\circ$  Yaw Configuration in Irrotational Upstream Flow

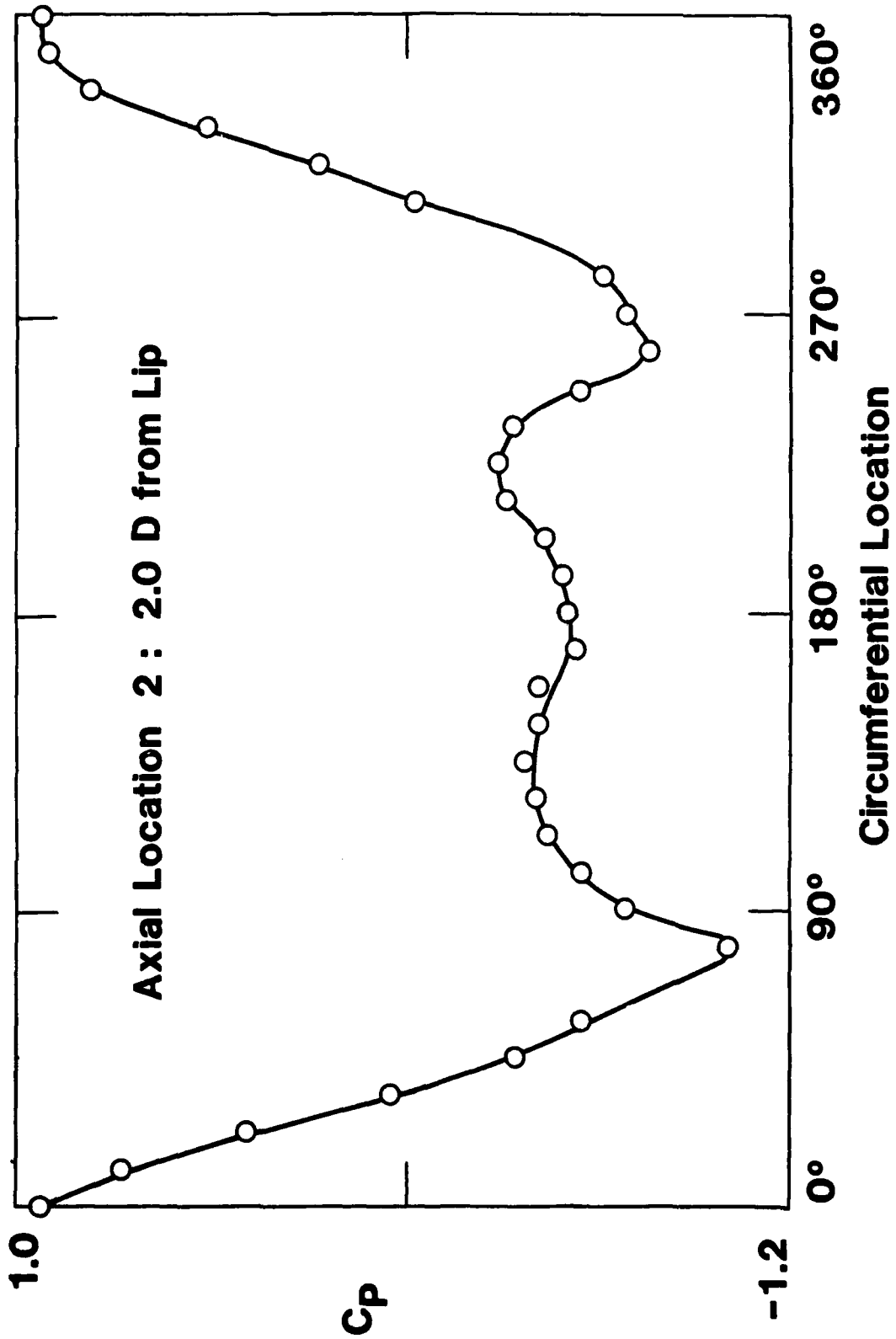


Fig. 3.3b

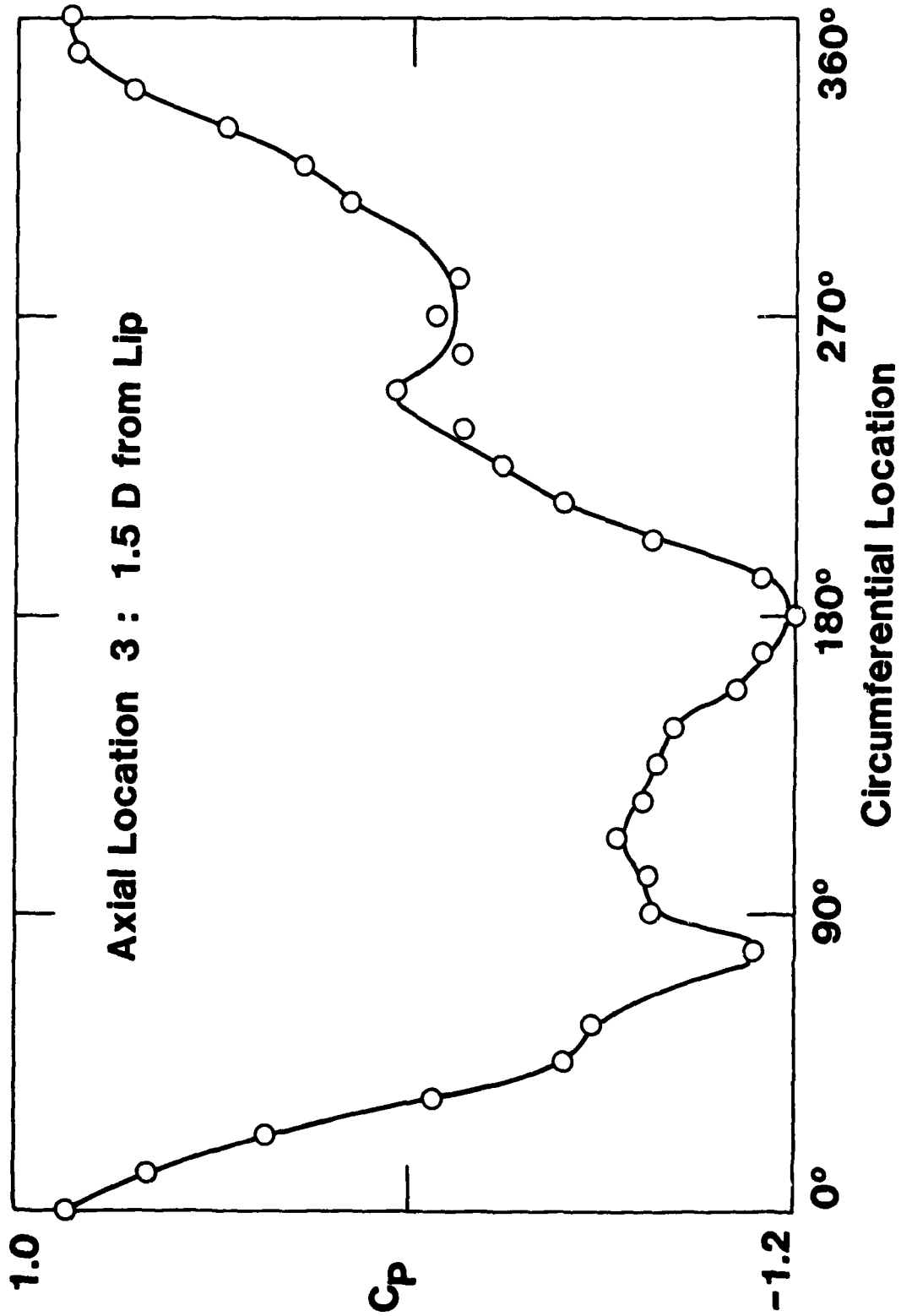


Fig. 3.3c

AD-A126 478

CURRENT PROBLEMS IN TURBOMACHINERY FLUID DYNAMICS(I)  
MASSACHUSETTS INST OF TECH CAMBRIDGE GAS TURBINE AND  
PLASMA DYNAMICS LAB E M GREITZER ET AL. 31 DEC 82  
AFOSR-TR-83-0147 F49620-82-R-0002

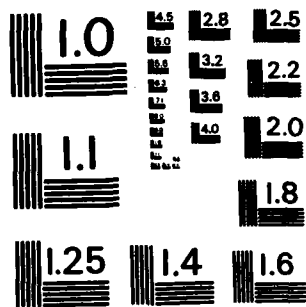
2/2

UNCLASSIFIED

F/G 21/5

NL

													END DATE FILMED C 83 DTIC



MICROCOPY RESOLUTION TEST CHART  
 NATIONAL BUREAU OF STANDARDS-1963-A

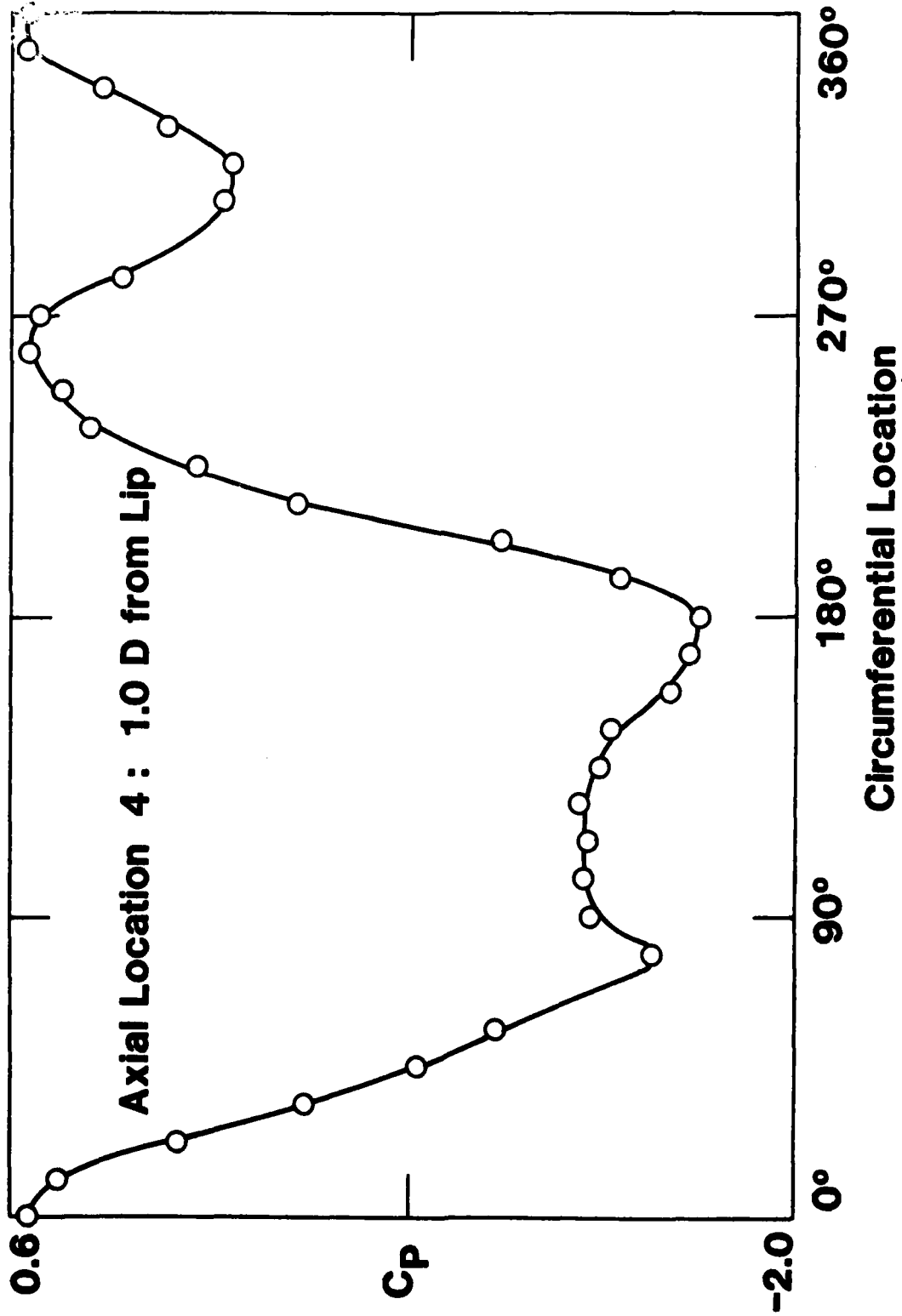


Fig. 3.3d

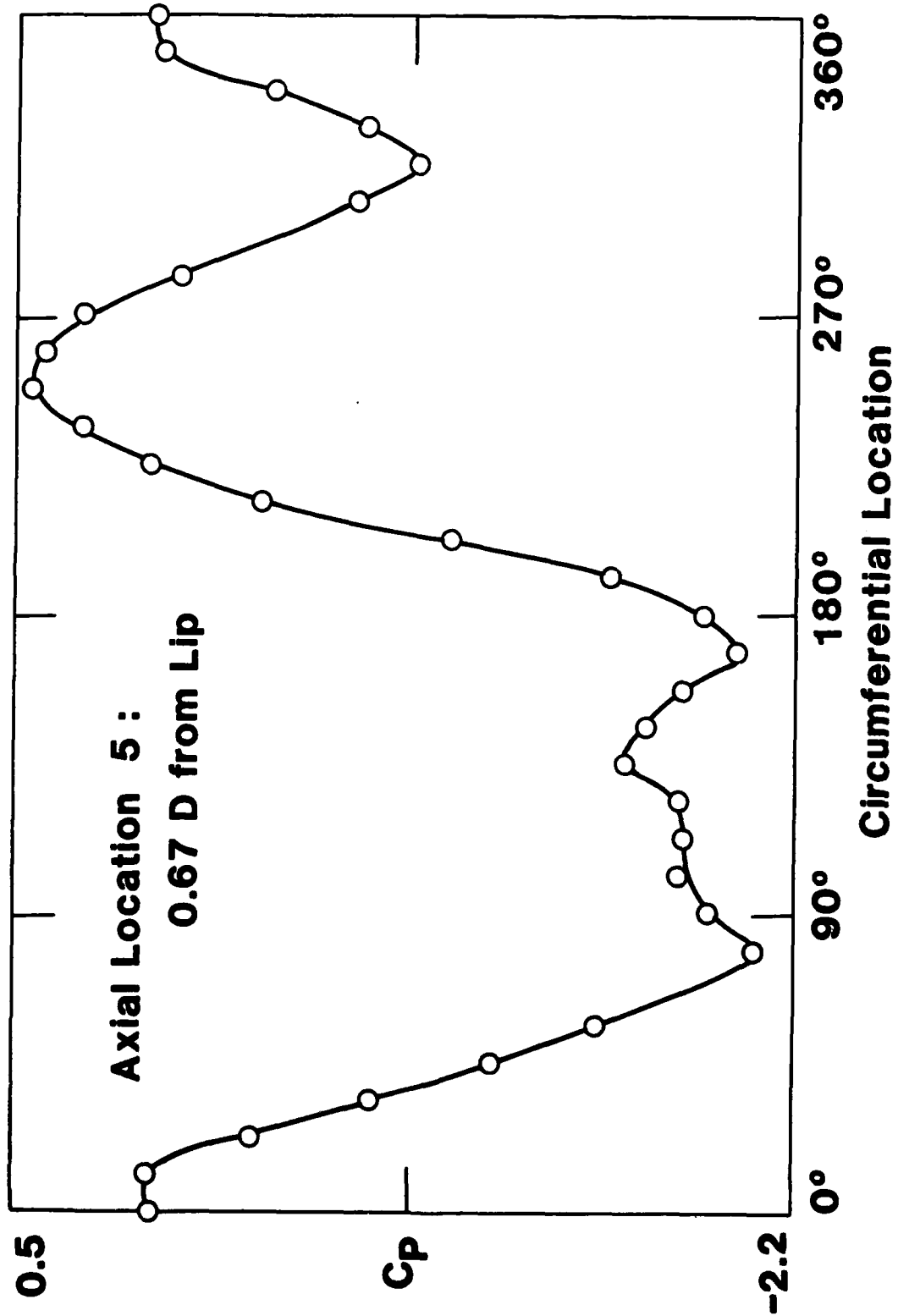


Fig. 3.3e

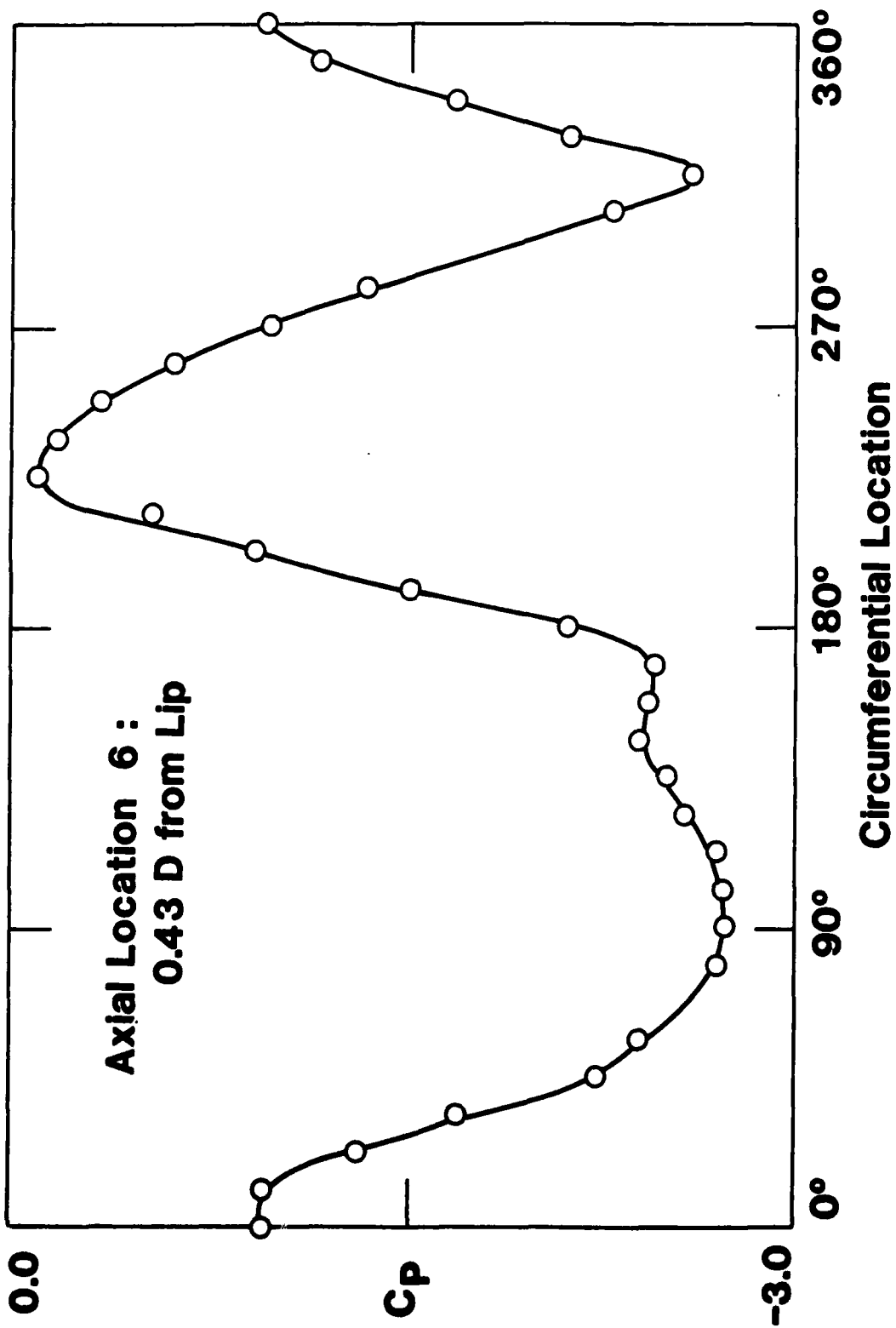


Fig . 3.3f

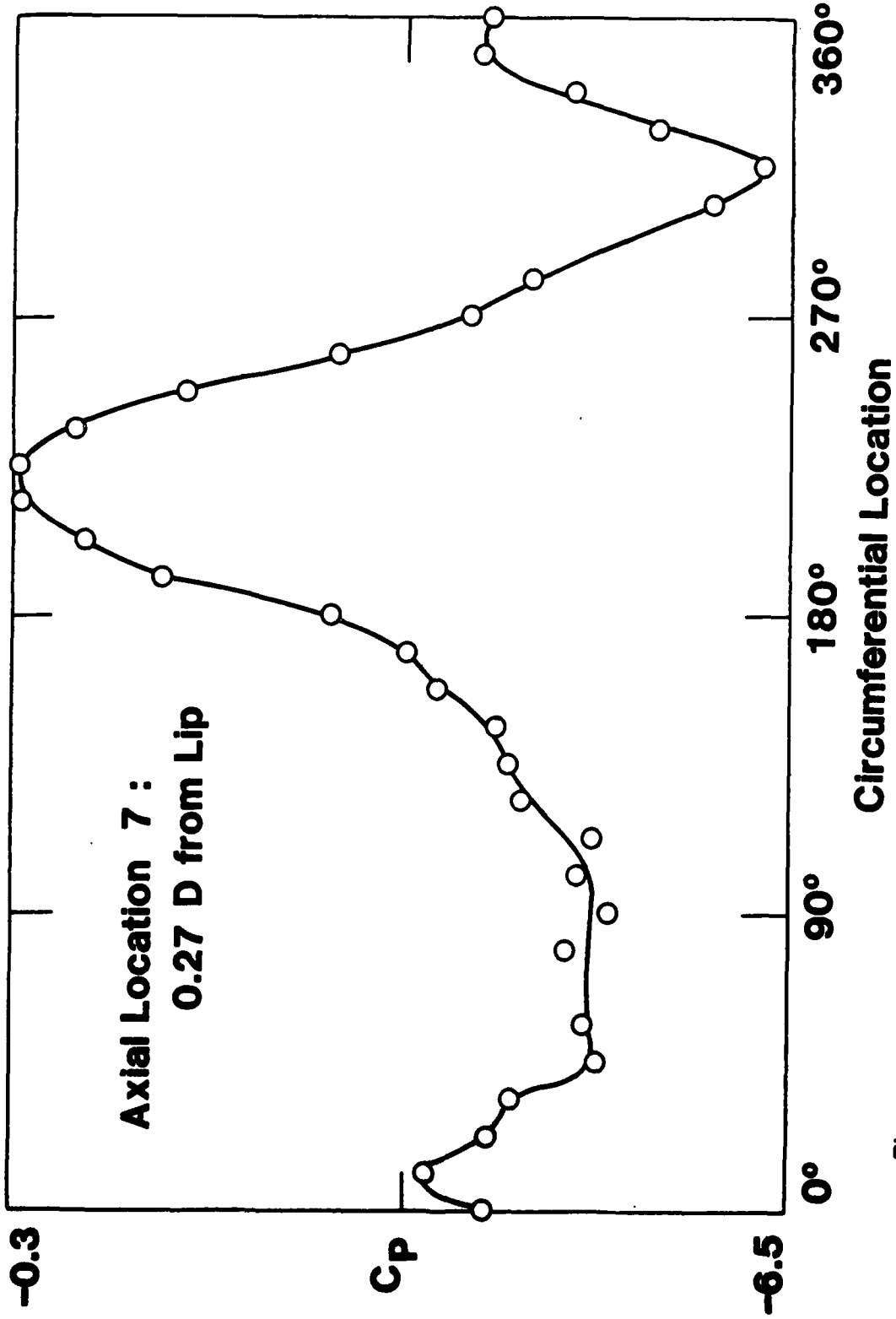


Fig. 3.3g

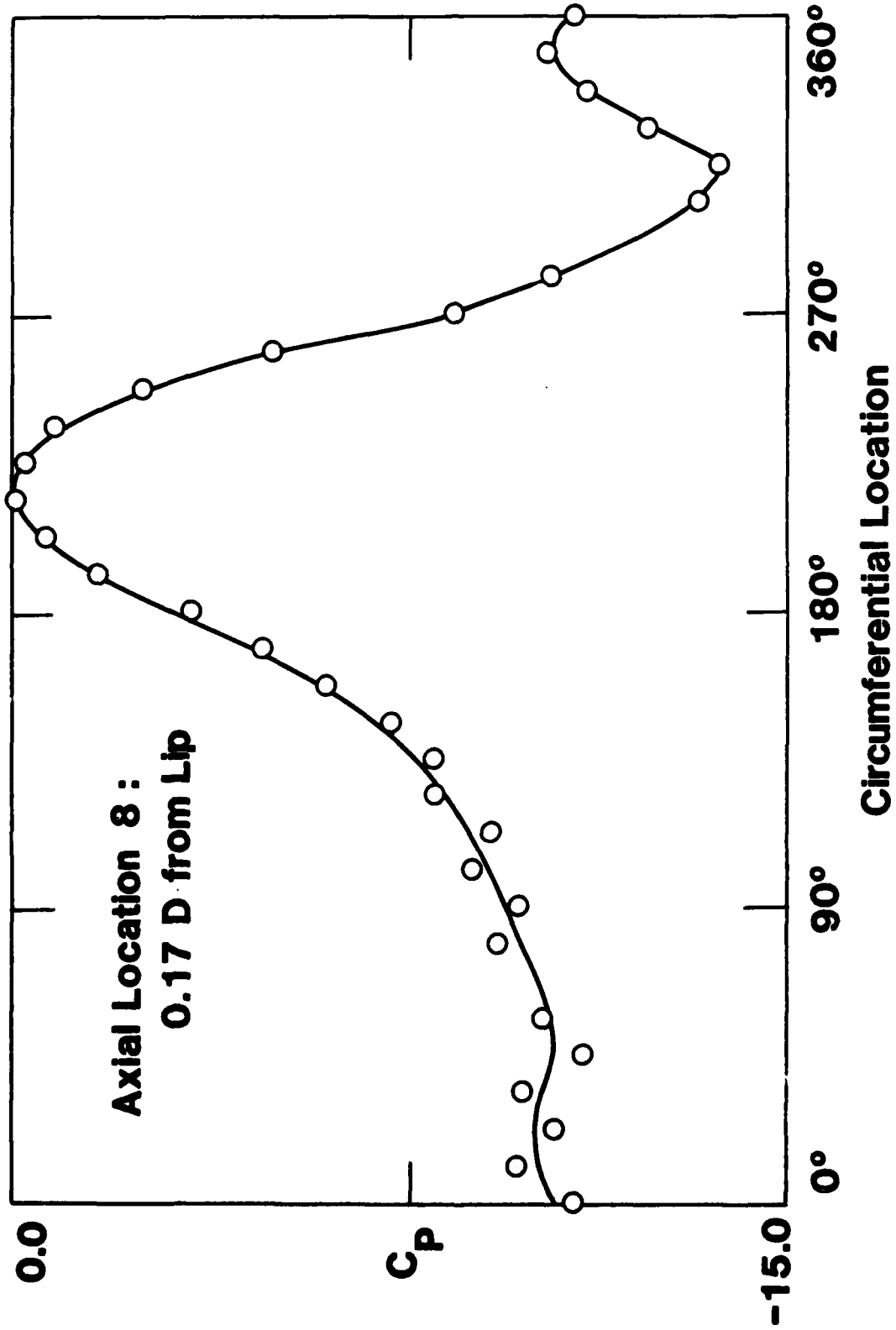


Fig . 3.3h

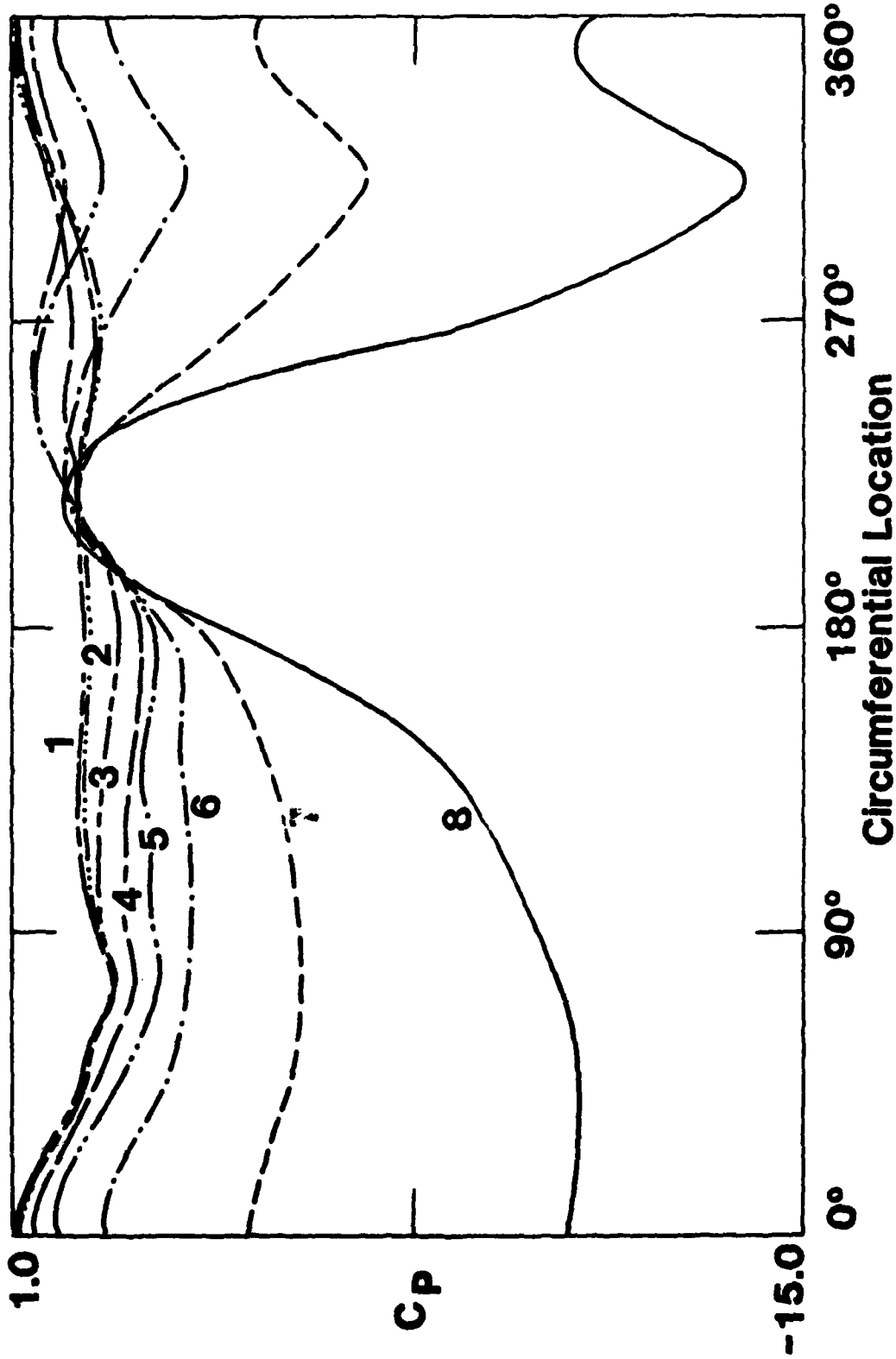


Fig. 3.4 -- Axial Comparison of Circumferential Cp Distribution of Inlet at 90° Yaw Configuration in Irrotational Upstream Flow at High  $V_i/V_\infty$

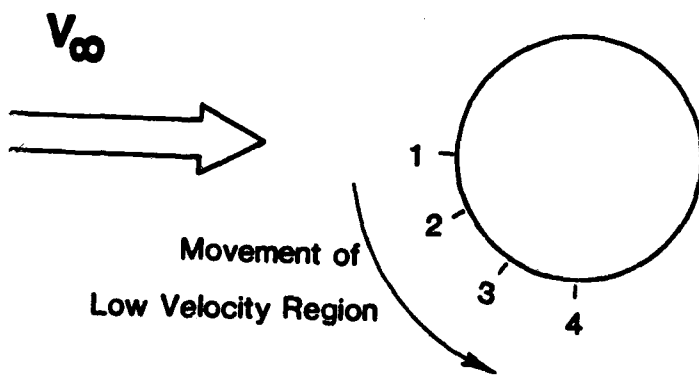
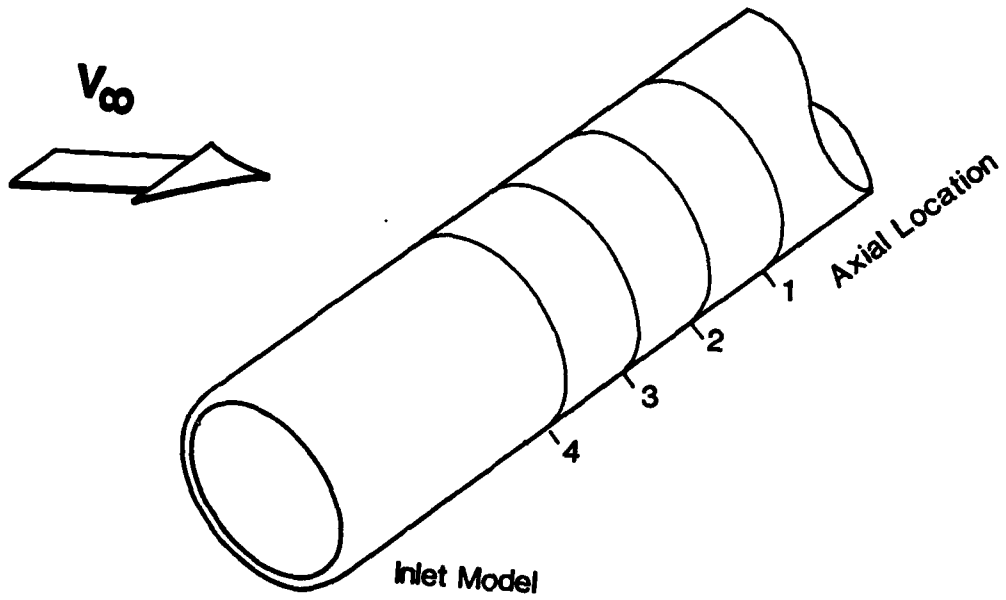


Fig. 3.5 -- Variation of Circulation along Inlet

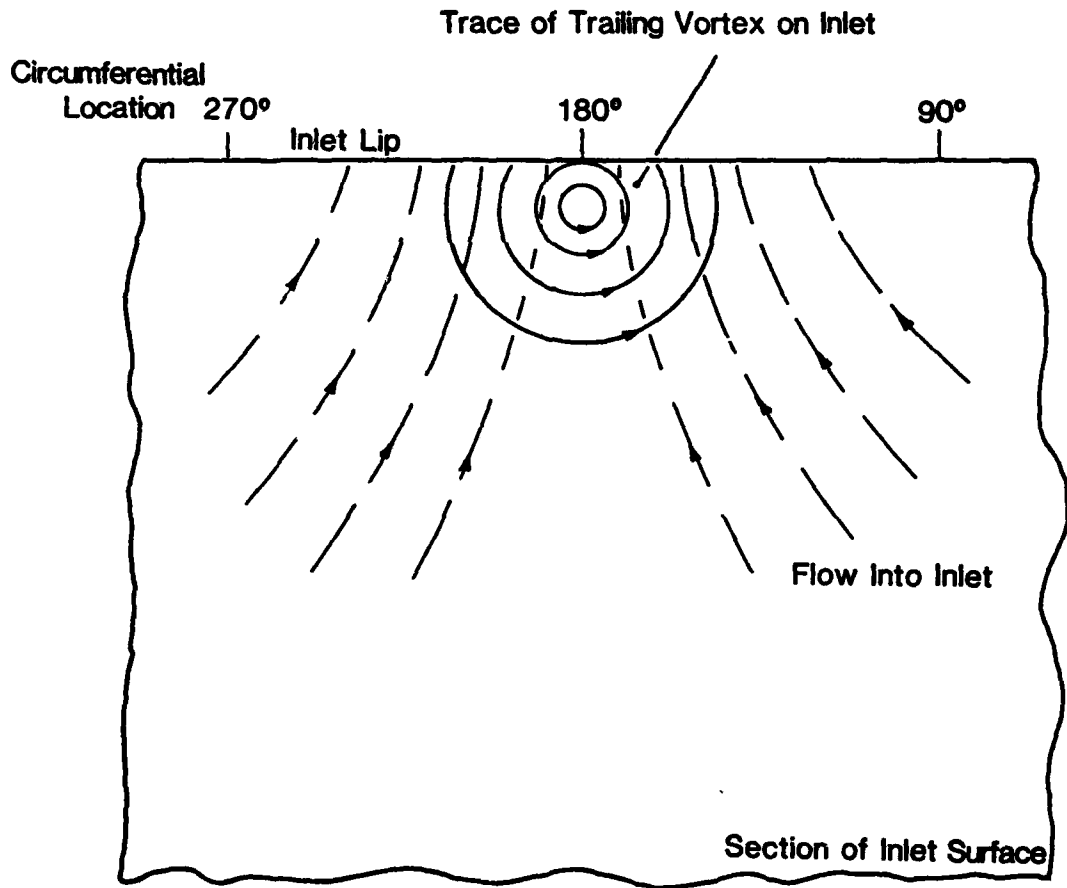


Fig. 3.6 -- Conceptual Model for Interaction of Trailing Vortex and Inlet Flow Field (High  $V_r/V_\infty$ )

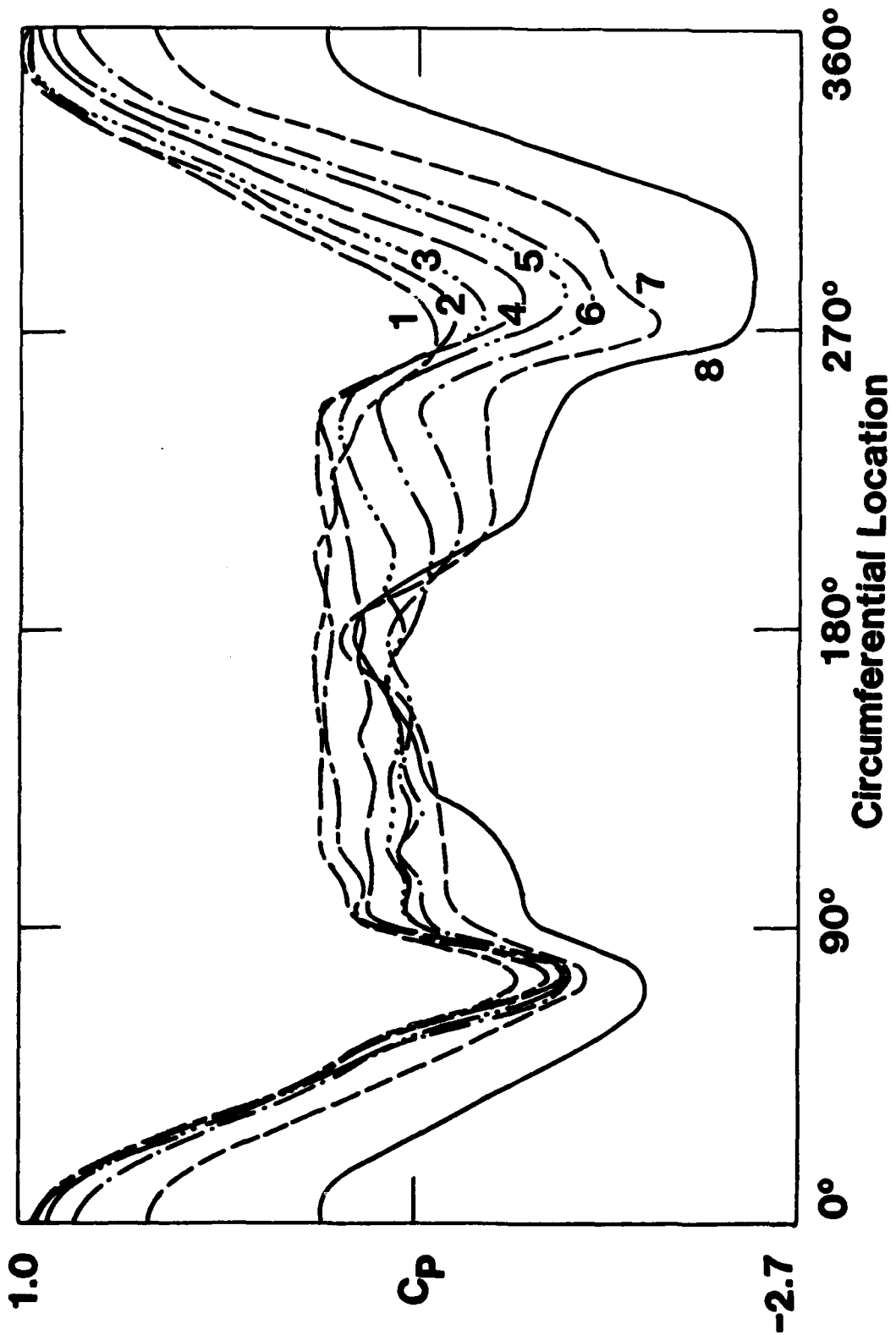


Fig. 3.7 -- Axial Comparison of Circumferential  $C_p$  Distribution of Inlet at 90° Yaw Configuration in Irrotational Upstream Flow at Low  $V_i/V_\infty$

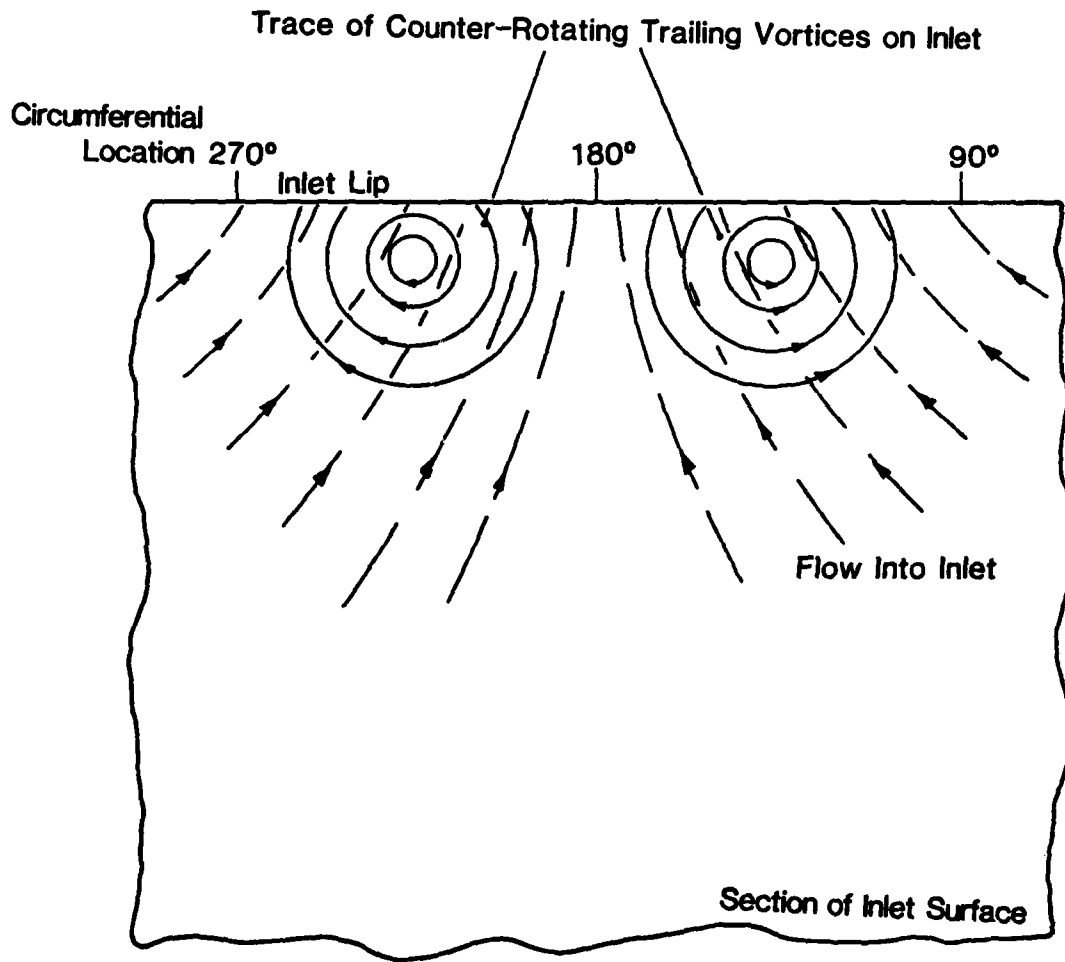


Fig. 3.8 -- Conceptual Model for (counter-rotating) Trailing Vortices/  
Inlet Flow Interaction (low  $V_T/V_\infty$ )

TASK IV: INVESTIGATION OF DISCRETE-BLADE AND 3-D FLOWS  
IN HIGHLY-LOADED TURBOMACHINES

1. Blade to Blade Effects

The following is a report of progress made in the past year in studying blade-to-blade (including 3-D) effects in practical turbomachine flows of high loading. Part of the emphasis is on contribution to improved design techniques, using modified non-linear analytic techniques.

Successful non-linear calculations of incompressible three-dimensional flow through high-swirl blade rows, using "very thin" blades have been reported earlier. Those results confirm expectations of significant 3-D effects. But they also suggested the importance of exploring additional modifications that may arise from blade-row blockage (blade thickness).

Proper treatment of "leading-edge" stagnation points, "Venturi" effects in the intra-blade region, and the trailing edge Kutta conditions could all be expected, it was thought, to modify the blade shapes needed to accomplish a given task. Significant differences in required camber, depending on the blockage, was to be expected.

During this reporting period application of modified non-linear wing theory methods have been successfully applied to treat this problem.

Taking advantage of the periodic symmetry of typical blade rows, and the fact that they frequently comprise many blades, an asymptotic expansion of the blade-row "Green's functions" can be found. Using

this result in a more-or-less classical manner for the solution of fluid flow boundary-value problems leads to an analytical method which we call "smoothing." This appears to greatly reduce the work required to solve blade row problems.

This "smoothing" technique has now been successfully applied to the "blockage" or "thickness" problem in designing highly-loaded blades in a 2-D cascade of high swirl.

One feature of the above results is that one can now explore, cheaply and efficiently, a wide variety of intrablade design choices. Included, for example, is the possibility of finding out what blockage distributions (chordwise) are favorable or unfavorable for given loading distributions (or whirl schedules). This work comprised the master's thesis of Mr. Thong Dang.

2. Non-Axisymmetric Compressible Swirling Flow in Turbomachine Annuli

An analysis of the behavior of non-axisymmetric disturbances in a swirling compressible flow typical of those found in turbomachine annuli has been completed. The results of this work will appear in the near future as GT & PDL Report No. 169.

The analysis used is based on the Clebsch transformation. For the flows analyzed, the different types of flow disturbances (vorticity, entropy and pressure) are strongly coupled, due to the swirl. Numerical examples are presented to show that the mean flow Mach number can have an influence on the magnitude and downstream evolution of the non-axisymmetric disturbances. In particular, at high subsonic Mach number, the amplitude of the disturbances can oscillate with decreasing modulation in the flow direction. In addition to the general analysis that is presented, another much simpler model (which only considers one class of non-axisymmetric disturbance) is also used to examine the static pressure non-uniformities that can occur in such flows.

To illustrate the magnitude of the effects that are due to compressibility, fig. 4.1 shows the evolution of the downstream static pressure distributions for three different far upstream Mach numbers: 0.1, 0.5, and 0.9. Note that the example shown is a rotor in a annulus of constant hub and tip diameter. With the present calculations, it is necessary to set the far upstream Mach number at the quite high value of 0.9 to obtain a downstream mach number in the

high subsonic regime. This, however, should not be important as far as the downstream evolution is concerned.

3. Theory of Blade Design for Large Deflections

A three dimensional method of designing highly loaded blades (both two-dimensional and annular blades) to give a specified distribution of swirl has been formulated. For the initial work, the flow is assumed to be incompressible and inviscid (the annulus has constant hub and tip radii), the blades are of negligible thickness; and a simple free vortex swirl schedule is assumed for the case of annular blades. Numerical calculations have been carried out to show the magnitude of the effects in parameter regimes of interest. The results of this work (two papers) have been submitted to the ASME for the 1983 Gas Turbine Conference. Abstracts of the two papers are reproduced below. The papers themselves are given as Appendix B. In addition, the theoretical and computational details will appear in GTL Report No.168.

Theory of Blade Design for Large Deflections

Part I: Two Dimensional Cascades

A method of designing two dimensional cascades of highly loaded blades to give a specified distribution of tangential velocity is presented. The fluid is assumed to be incompressible and inviscid and the blades of negligible thickness. The blades are represented by a distributed bound vorticity whose strength is determined by the prescribed tangential velocity. The velocity induced by the bound

vortices is obtained by a conventional Biot-Savart method assuming a first approximation to the blade profile. Using the blade surface boundary condition, the profile is then obtained by iteration. It is shown that this procedure is successful for large pitch-chord ratios and large deflections. In order to develop a method for use in three dimensions, the velocity is divided into a pitchwise mean value and a value varying periodically in the pitchwise direction. By using generalized functions to represent the bound vorticity and a Clebsch formulation for the periodic velocity, series expressions are obtained which can be adapted to three dimensional problems. Several numerical results are obtained using both approaches.

Theory of Blade Design for Large Deflection

Part II: Annular Cascades

A method of designing highly loaded blades to give a specified distribution of swirl is presented. The method is based on a newly-developed three-dimensional analysis. In the present application, the flow is assumed to be incompressible and inviscid (the annulus has constant hub and tip radii) and the blades are of negligible thickness. A simple free vortex swirl schedule is assumed. The flow velocity is divided into circumferentially averaged and periodic terms. The Clebsch formulation for the periodic velocities is used and the singularities are represented by periodic generalized

functions so that solutions may be obtained in terms of eigenfunctions. The blade profile is determined iteratively from the blade boundary condition.

Results from the computer program show how blade number, aspect and hub-tip ratios affect the blade shape. The blade profiles for a given swirl schedule depend not only on the aspect ratio but also on the stacking position (i.e., the chordwise location at which this thin blade profile is radial), and so too do the mean axial and radial velocities. These effects occur whether the number of blades is large or small, and we conclude that even in incompressible flow the blade element or strip theory is not generally satisfactory for the design of high deflection blades. The analysis derives conditions for the blade profiles on the walls of the annulus as well as the mean swirl velocity there and at the trailing edge.

In the limit when the number of blades approaches infinity, a bladed actuator duct solution is obtained. The conditions for the blade profile at the walls are absent, but the stacking position and aspect ratio still affect the axial and radial velocity distributions for the same swirl schedule.

4. Numerical Studies of Secondary Flow in a Bend Using Spectral Methods

A numerical algorithm for solution of the incompressible Navier-Stokes equations for flow in a bend of square cross-section has been formulated. The momentum equation has been written in rotational form as

$$\frac{\partial \vec{V}}{\partial t} = \vec{V} \times \vec{\omega} - \nabla \pi + \nu \nabla^2 \vec{V} \quad (1)$$

and the continuity equation is simply

$$\nabla \cdot \vec{V} = 0 \quad (2)$$

For Eq. 1 and 2,  $\vec{V}$  is the velocity vector,  $\vec{\omega}$  the vorticity,  $\pi$  the stagnation pressure normalized by the density, and  $\nu$  the kinematic viscosity. A cylindrical coordinate system  $(r, \theta, z)$  is used with the square section of the bend lying on the  $r - z$  plane.

The fractional time stepping technique has been proposed to advance the Navier-Stokes equation<sup>1</sup> in time as follows:

(1) The convective (or advective) part:

The first fractional step is the convective part. A semi-implicit Crank-Nicholson-Adams-Bashforth Scheme is used and yields

$$\underbrace{\frac{\vec{V}^{(1)n+1} - \vec{V}^n}{\Delta t} + \frac{1}{2} \frac{\vec{v}_\theta}{r} \frac{\partial \vec{V}}{\partial \theta}}_{\text{Implicit Crank-Nicholson for stabilization of time stepping}} \vec{V}^{(1)n+1} = \frac{3}{2} (\vec{V} \times \vec{\omega})^n - \frac{1}{2} (\vec{V} \times \vec{\omega})^{n-1} + \frac{\vec{v}_\theta}{r} \frac{\partial \vec{V}^{(1)n}}{\partial \theta} - \frac{1}{2} \frac{\vec{v}_\theta}{r} \frac{\partial \vec{V}^{(1)n-1}}{\partial \theta} \quad (3)$$

Explicit Adams-Bashforth part

$\bar{v}_\theta$  is the value of the bend through-flow velocity at the inflow boundary. Superscript (1) denotes the first fractional time step while superscript n denotes the time level. For this part, no outflow B.C. are required as the spectral method does not introduce spurious B.C. The inflow boundary conditions are:

$$\begin{aligned} v_r &= 0 \\ v_\theta &= C_0(1 - R^2)(1 - Z^2) \\ v_z &= 0 \end{aligned} \tag{4}$$

(2) The pressure correction step:

The second fractional step enforces the incompressibility condition and the normal wall boundary conditions, which are not required by the first fractional step. This is achieved via the solution of  $\pi$  from

$$L[\pi] = \frac{1}{\Delta t} \nabla \cdot \vec{v}^{(1)n+1} \tag{5}$$

where L is the appropriate Laplacian operator in  $(R, \phi, Z)$  space mapped from the cylindrical co-ordinate space  $(r, \theta, z)$ . The boundary conditions imposed on  $\pi$  are:

$$\frac{\partial \pi}{\partial R} = \frac{(r_o - r_i)}{2\Delta t} v_r (1)n+1 \quad \text{at } R = \pm 1 \quad (6a)$$

$$\frac{\partial \pi}{\partial z} = \frac{1}{\Delta t} v_z (1)n+1 \quad \text{at } Z = \pm 1 \quad (6b)$$

$$\frac{\partial \pi}{\partial \phi} = \frac{1}{2} \frac{\theta_o}{\Delta t} \left( \frac{v_o - v_i}{2} R + \frac{r_o + r_i}{2} \right) v_\theta (1)n+1 \quad \text{at inflow boundary} \quad (6c)$$

$$\frac{\partial \pi}{\partial \phi} = 0 \quad \text{at the outflow boundary} \quad (6d)$$

( $\theta_o$  is the angle of the bend,  $r_i$  and  $r_o$  are the inner and outer radius of the bend)

(Note that the imposed outflow boundary condition, Equation (6d), is not strictly correct, and we will be attempting to improve (6d) utilizing a linearized secondary flow analysis.) In eqn. (6), we have used subscript ( $r, \theta, z$ ) to denote vector component in the  $r$ -,  $\theta$ -,  $z$ - direction. The corrected velocity field  $\psi(2)n+1$  is obtained through

$$\psi(2)n+1 = \psi(1)n+1 - \Delta t \nabla \pi \quad (7)$$

(3) The viscous correction step:

The final fractional step consists of imposing the no-slip conditions at the walls together with appropriate inflow and outflow B.C. The backward Euler-like scheme is used and it yields

$$\frac{v_r^{n+1} - v_r^{(2)n+1}}{\Delta t} - v \left( \nabla^2 v_r^{n+1} - \frac{v_r^{n+1}}{r^2} \right) = - \frac{2v}{r^2} \frac{2v_\theta^{(2)n+1}}{\partial \theta} \quad (8)$$

$$\frac{v_\theta^{n+1} - v_\theta^{(2)n+1}}{\Delta t} - v \left( \nabla^2 v_\theta^{n+1} - \frac{v_\theta^{n+1}}{r^2} \right) = - \frac{2v}{r^2} \frac{2v_r^{n+1}}{\partial \theta} \quad (9)$$

$$\frac{v_z^{n+1} - v_z^{(2)n+1}}{\Delta t} - v \nabla^2 v_z^{n+1} = 0 \quad (10)$$

Steps (1) and (2) are of  $O(\Delta t^2)$  while step (3) is of  $O(v\Delta t)$ . However, due to the curvature term, the pressure and the viscous operator do not commute, therefore the overall accuracy will be of  $O(\Delta t)$ . However,  $O(\Delta t^2)$  may be achievable by alternating the direction of fractional stepping. It should also be mentioned that the implementation of fractional step (1) and (2) only, will yield an inviscid solution of the flow.

We have proposed to expand the velocity field  $\vec{v}$  and the stagnation pressure  $\pi$  in triple chebyshev series. Consequently, we have developed software: (1) to compute and invert single, double and triple Chebyshev series efficiently using FFT; (2) to compute the derivatives of function efficiently given the Chebyshev coefficients of the function. This includes one-dimensional, two-dimensional and three-dimensional functions. (3) To solve the three-dimensional Poisson equation in a cylindrical co-ordinate system with both Neumann type of boundary conditions (pressure step), and Dirichlet boundary conditions (various step). We have tested the software developed in

(1) and (2) rather exhaustively (against known analytical functions) to ensure the correctness of the software.

For the three-dimensional Poisson solver, we have initially proposed the use of a tensor-product technique with diagonalization in the  $\phi$  and  $z$  direction and spectral iteration in the radial direction. The spectral iteration operator chosen is the second finite difference operator for  $\partial^2/\partial r^2 + (1/r) \partial/\partial r$  with the appropriate boundary conditions. However, we are now in favor of a slightly different method for the solution of three-dimensional Poisson equation in the cylindrical co-ordinate system. In this method, we still perform the diagonalization in the  $\phi$ - and  $z$ - direction, but we now use a collocation approximation for the operator in the radial direction. An eigensolver is then used to diagonalize the collocation operator to reduce the storage and number of operations required for the solution. The current technique still requires a preprocessing stage. The software has been developed for this and has been tested on model equations with homogenous B.C. with known analytical solution. For inhomogenous boundary conditions, it is necessary to invent a function (usually a polynomial) to make the boundary conditions homogenous with a resulting modification of the source term on the R.H.S. of the Poisson equation for this method to work. We have found that the invention of such a function to be rather inconvenient (especially for the case of inhomogenous Neumann Boundary condition which is the case

for the Pressure step here). We expect to modify our current scheme so that the case of a general boundary condition of the mixed type can be handled conveniently.

It is noted that the use of Chebyshev polynomials in the r-z plane leads to a good resolution of the boundary layers at the walls. However, its use in the  $\phi$  direction does lead to some wasteful resolution in the inflow and outflow boundaries. Besides, since spectral methods are global, therefore any error incurred during the imposition of outflow boundary conditions (e.g. 6d) may not tend to be localized. Thus we may anticipate the modification to finite difference approximation in the  $\phi$ -direction to alleviate the wasteful resolution at the inflow and outflow boundaries and to localize the errors incurred in the imposition of outflow boundary condition such as that in equation 6d.

5. Numerical calculation of flow in casing treatment grooves

Work is in progress on the calculation of the flow in a rectangular slot, characteristic of those used in rotor casing treatment. The flow is assumed to be inviscid, incompressible, irrotational, and two-dimensional. The boundary condition, in addition to the usual vanishing of the normal velocity at the solid walls, is the time-dependent pressure distribution imposed by the passage of rotor blades on the open end of the rectangular slot. In mathematical terms, we solve the following problem:

$$\nabla^2 \phi = 0 \quad (1)$$

in  $-1 \leq x \leq 1$ , and  $-1 \leq y \leq 1$  (see fig. 4.2)

subjected to the boundary conditions:

$$\frac{\partial \phi}{\partial x} = 0 \quad \text{at } x = \pm 1 \quad (2a)$$

$$\frac{\partial \phi}{\partial y} = 0 \quad \text{at } y = -1 \quad (2a)$$

$$\text{and } \Omega \frac{\partial \phi}{\partial t} + (\nabla \phi)^2 + p = \text{constant} \quad \text{at } y = 1 \quad (2c)$$

The above equations have been appropriately made dimensionless:  $\phi$  is the velocity potential and  $p$  is the pressure distribution at the open end.  $\Omega$  ( $2 \times$  blade passing frequency  $\times$  slot length/blade tip speed) can be taken as a reduced frequency parameter providing a measure of the importance of unsteadiness.

A typical time-dependent pressure distribution at 8 different time levels at the open end of the groove constructed from the blade pressure distributions given in the Ph.D. thesis by Smith (4.2), is shown in fig. (4.3a). The time-averaged pressure distribution is shown in fig. (4.3b).

Several numerical methods, including spectral and finite difference schemes, were tried. Spectral expansions were either in Chebyshev polynomials or cosine functions (the natural eigenfunction of the system). Temporal resolution was either in Fourier series (taking advantage of the time periodicity) or in simple finite

difference form (Euler, leapfrog, etc.). Because of the nonlinearity of the boundary condition at  $y = 1$  (eg. 2c), iteration of the relaxation type

$$\phi^{iH} = \phi^i + \mu [\Omega (\partial\phi/\partial x) + (R\phi)^2 + p - \text{constant}] \quad (3)$$

was used in the spectral calculation. Satisfactory convergence was only obtainable for imaginary relaxation factor  $\mu$  and 5 spectral modes, neglecting the D.C. (timewise) component of the pressure at the open end. The use of spectral modes greater than 5 yielded a non-satisfactory convergent solution. For real relaxation factor  $\mu$ , the computational procedure was unstable. For the finite difference schemes that were tried, no satisfactory convergent solution is obtained. The details and results of work described above is documented in the M.S. Thesis of P. Kletzkine.

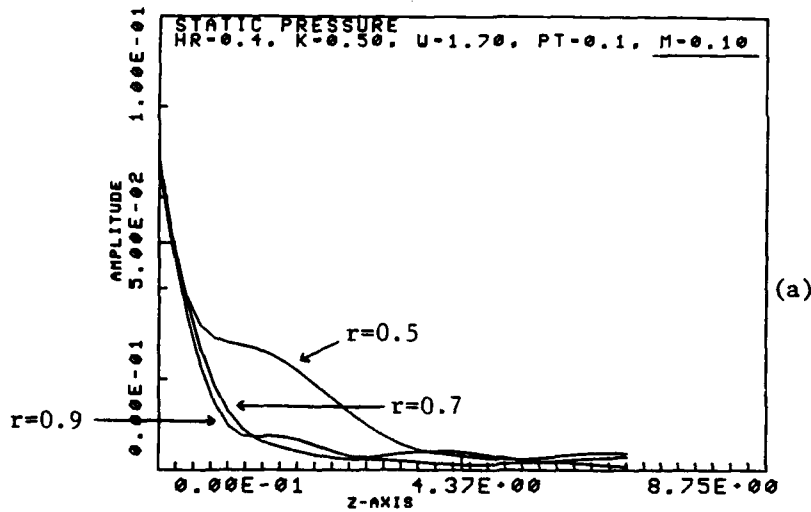
Recently, we have implemented the calculation of the time-averaged flow using the pressure distribution shown in fig. 4.3b. The spectral expansion used for  $\phi$  is a cosine series. The nonlinearity of the boundary condition at the open end (fig. 4.3c) results in multiple solutions for the same given pressure distribution. The most physically realistic solution, corresponding to the pressure distribution in fig. 4.3b, is shown in fig. 4.4.

We are currently attempting to develop a robust technique for the solution of equation 1 subjected to boundary conditions 2. Currently, we are also investigating other ways (e.g. using the primitive variables  $p$  and velocity components  $u$  and  $v$ ) of

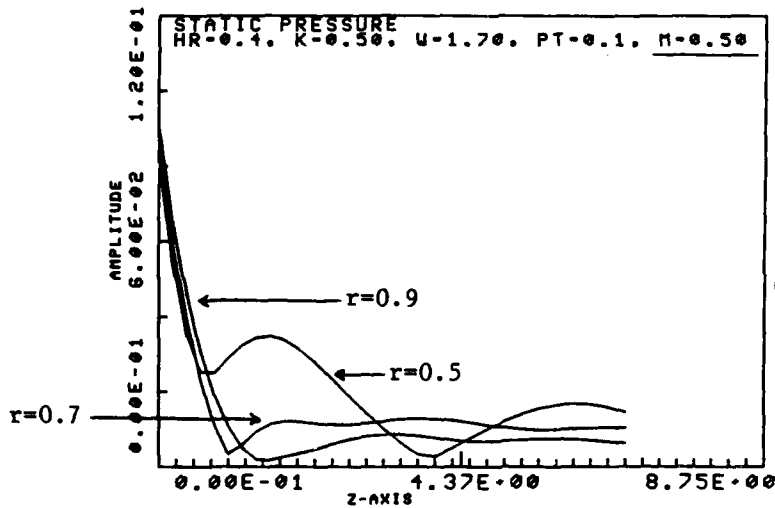
numerically computing such a flow field. For this latter work, the flow does not have to be irrotational.

REFERENCES

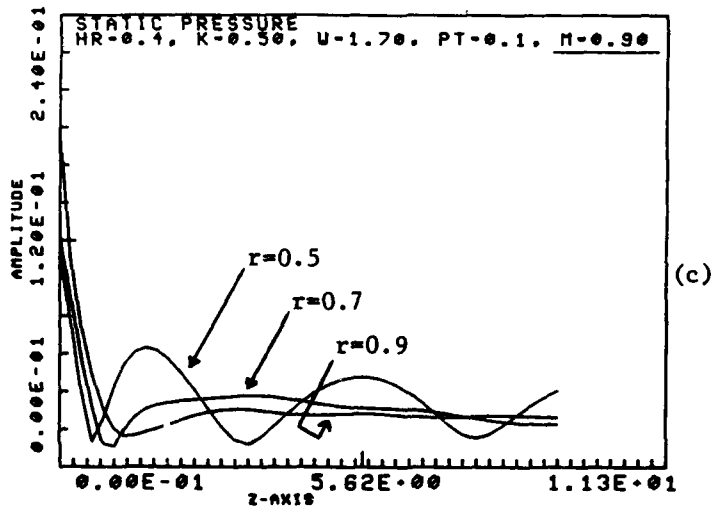
- 4.1 Kells, L.C. and Orsgag, S.A., "Transition to Turbulence in Plane Coette Flow," Journal of Fluid Mechanics, 96, (1980), pp.159-205.



(a)



(b)



(c)

HR = hub-to-tip ratio

r = radius/tip radius

$\bar{V}_\theta$  = mean tangential velocity

$\bar{V}_{z-\infty}$  = far upstream axial velocity

$$K = \frac{r\bar{V}_\theta}{\bar{V}_{z-\infty}}$$

$W = \frac{1}{\text{flow coefficient at tip}}$

PT = amplitude of upstream total pressure distortion

M = far upstream Mach number

Z = axial distance from the blade row

Fig. 4.1 -- Rotor: Downstream evolution of static pressure perturbation amplitude at various radii for M = 0.1, 0.5, and 0.9.

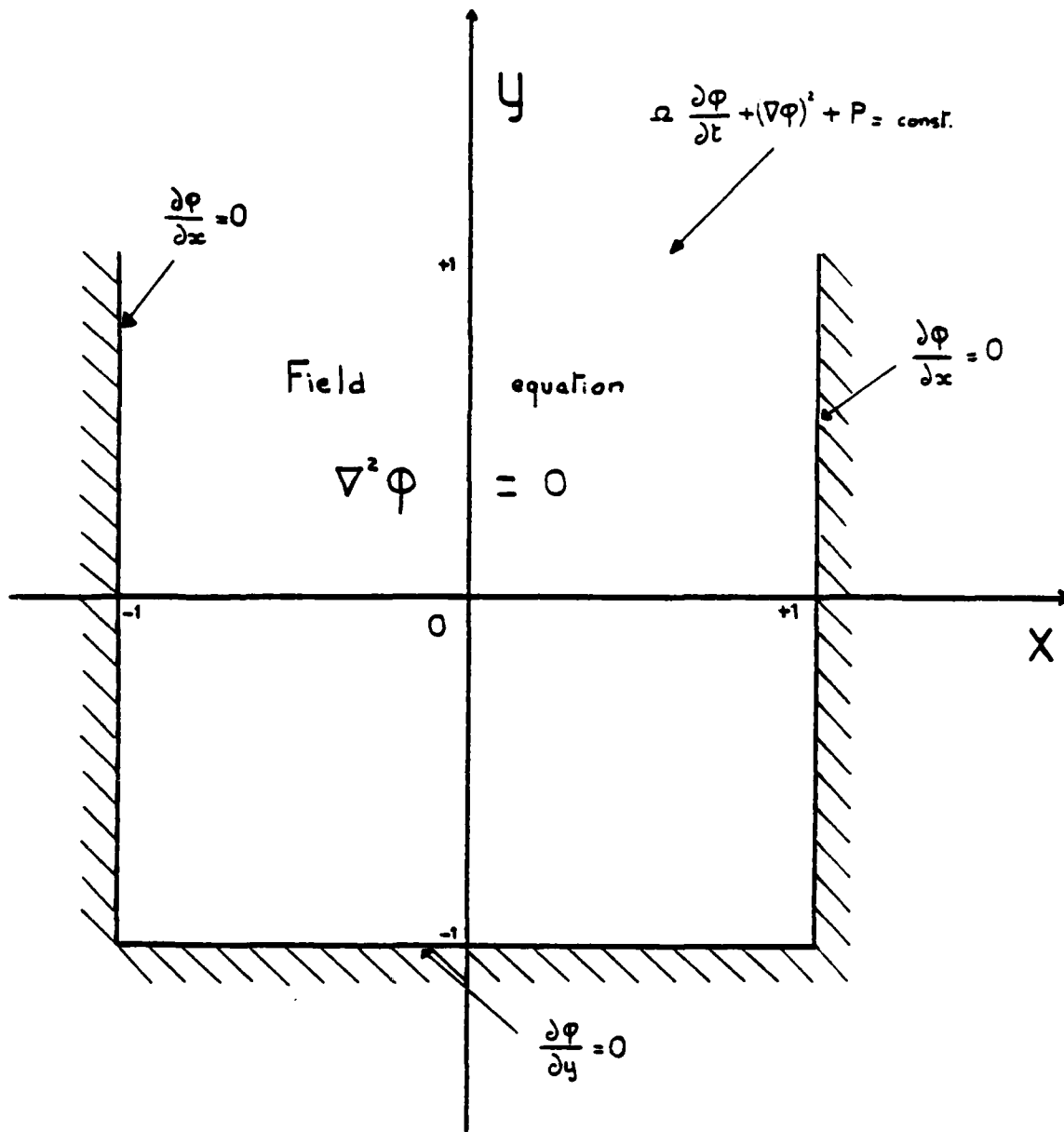


Fig. 4.2 -- Problem layout

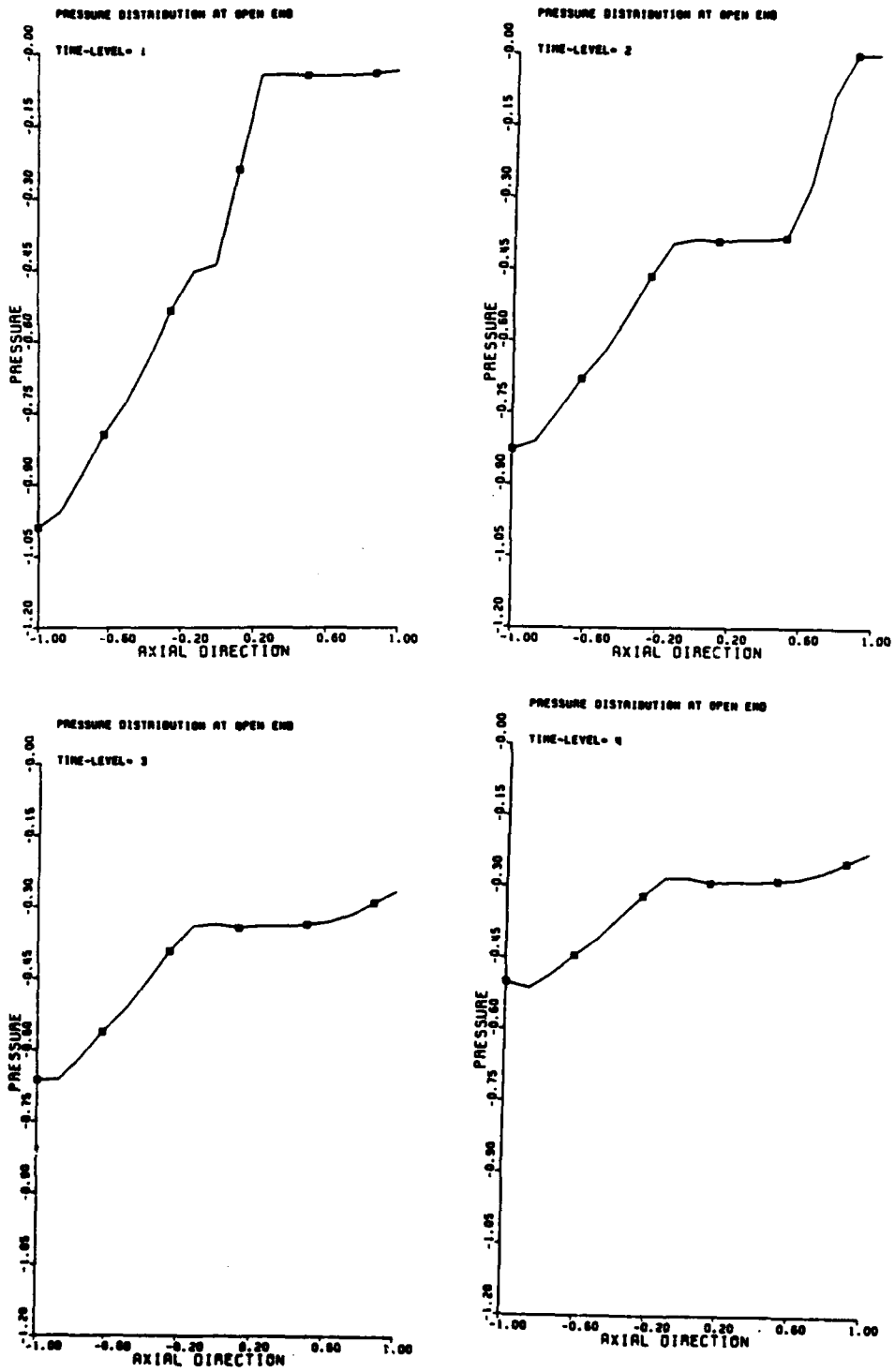


Fig. 4.3a -- Pressure Distribution at 8 Different Time Levels at the Open End

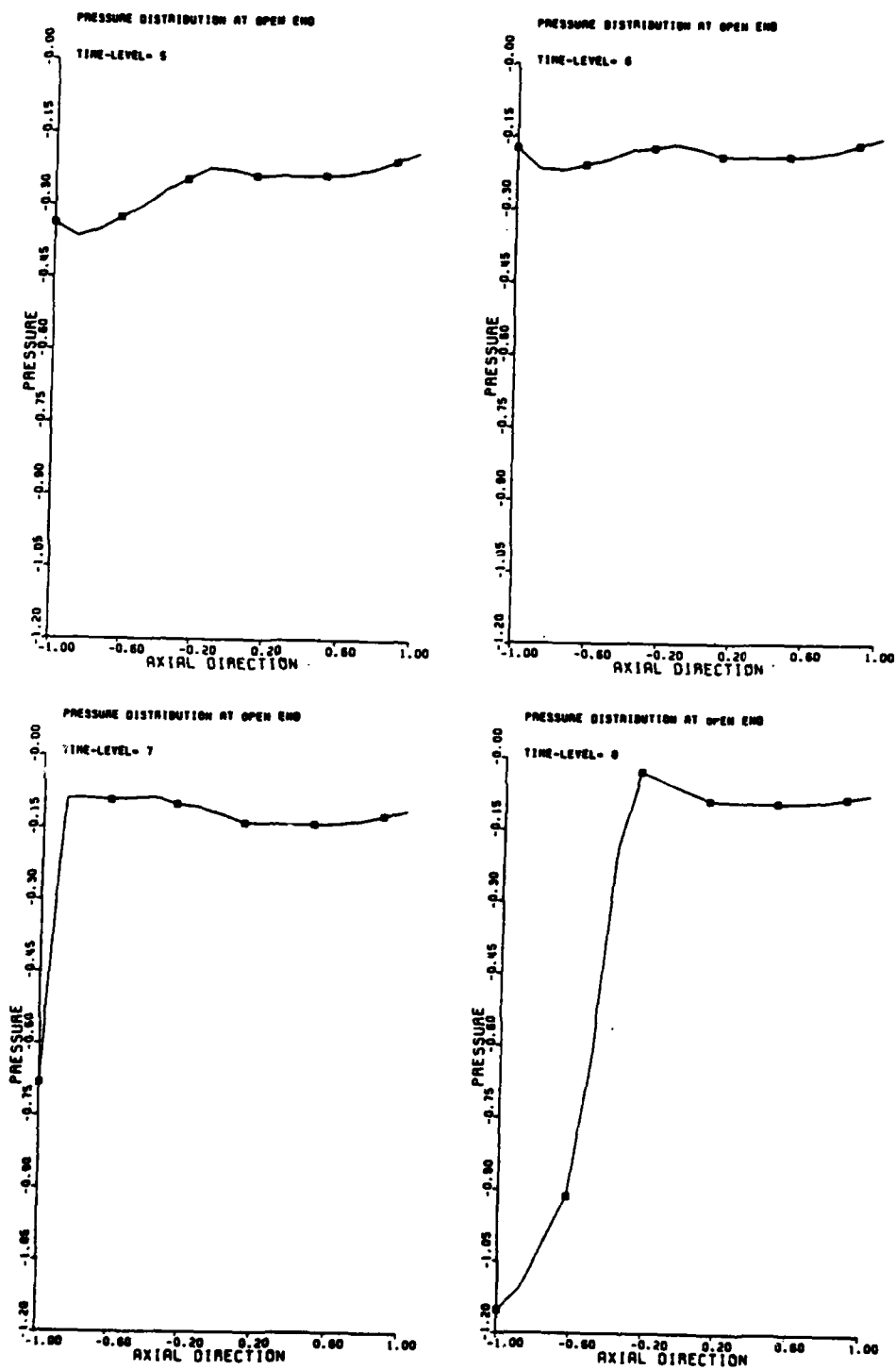


Fig. 4.3a (Cont'd.)

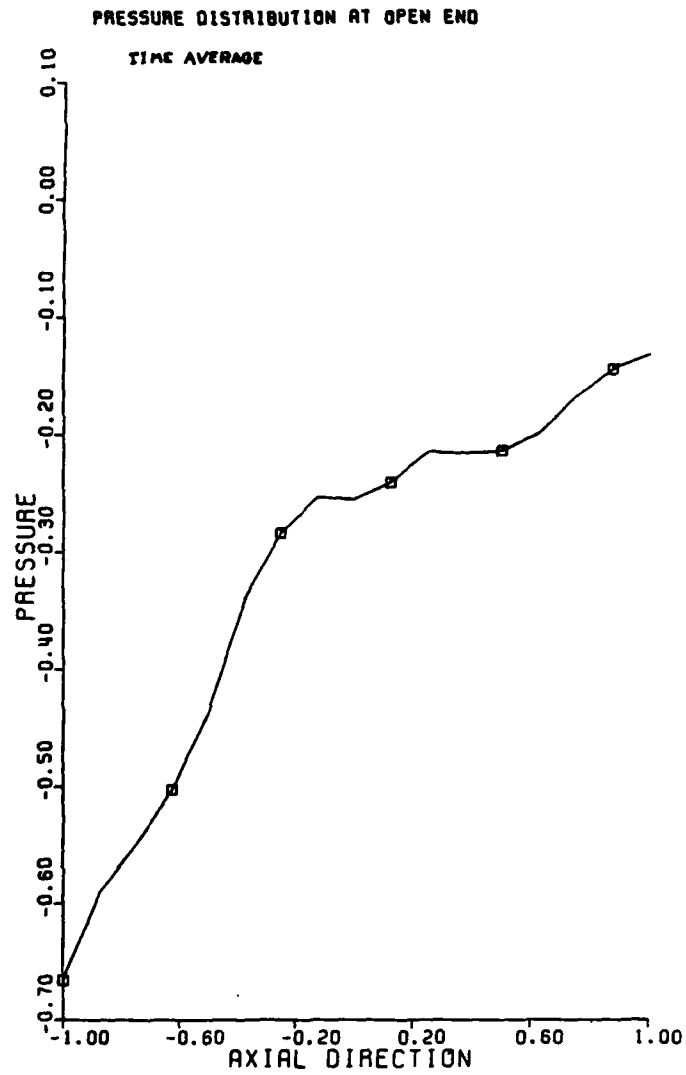


Fig. 4.3b -- Time-Averaged Pressure Distribution at Open End

AXIAL VELOCITY DISTRIBUTION AT OPEN END

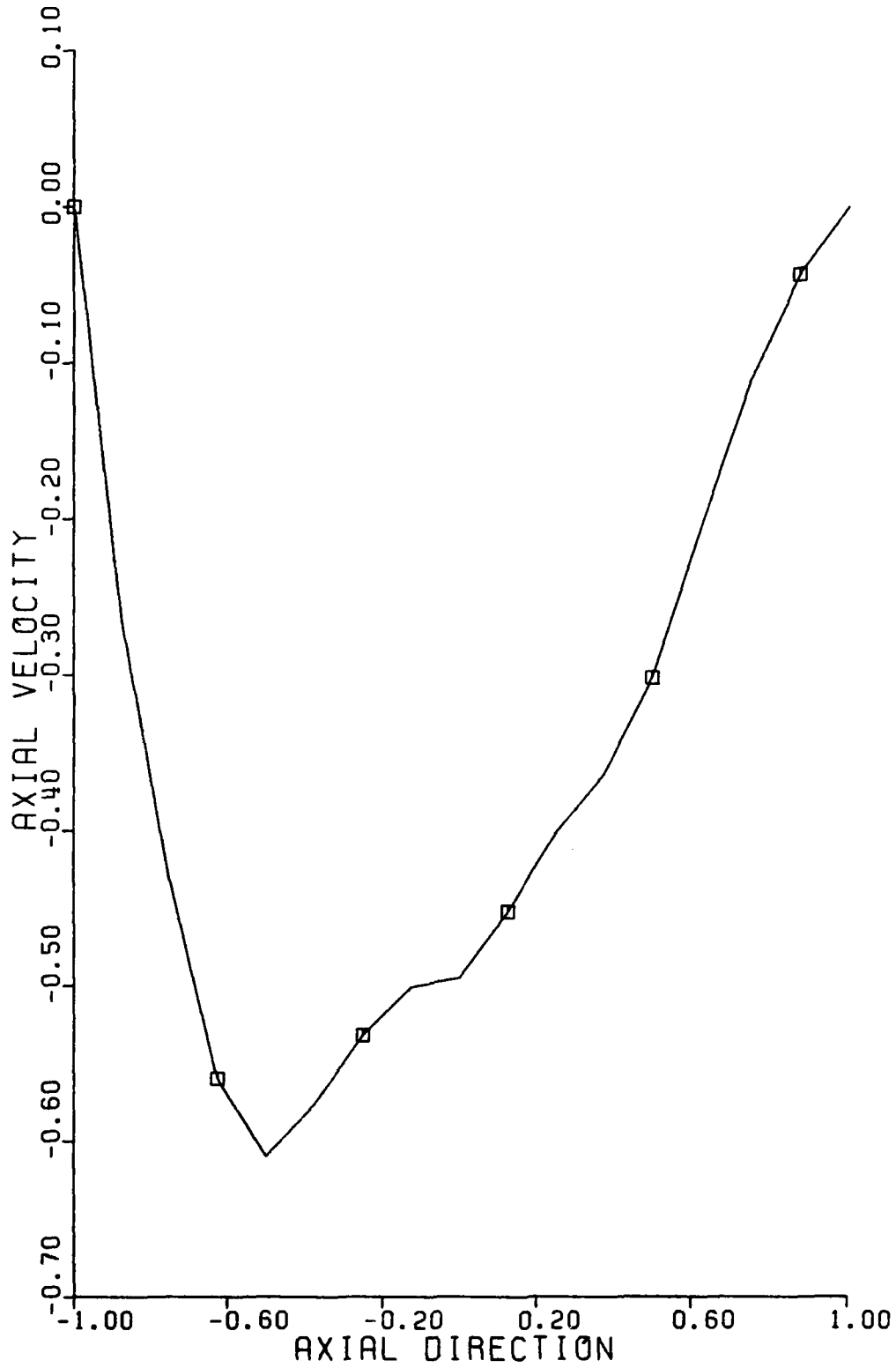


Fig. 4.4a

VERTICAL VELOCITY DISTRIBUTION AT OPEN END

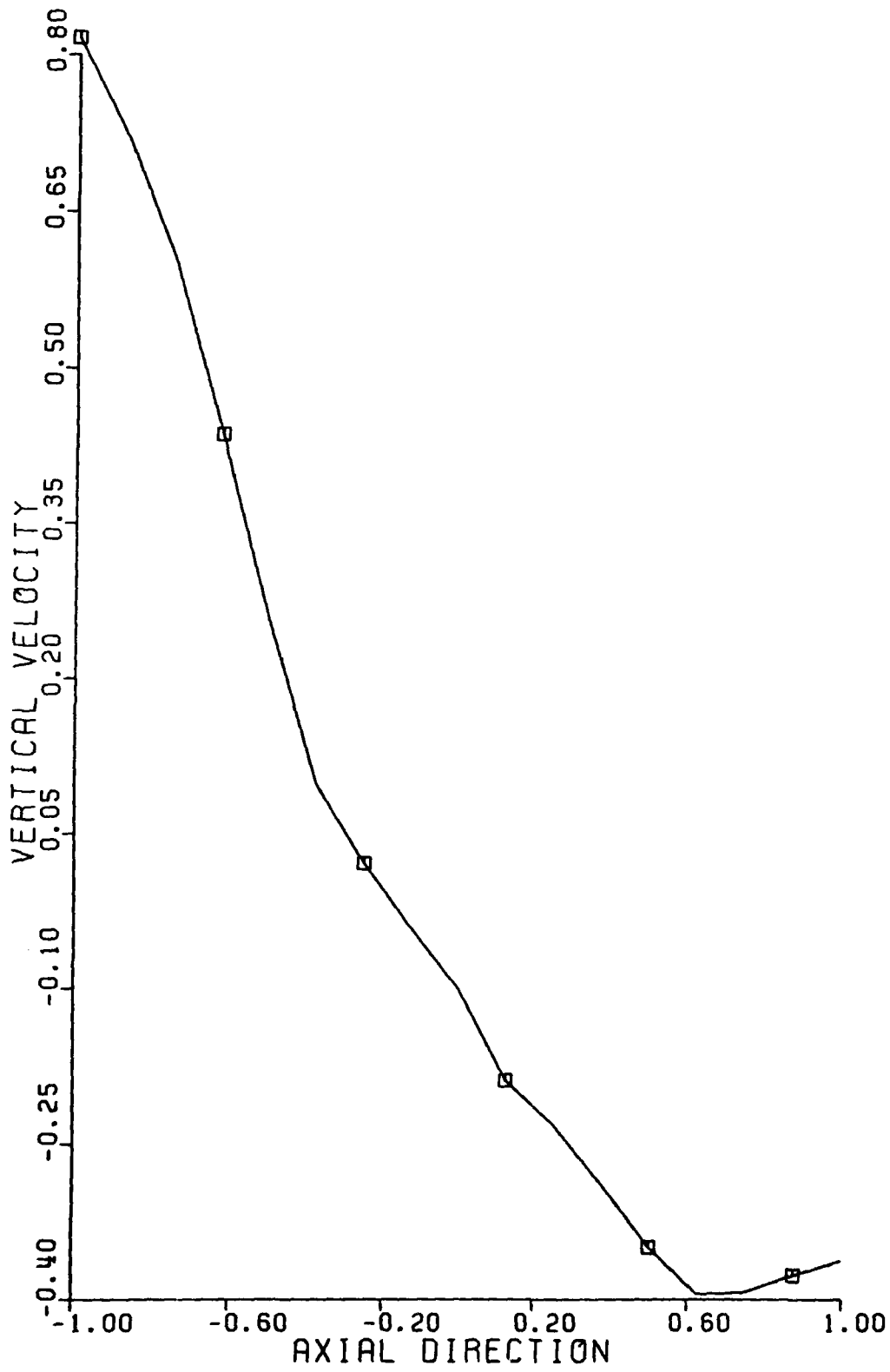


Fig. 4.4b

GENERAL PROGRESS ON AFRAPT

During the last year the Air Force OSR sponsored educational program, called Air Force Research in Aeronautical Propulsion Technology (AFRAPT), was initiated. An industry-faculty steering committee was established. It consists of

Dr. Michael Salkind	AFOSR, Chairman
Mr. Walter Schrader	AVCO Lycoming
Dr. Lynn Snyder	DDA
Mr. Elmer Wheeler	Garrett Aerospace Corp.
Dr. Fred Erich	GE Lynn
Dr. David Wisler	GE Evendale
Mr. Morris Zipkin	Pratt and Whitney (GPD)
Professor Sanford Fleeter	Purdue University
Professor Peter Jenkins	Texas A & M University

and

Professor E. E. Covert	Massachusetts Institute of Technology, Secretary
------------------------	---

This group has met three times, established procedures, put out the first year's brochure and generally put the program in motion.

This spring 22 applications were received, 9 offers were made and 5 acceptances have been received.

The Steering Committee met to review the program for next year and decided to continue the program in the present form.

3. PUBLICATIONS

Cheng, P., et al., "Effects of Compressor Hub Treatment on Stator Stall and Pressure Rise," to be submitted to AIAA/ASME/SAE Joint Propulsion Specialists Conference, June 1983.

De Siervi, et al., "Mechanisms of Inlet Vortex Formation," Journal of Fluid Mechanics, 124, 173-208, Nov. 1982.

Hawthorne, W.R., et al., "Theory of Blade Design for Large Reflections, Part I: Two Dimensional Cascades," submitted to 1983 ASME Gas Turbine Conference/Journal of Engineering for Power.

Tan, C.S., et al., "Theory of Blade Design for Large Reflections, Part II: Annular Cascades," submitted to 1983 ASME Gas Turbine Conference/Journal of Engineering for Power.

Thompkins, W.T., et al., "Solution Procedures for Accurate Numerical Simulations of Flow in Turbomachinery Cascades," AIAA Paper 83-0257, presented at AIAA 21st Aerospace Sciences Meeting, Jan. 9-13, 1983, Reno, Nevada.

Tong, S.S. and Thompkins, W.T., "A Design Calculation Procedure for Shock-Free or Strong Passage Shock Turbomachinery Cascades," ASME paper presented at 27th ASME Gas Turbine Conference, April 1982. To be published in Journal of Engineering for Power.

REPORTS

Liu, W., "Design and Analysis of an Experimental Facility for Inlet Vortex Ingestion," M.I.T. GT & PDL Report #166, August 1982.

4. PROGRAM PERSONNEL

Principal Investigators:

Edward M. Greitzer  
Associate Professor of Aeronautics and Astronautics

William T. Thompkins, Jr.  
Associate Professor of Aeronautics and Astronautics

James E. McCune  
Professor of Aeronautics and Astronautics

Co-Investigators:

Alan H. Epstein  
Assistant Professor of Aeronautics and Astronautics  
Associate Director of Gas Turbine & Plasma Dynamics Laboratory

Choon S. Tan  
Research Associate

Collaborating Investigators:

Eugene E. Covert  
Professor of Aeronautics and Astronautics  
Director of Gas Turbine & Plasma Dynamics Laboratory

Frank H. Durgin  
Research Associate

Sir William R. Hawthorne  
Senior Lecturer

Graduate Students:

9/82 - Present	Sinan Akmandor
9/80 - 8/82	Peter Cheng *
9/81 - Present	Thong Dang *
9/81 - Present	Philippe Kletzkin *
9/80 - 8/82	Wen Liu *
9/80 - Present	Wing-Fai Ng
9/82 - Present	Cheryl Shippee
9/82 - Present	Gilles Thevenet
9/79 - Present	Siu Shing Tong

\*S.M. Degree Completed.

5. INTERACTIONS

Presentations

E.M. Greitzer, lecture series on "Flow Instabilities in Gas Turbine Engines" (including inlet distortion effects, stall enhancement using casing treatment, non-uniform swirling flows in turbomachines, etc.), presented at Nanjing Aeronautical Institute, Nanjing, China, and Beijing Institute of Aeronautics and Astronautics, Beijing, China, October 1981.

E.M. Greitzer, seminar at NASA Lewis Research Center "Non-Recoverable Stall in Axial Compressors," January, 1982.

E.M. Greitzer, seminar at NASA Lewis Research Center, "Mechanisms of Inlet Vortex Formation," June, 1982.

E.M. Greitzer, lecturer in Southwest Applied Mechanics Lecture Series "The Stability of Pumping Systems", October 1982.

A.H. Epstein, "Time Resolved Measurements in a Transonic Compressor," paper presented at 1982 ASME Gas Turbine Conference, London, England, April, 1982.

As described in previous reports, there are strong interactions between the Gas Turbine Laboratory and the aircraft engine industry, as well as Air Force and other government laboratories. In addition we have an active seminar program to bring speakers from industry and/or government to M.I.T. During the past year these have included

Dr. J. Caspar, United Technologies Research Center  
"Numerical Calculation of Cascade Flows Using Non-Orthogonal Grids"

Mr. R.E. Davis, Pratt and Whitney Aircraft, Government Products Division  
"Designing for Transients in High Performance Gas Turbine Engines"

Dr. M.E. Goldstein, NASA Lewis Research Center  
"Generation of Tollmien-Schlichting Waves by Free-Stream Disturbances"

Dr. R. Mani, Corporate Research Center, General Electric Company  
"Some Aspects of Gas Turbine Engine Post-Stall Behavior"

Dr. R. Norton, Rolls Royce U.S.A. (on leave from M.I.T.  
Department of Aero/Astro)  
"Transonic Flow in a Nozzle Guide Vane"

Mr. R. Novak, Aircraft Engine Group, General Electric Company  
"A Mixed-Flow Cascade Passage Design Procedure Based on A Power  
Series Expansion"

Mr. B.A. Robideau, Pratt & Whitney Aircraft, Commercial Products  
Division  
"Practical Application of Aerodynamic Principles to Multistage  
Compressor Design"

Dr. M. Sajben, McDonnell-Douglas Corporation  
"Unsteady Aspects of Internal Flows with Shock/Boundary Layer  
Interaction"

Dr. M.J. Werle, United Technologies Research Center  
"Boundary Layer Separation in Turbomachinery"

6. DISCOVERIES, INVENTIONS AND SCIENTIFIC APPLICATIONS

Discoveries

We have demonstrated (for the first time) that compressor hub treatment can markedly improve the stall margin of an axial compressor stator row.

Inventions and Scientific Applications

A transonic flow computation procedure, having stagnation pressure errors on the order of 1%, has been developed for turbomachinery cascades.

7. CONCLUSIONS

In brief, although some of the projects appear farther along than others, the M.I.T. Multi-Investigator effort appears to be basically on target. In addition, it now appears that we are seeing "build-up" efforts of the previous years start to bear fruit, as reflected in the publications produced.

DATE  
LMEI  
8